UNIVERSITÀ DEGLI STUDI DI PADOVA

Dipartimento di Ingegneria Industriale

Corso di Laurea Magistrale
in Ingegneria Aerospaziale

EFFETTO DEL SUPPORTO IN MISURAZIONI IN GALLERIA DEL VENTO

Relatore: Dr. Ing. Ernesto Benini
Supervisor: Dr. Ing. Sebastien Paris
Advisor: Dr. Ing. Tamas Bányai

Laureando: Alberto Ghiraldo
Matricola: 1057998

Anno Accademico 2014/15

ABSTRACT

In questa relazione è descritta la progettazioni di supporti per prove in galleria del vento. Il lavoro è stato svolto al Von Karman Institute di Rhode Saint-Genèse (BE) e riguarda un progetto commissionato dell'azienda S3-Swisse Space System per lo studio della separazione del veicolo suborbitale SOAR dal primo stadio di missione, ovvero un aereo commerciale Airbus. I supporti sono progettati per futuri test di separazione del SOAR, versione V10, nella galleria del vento S1 dell'istituto. Questo studio origina da una precedente campagna di prove realizzata nelle medesime condizioni, i cui risultati sono riportati nella relazione interna S3-VKI-RPT-001. I supporti sono progettati in scala 1:180 per le prove in presenza simultanea del SOAR e dell'Airbus, mentre in scala 1:80 per i test del solo SOAR. Due differenti sezioni di supporto, circolare ed ellittica, sono valutate per entrambi i casi. In una prima parte del presente documento vi sono le considerazioni che hanno portato alle scelte progettuali, quindi i risultati dell'analisi strutturale agli elementi finiti (FEM) e infine gli esiti dello studio fluidodinamico computazionale (CFD). Per fare ciò simulazioni del SOAR con e senza supporto sono state eseguite a Mach 0.7. Inoltre sono riportate considerazioni sul comportamento delle due diverse forme e su variazioni dimensionali nei supporti ad angoli d'attacco compresi tra 0 e 15°.

In this report a process of support design for wind tunnel models is described. The work was performed at The Von Karman Institute of Sint-Genesius Rhode (BE) and it was commissioned by the S3-Swisse Space System company. It concerns the separation wind tunnel test of the suborbital vehicle SOAR from an Airbus commercial plane carrier. The supports are designed for future separation wind tunnel test of the SOAR, version V10 in the VKI-S1 wind tunnel. The work origins from the results of the VKI-S1 wind tunnel campaign reported in the issue S3-VKI-RPT-001. The supports are designed in scale 1:180 for the test of the SOAR in presence of the Airbus and in scale 1:80 for the SOAR alone test. Two different shape of support, circular and elliptic, are tested in each cases. First there are the supports designed, then the results of the FEM static structural analysis and vibrational analysis, finally the result of the CFD campaign. The behaviour of the two shapes and of the dimensional variations are investigated at angle of attack between 0° and 15°. The simulations of the SOAR with and without supports are carried on at Mach 0.7.

Index

List of symbols, abbreviations and nomenclature

α Angle of attack

B Inclination angle of the support vertical part

CoG Centre of gravity

C' Aerodynamics coefficient corrected for the effect of the support

D Model base diameter

d Sting diameter

L_C Critical sting length

l Sting length

l_i Length of the support inclined part (scale 1:180 only)

M Mach number

P_b Base pressure

q_∞ Dynamic pressure

R_e Reynolds number

VKI The Von Karman Institute

Sting. It is a kind of support for wind tunnel test that enter from the base of the model. With this term the rectilinear circular and elliptic supports in scale 1:80 are described in this paper. Also the rectilinear part of the supports in scale 1:180 is called with this name.

Strut. It is a kind of support that sustains the model from the bottom or from the top.

Support. This word in this document means wind tunnel supports in general. Also the supports in scale 1:180 model are so called.

Index of figures

Index of tables

1 Introduction

The present project, commissioned by S3-Swiss Space System deals with the development and qualification of a 3 stage to orbit composite vehicle. The first and the second stage, respectively the Airbus and the SOAR[1] vehicles are reusable, whereas the third stage is an expandable booster. For this project it is requested to design new supports for the separation wind tunnel test.

The S-3 SOAR separation from the Airbus A300 is a critical issue during the mission. The aerodynamic coefficients are affected by the proximity of the vehicles. In order to design properly the separation, the aerodynamic database must be known with sufficient accuracy. For this reason an important campaign of wind tunnel test is necessary. The aerodynamic coefficients depend of the Mach number, the angle of attack, the position of the control surfaces of the vehicles as well as their relative positions.

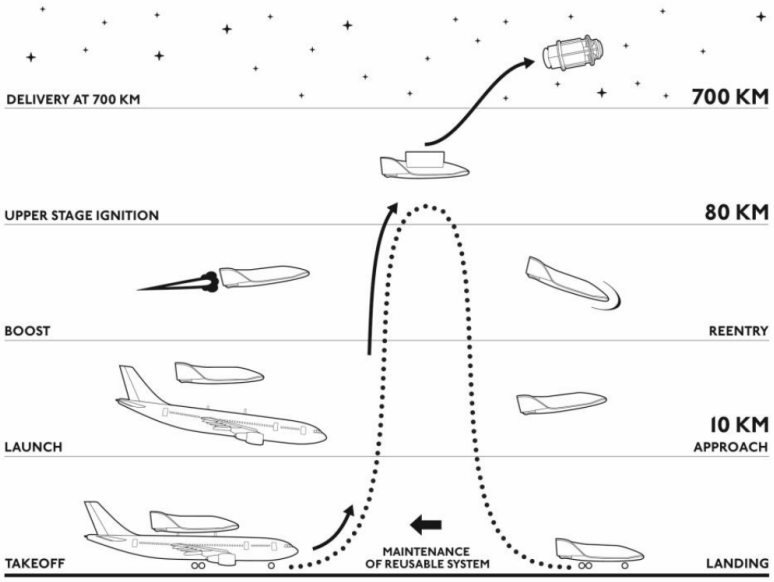

Figure 1. Illustration of the main steps of the mission.

1.1 Objective of the project

A first wind tunnel campaign was already performed with the construction of an initial aerodynamic database [1]. In prevision of further wind tunnel experiments it is required to improve the knowledge in supports design. In fact to design supports for the SOAR, in this configuration, is particular complicated for the presence of the Airbus below and behind the vehicle[2]. In effect the first sting designed produced great interferences on the SOAR. Then the

[1] SOAR is the acronym of Sub Orbital Aircraft Reusable.
[2] The presence of the empennage impede to use also a support from the base.

purpose of this work is to design supports for the SOAR vehicle in the following two configurations:

- scale 1:180 wind tunnel test of the SOAR in presence of the Airbus;
- scale 1:80 wind tunnel test of the SOAR alone.

1.2 Reference geometry

In this paragraph the geometry of the SOAR and of the Airbus in their relative configuration are presented.

Figure 2. SOAR and Airbus carrier in the composite configuration before the separation.

1.2.1 SOAR

The SOAR aero-shape is based on the Hermes reentry vehicle. In this project, it is used the version V10 received from S3 in August 2013. Nowadays it is only available a model in scale 1:180 used in the previous wind tunnel test with an internal three component balance. New models and new balances will be build for the new experiments. It is request to design the supports for a six component internal balance.

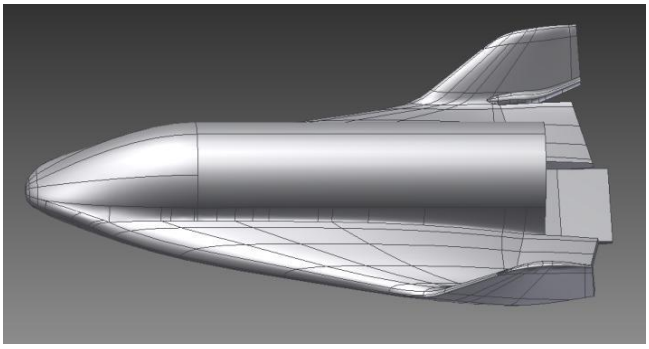

SOAR			
Scale	**L_{ref}[m]**	**S_{ref} [m^2]**	**CoG**
1:1	17.00	87.98	(-10,202; 0;0)
1:180	0.0944	0.00271	
1:80	0.2125	0.01374	

Figure 3. SOAR reference geometry.

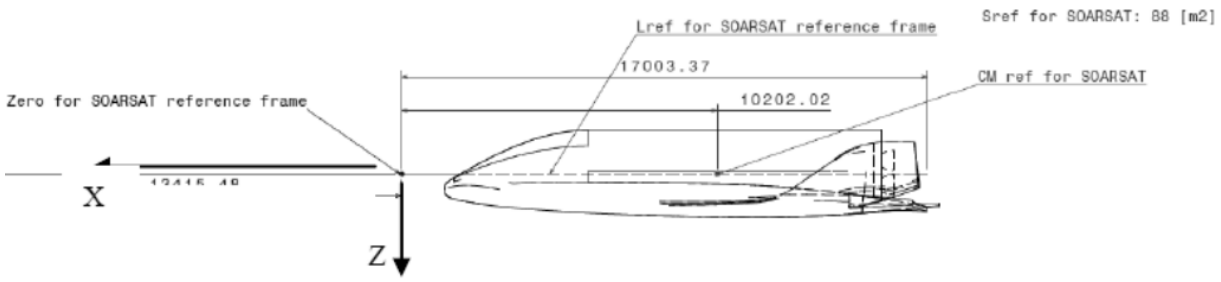

Figure 4. SOAR reference frame. This frame in the present work is used only for show the position of the centre of mass.

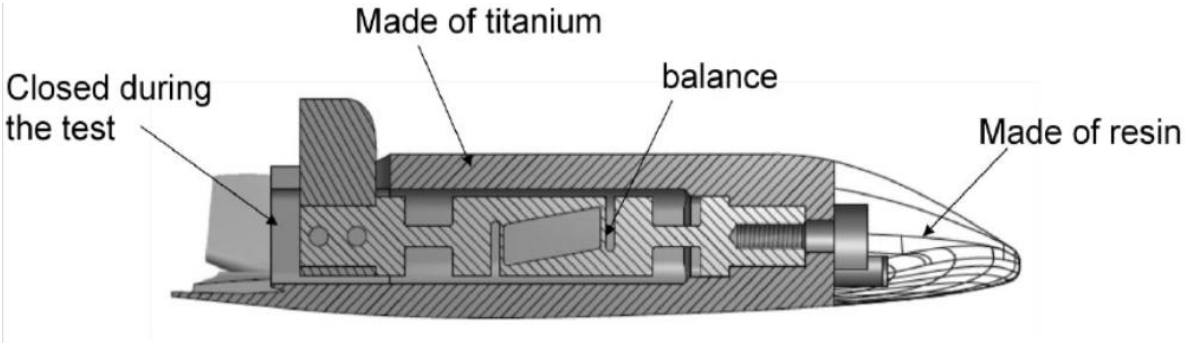

Figure 5. Technical draw of the old model with the internal balance.

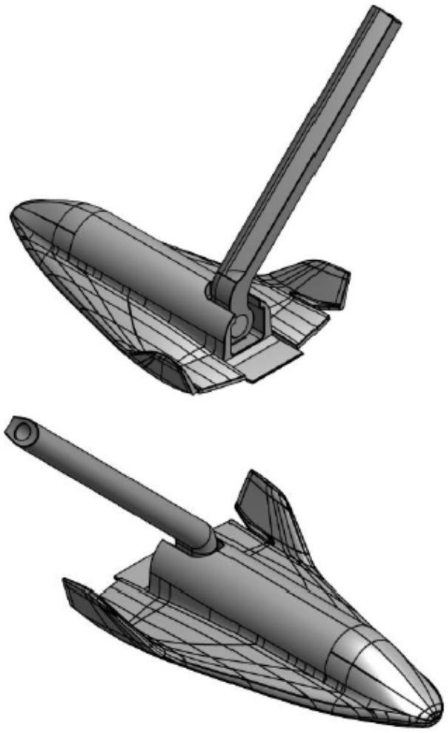

Figure 6. The support for the SOAR in the previous wind tunnel test campaign.

1.2.2 Airbus

The Airbus aeroshape is derived from the Airbus A300 with some simplification as provided by S3. In this project, it is used the version received from S3 in August 2013.

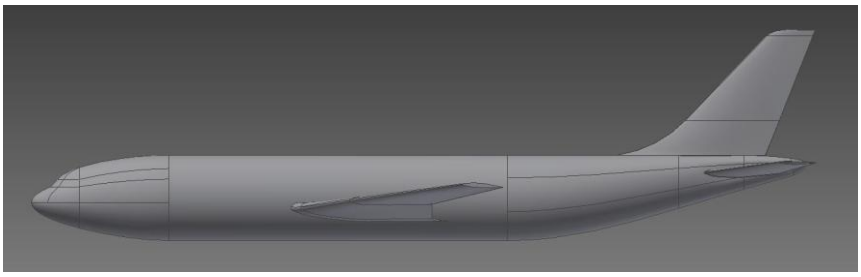

Airbus		
Scale	**L_{ref} [m]**	**S_{ref} [m^2]**
1:1	6.608	260.02
1:180	0.0367	0.008025
1:80	0.0826	0.040628

Figure 7. Airbus reference geometry

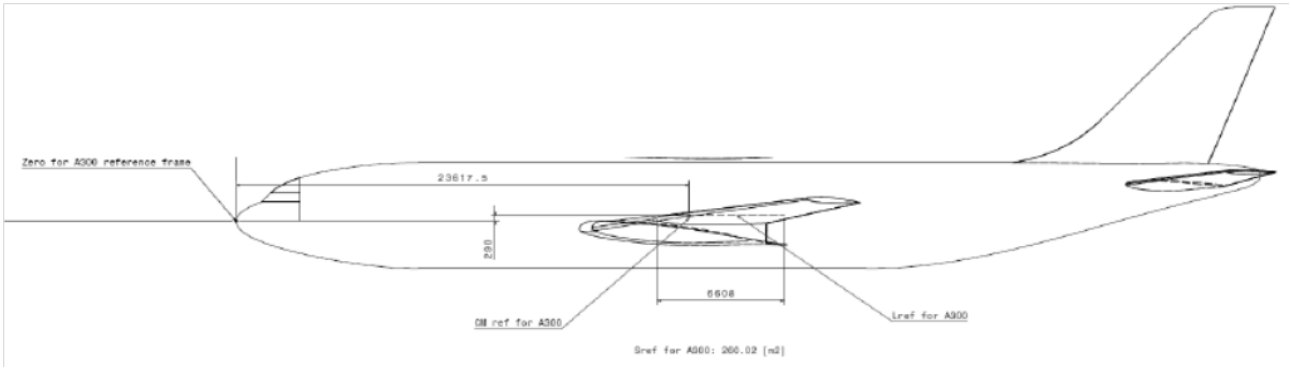

Figure 8. Airbus reference frame. This frame in the present work is used only to show the position of the centre of mass.

1.2.3 Composite configuration

In the nominal composite configuration the angle of attack of the Airbus is set to 1.5° and the delta AoA between Airbus and SOAR is 4°. The CoGs of the vehicles are located at the same longitudinal coordinate.

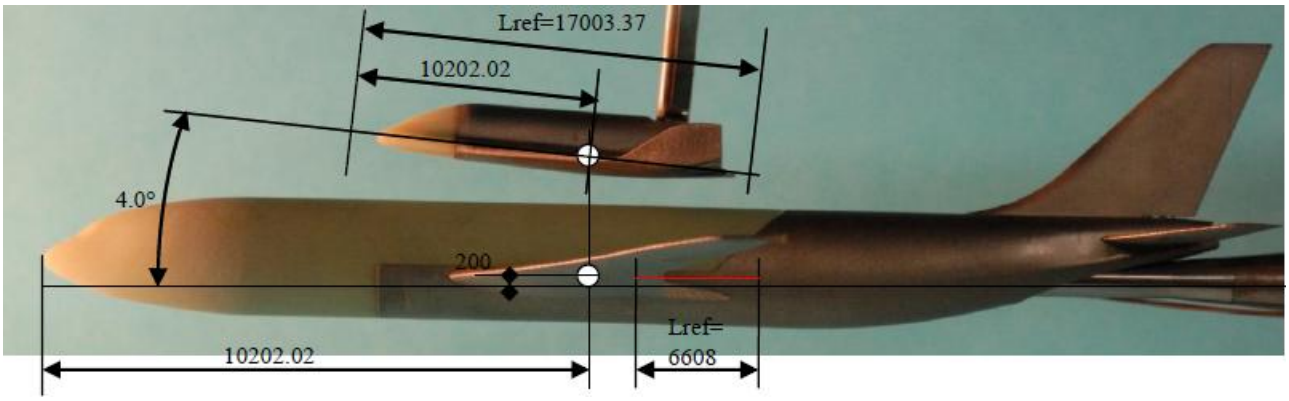

Figure 9. CoGs location and nominal positions of the composite configuration.

1.3 Wind tunnel facility

The VKI supersonic/transonic wind tunnel S-1 (see Figure 10) is a continuous closed circuit facility of the Ackeret type, driven by a 615 kW axial flow compressor. Two 0.4 m x 0.36 m test sections are available: contoured nozzles with M = 2.0 and a slotted transonic section with variable Mach number, from 0.3 to 1.05. A typical unit Reynolds number is $4 \cdot 10^6/m$. The test section contains a three-degree-of-freedom traversing mechanism for model and/or probe support, as well as a variable incidence mechanism (up to ± 35 degrees). A six-degree-of-freedom mechanism will be build for the next wind tunnel test. Only the subsonic test section is supposed to be used (Mach=0.7) for this study.

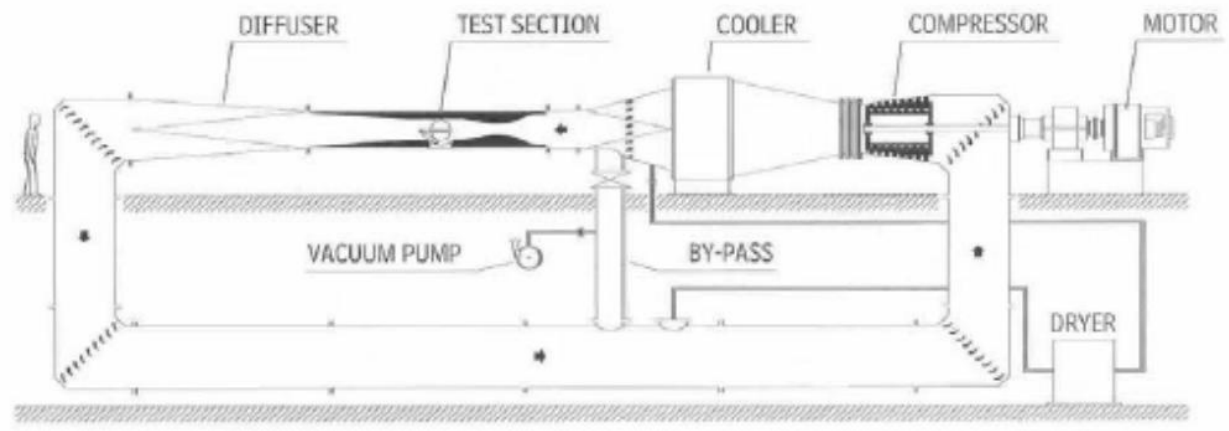

Figure 10. S1 wind tunnel.

2 Support design theory

In this chapter the common rules for the wind tunnel support design followed for this project are briefly explained. First an overview on the possible support configurations, after that the guideline for the design are presented.

2.1 State of the art

The support in wind tunnel test is necessary to hold up the model in the test section but it is also an artificial device that, especially from an aerodynamic point of view, does not exist.

The first and most common support used, especially for subsonic test, is the “single or three strut support” that sustain the model from the bottom part. A variation of this is to use a “twin strut support” with two rods under the wings. Increasing the number of struts rises the stiffness but also the complexity and the interferences.

Other solutions are to use “dorsal strut support” with the support that enter from the top of the fuselage. Otherwise the “half model mount” is a possibility for symmetric bodies but this choice does not allow six degrees of freedom measurement.

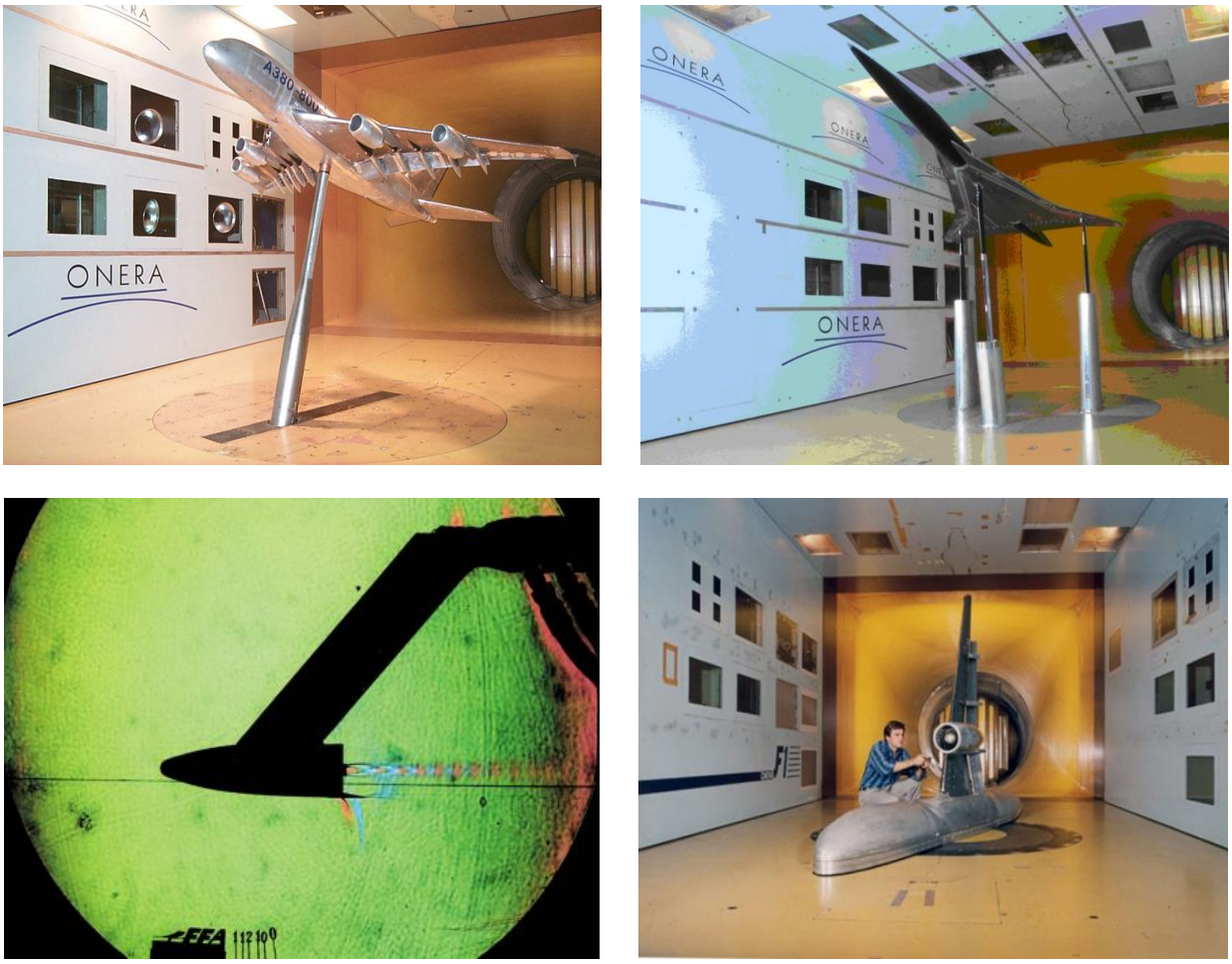

Figure 11. On the top two model tested in the ONERA F1 wind tunnel: left with a single strut, right with trhee srus. On the bottom: left the EXTV model with a "dorsal strut" (S4 FFA), right an "half mounted" model (ONERA F1).

Finally the “sting support family” developed especially to reduce the interferences in transonic wind tunnel testing. Usually a sting is a kind of quite long and thin support that sustains the model from the base part. In addition to the “straight sting” also some variations exist like the “bent sting” used for high angle of attack, the “zed sting support” and the “fin sting support”. The last couple of sting configurations are chosen according to the layout of the model posterior part.

Figure 12. On the top left the Dream chaser with a rectilinear sting, on the right the Shuttle with a bent sting. On the bottom left a "Z sting", while on the right a "fin sting" both applied at commercial planes (ONERA S1MA wind tunnel).

2.2 Design rules for wind tunnel support

From the definition of wind tunnel support given in the previous paragraph it is immediate to derive the requirement for its design:

- to minimize the aerodynamic interferences with the flow;
- to have adequate mechanical properties to sustain the model (stiffness, strength, minimum strain...);
- to permit flow measurements;

- to allow electrical supply and, for internal balance, permit the interface with balance and measurement devices through the passage of cables;
- To allow the supply and the return of the fluids.

By the second post-war, when wind tunnel tests at high speed dramatically rose, aerodynamicists realized that from transonic flow the interferences with common struts supports (single or multiple) increased considerably. Then it was developed a new kind of support, that is the "straight sting" to reduce (but not cancel) the interferences. This is a tube that enters the model at the base. With this solution all the supporting structure is downstream of the model. When it is used the balance system is usually internal at the model [2].

Once acquired requirements about flow measurement and passage of cables,[3] the two parameters to be optimized are to minimize the aerodynamic interferences and to give adequate mechanical properties. For stings this means that to minimize interferences it is necessary to have a sting as long as possible and with the diameter as small as possible. These requirements are not in agreement with the structural properties for which stings should be short and have a large diameter. This optimization is the central point of a sting design because, especially in transonic region, sting length and sting diameter dramatically influence the base pressure of the model [3].

An important parameter in this dissertation is the "critical sting length" that is “the shortest sting length that does not change the level of an aerodynamic measurement obtained with longer stings”[4]. Critical sting length is influenced by the Mach number, Reynolds number, boundary layer at the base of the model, sting diameter and model base. Especially Reynolds number plays an important role. In fact if the flow is laminar at the base of the model L_C is as much as 12-15 times the base model diameter (D), on the other hand with turbulent flow L_C reduces to 3-5 D. This is due to the fact that with turbulent flow the skin friction drag (viscous) increases and it depends on the wet areas that, obviously, rise with the sting length [3]. During the design it is implied that it is desirable to have the sting length as near as possible to the critical sting length.

About the diameter it is necessary to pay attention that it does not have to modify the typology of boundary layer at the model base. The minimum diameter allowable, from load considerations, is about 0.25 times the base diameter [3]. For the maximum value it is necessary to consider that in the transonic flow minimum interferences exist with a sting diameter until 0.4 times the base [5]. Furthermore it is not possible to have a sting diameter less than 0.3 times the base diameter in wind tunnel where high dynamic pressure values are present.

Another important rule to remember during the stings design is that the model base pressure rises for the presence of the sting, especially increasing the diameter.

For large angle of attack test it may be useful to choose an oval (elliptic) shape for the sting. This shape is more streamlined in the flow direction and then it should reduce the interferences that are common with the increase of α [6].

[3] Cables are necessary with internal balance and they can pass inside the support or outside it.

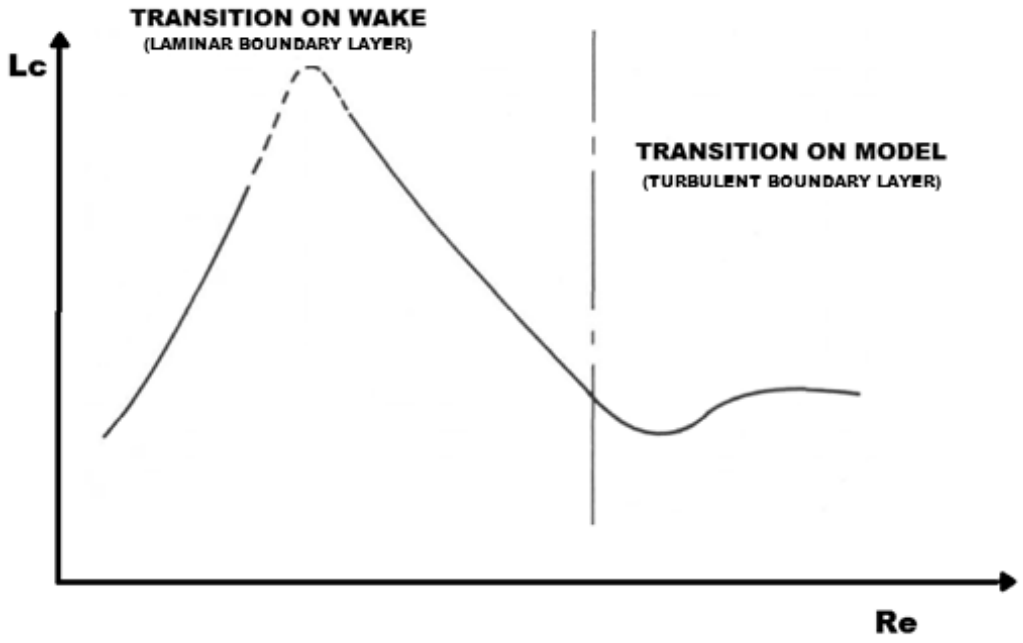

Figure 13. Plot of the critical sting length function of the Reynolds number [3].

3 Supports designed

In this section the project constraints and then the supports designed are presented. The choices done derive directly from the constraints and following as much as possible the rules explained in the previous chapter.

3.1 Project constraints

For the support design it was necessary to take into account a series of constraints descending both from the S3 company both from the VKI institute. The following constraints are present both in 1:180 both in 1:80 scale:

- wind tunnel test conditions (see Table XIII);
- the supports have to support the external load;
- the supports have to be adequate to the vehicle shapes and dimensions;
- to consider the wind tunnel dimensions;
- the presence of an internal six degree of freedom balance system;
- the supports have to avoid the internal passage of the cables;
- the supports design have to contain cost and simplicity of manufacturing;
- the utilization of steel as material in the manufacturing process;
- the blockage of the support and connection with the balance;
- to design a support also for different from zero angle of attack (max 15°);
- the supports design have to consider a new configuration with respect the previous one;
- the supports have to reduce interferences.

Some additional constraints are present in the scale 1:180 composite testing:

- to test the separation with the presence of Airbus empennage;
- to consider the nominal relative position of the two vehicles;
- to permit a relative motion of the SOAR over the Airbus.

The most critical constraints are now discussed more in detail.

A six degree internal balance will be equipped with 6 Wheatstone bridges and 24 small cables to transmit the information of every component. It is possible to merge together more cables in a small pipe of thermoretractable plastic (then warm it) to obtain two or three bigger cables of about 2.4 mm of diameter. It is considered the worst case with the presence of three cables of 2.4 mm of diameter.

The relative position of the SOAR over the Airbus is set to align the centre of gravity of the two vehicle (see Figure 9). The Airbus model that should be used for the next wind tunnel test has

not been transmitted from S3 yet[4]. Since the distance between the base of the SOAR and the Airbus empennage is a critical constraint for the support design it is assumed as the worst case with the smallest carrier, that is the A300. This distance is 12,8265 m, in scale 1:1. Furthermore it is necessary to take into account a safety factor of 1.5 m to allow the relative movement and do not extremely disturb the Airbus tail plane. Then the maximum support length, in scale 1:180, is 0.062 m [5]. It is also considered the inclination of the empennage that for the Airbus models is about between 40° (A300) and 47°.

Table I. Summary of the most critical constraints.

Scale	1:180	1:80
Cables diameter [mm]	3X2.4	3X2.4
Maximum sting length [mm]	62.00	/
Empennage inclination [°]	40-47	/
Model base diameter (D) [mm]	15	33.75
Mach number	0.7	0.7

3.2 The design process

Since the transonic flow field the most adequate support configuration should be a straight sting but this choice is possible only for the 1:80 scale model. It is immediately clear that, especially for the 1:180 scale, the constraints are really strict. For the presence of the Airbus with its empennage the use of a straight sting, as also struts that sustain the model from the bottom, is not possible. Moreover also the utilization of a "dorsal strut" is rejected because already tested with not satisfied results. The only remained possibility is to use a straight sting that enters in the SOAR base but at the other extremity connected with an inclined support bar before the Airbus empennage (see Figure 18 and Figure 19).

The presence of the cables inside the support needs a cavity big enough to contain them. Furthermore the presence of the hole decreases the stiffness of the support with the necessity to pay particular attention to the thickness of the walls.

As it has already said one of the most critical parameters is the sting length because of which it is necessary to know the flow topology at the base of the model. From the definition of critical Reynolds number, assuming that the transition from a laminar boundary layer to a turbulent one takes place at $R_e = 300000$, it is possible to calculate the critical length[6].

[4] It is probable that the choice will be on a bigger airbus model than the A300 received in August 2013.
[5] With this sting length the possibility of motion over the Airbus A300 is really short, the minimum requested. With bigger airbus model, that should be chosen the relative motion allowed increase.
[6] The critical length is the distance from the leading edge (in this case the SOAR nose) after which the boundary layer becomes completely turbulent. For a flat plate it is possible to assume $R_e = 500000$ [7],otherwise for a cylinder this value is around 300000 [5]. The calculations are done with the wind tunnel setup of Table XIII. The viscosity coefficient is calculated as function of the temperature and it results: $\mu_\infty = 1.74 \cdot 10^{-5}\ Pa \cdot s$

$$R_{e_{cr}} = \frac{\rho_\infty u_\infty x_{cr}}{\mu_\infty} \quad (1)$$

Table II. The Reynolds number calculated with the reference length, the critical length and the SOAR length.

Scale	Re_{Lref}	x_{cr} [m]	L_{SOAR} [m]
1:80	$6.940 \cdot 10^5$	0.0918	0.1998
1:180	$3.083 \cdot 10^5$	0.0918	0.0888

It is possible to see that for the scale 1:80 the flow at the base is turbulent, while for the case 1:180 it is more difficult to predict with certainty the flow topology at that point. In fact to have an exact knowledge of the transition point it would be necessary to perform a wind tunnel transition study, that is not possible yet for the not availability of the model.

In any case to design a sting long 12-15 times D (laminar flow at the base, see Paragraph 2.2) it was not possible for the constraint of the Airbus empennage. In the same scale, also for the diameter it was not possible to respect the rules explained (again in Paragraph 2.2) for the presence of the cable inside. For these parameter the longer possible sting and with the smaller possible diameter, respecting all safety margins, was chosen.

Otherwise for the scale 1:80 the length is chosen considering a fully turbulent flow at the base that require a sting length of 3-5 times D. The diameter is selected as small as possible again but the safety margin, for the passage of the cables or for structural reason is kept larger especially with the circular model (See Table III).

The inclined part of the support is clearly a critical point for the interferences and it dramatically brakes the flow in the proximity of the rear portion of the SOAR. For this reason it was tried to make it as less as possible inclined (B angle small; see Table III, Figure 18 and Figure 19). On the other hand this angle should not be really smaller than the empennage angle because otherwise the support would approach too much to the Airbus tail plane. Another solution adopted to try to have small interferences is to use as section of the inclined rod an airfoil shape. In fact in the transonic flow a thin airfoil permits a dramatic reduction of the drag [7]. The aim of this is to choose the thinner airfoil possible compatibly with the structural constraints and the presence of cables inside.

Another crucial point with the presence of the cables inside was the blockage with the balance. To overcome this problem a threaded end (like a screw) with a hole inside was added at the sting extremity connected with the balance. Afterwards in the scale 1:180 supports the cables come out from the end of the sting to come inside the inclined part. This choice was done to simplify the passage and to allow every kind of access and connection (see Figure 20).

From the beginning it was already clear that the support design for the separation of a vehicle from a carrier plane is something particular. Now it is evident that all the project constraints lead to deal with a problem that is really unique and unexplored.

For the problematic nature of the project it is possible to face it in a three steps iterative method:

1. support designs;
2. structural analysis (FEM);
3. aerodynamic analysis (CFD).

After the last step a complete balance of the project is performed and the necessary modification are purposed. If the requested changing in the design are important it will be indispensable to redo point 2 and 3 in the iteration.

3.3 The supports realized

After it has been illustrated the problems rose during the design and the solutions chosen, in this paragraph the results of that process are exposed.

For the SOAR alone (scale 1:80) it was chosen as support a straight sting mounted in the rear part of the vehicle. This solution, as already discussed, is the most suitable for transonic wind tunnel test. Two different shapes of sting sections are evaluated in this work:

- Circular;
- Elliptic;

The circular one is the most common and there are many references in literature [2], [3], [4]. On the other hand an elliptic sting should reduce the interferences and the drag especially a high angle of attack [6]. These configurations will be evaluated at every step of the design process, first from a structural point of view, and then with a flow analysis using a CFD software. Since the short literature existing, the use of the elliptic sting and, eventually, the advantage of this choice are deeply investigated.

The separation wind tunnel test (scale 1:180) raises many more difficulties, as already discussed in the previous paragraph. For this reason a sting at the beginning rectilinear but then inclined with an angle of 40.8° in the presence of the Airbus empennage is chosen. Once again for the rectilinear part both the circular shape and the elliptical one are evaluated. Instead the inclined section is a NACA 0016 airfoil cut in the rear section.

The supports are designed to allocate the cables as shown in Figure 14 and Figure 15. All supports have not any problems to allocate 3 cables of 2.5 mm of diameter. In the inclined part the maximum diameter insertable for three cables is 2,4 mm.

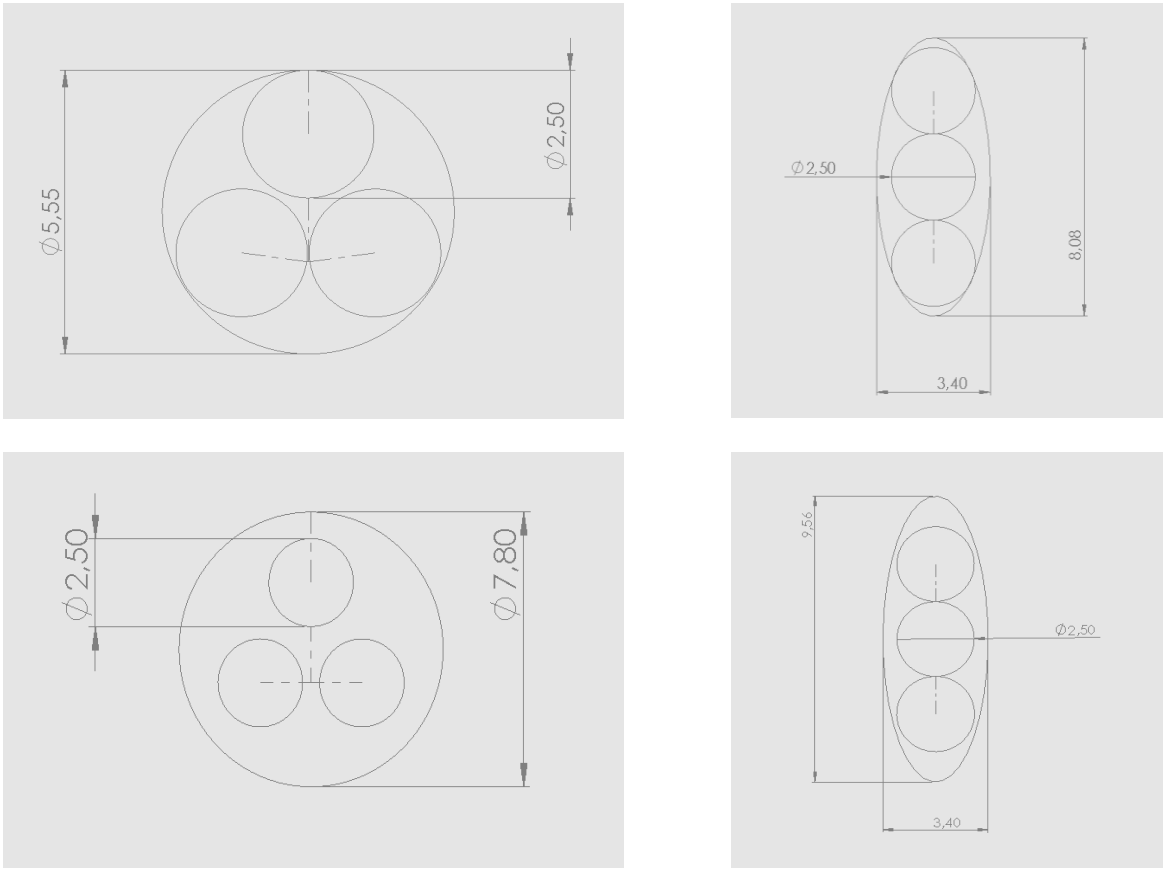

Figure 14. Drawings of the sting hole section with the cable inside. On the top scale 1:180, on the bottom scale 1:80.

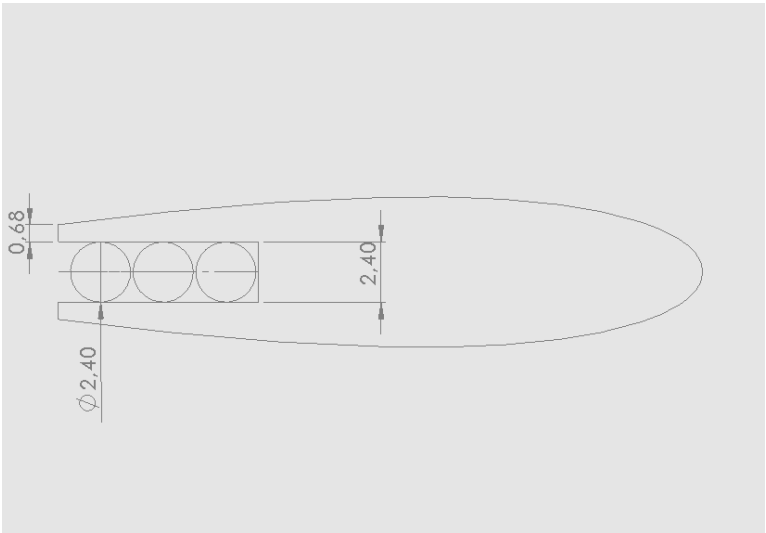

Figure 15. Drawing of the inclined bar with the cables in the hole; scale 1:180.

In the following tables all dimensions are resumed:

Table III. Support dimensions.

Scale	shape	d [mm]	d_s/D	Φ [mm]	l_s [mm]	l_s/D	B [°]	l_i [mm]
1:180	circular	8.55	0.57	5.55	62	4.13	40.8°	134.15
	elliptic	(10.6;6.2)	0.56	(8.8;3.4)	62	4.13	40.8°	134.56
1:80	circular	11.81	0.35	7.80	114.75	3.40	/	/
	elliptic	(12.1;7.1)	0.28	(9.56;3.4)	114.75	3.40	/	/

In the following sketches there are the supports designed. Lengths are in millimetres and angles in degrees.

Figure 16. Circular sting, scale 1:80

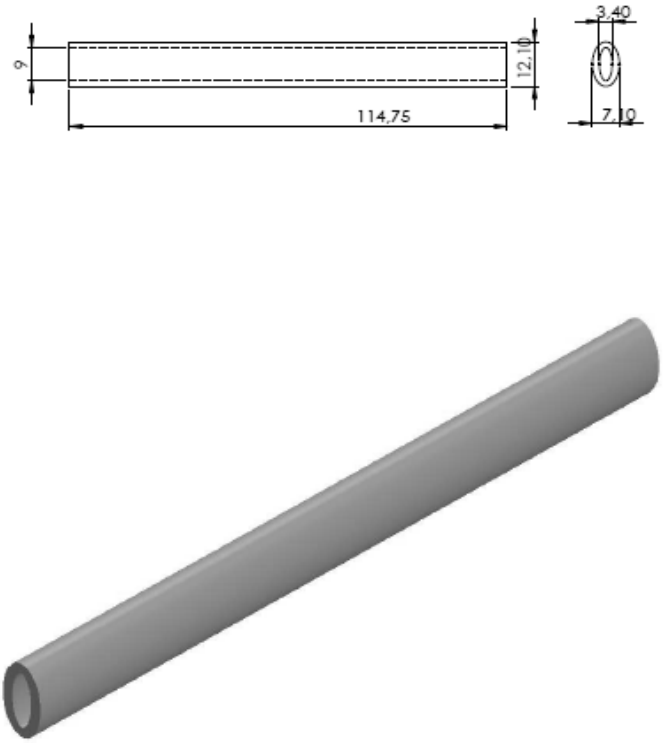

Figure 17. Elliptic sting, scale 1:80.

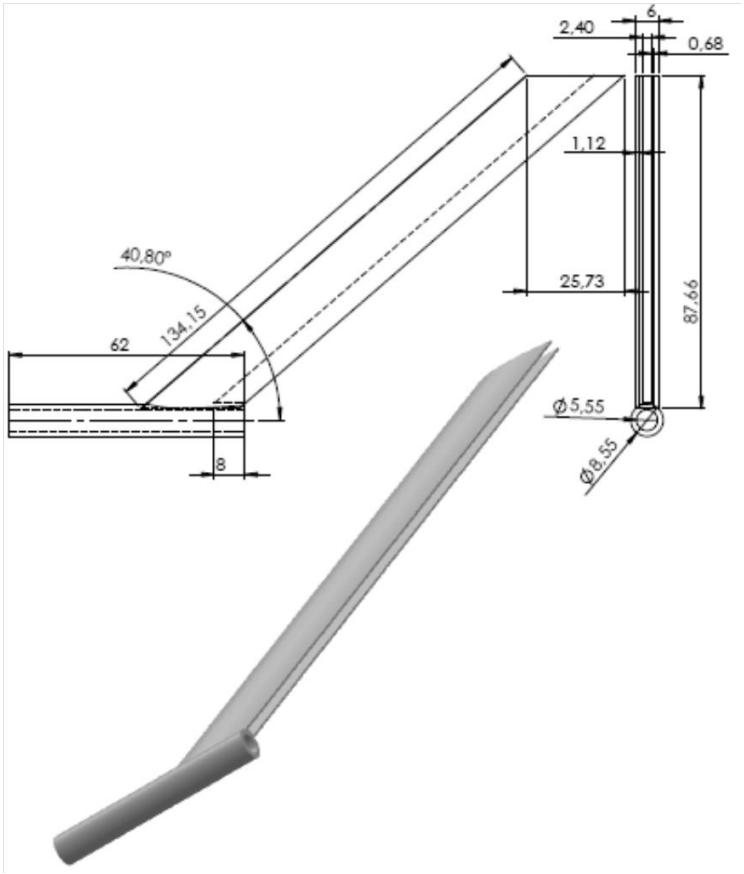

Figure 18. Inclined support with circular section in the straight part, scale 1:180

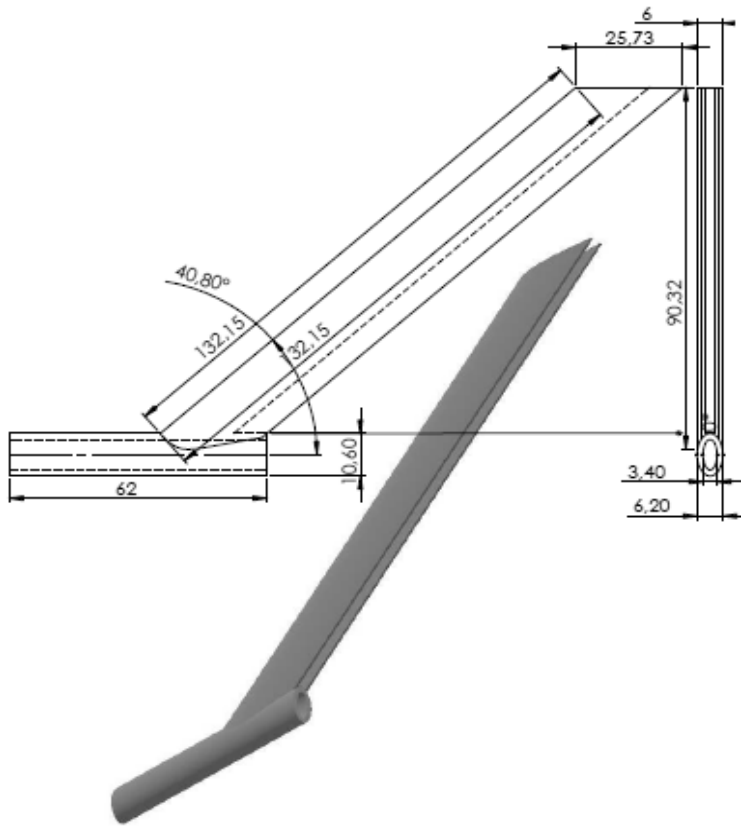

Figure 19. Inclined support with elliptic section in the straight part, scale 1:180.

It is useful to highlight, from the beginning, a remarkable difference between the design of the last two supports. In the circular one the inclined part is inserted in the sting only for a length of $\lambda = 2$ mm, otherwise in the elliptic sting the inclined part is in the sting for half of its height. This difference is due to the fact that in the circular sting the hole is larger and inserting more the superior part the force resisting area decrease dramatically. The short insertion in the circular sting may entail a larger stress concentration at the junction. See paragraph 4.2.3.1.

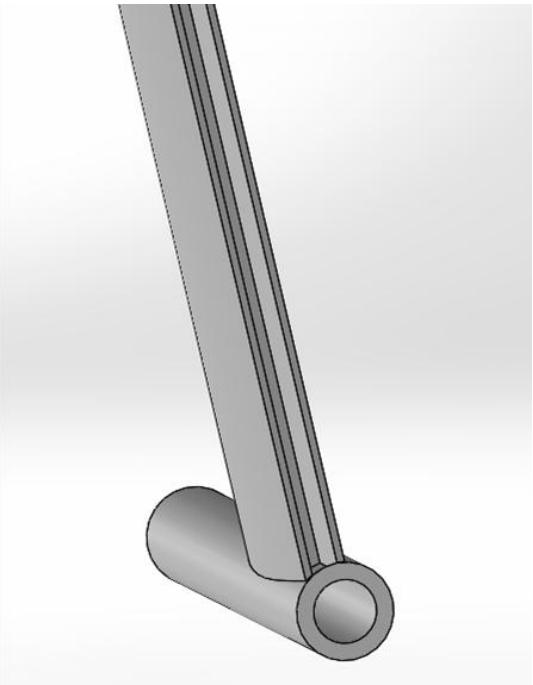

Figure 20. View of the support rear part, scale 1:180. It is possible to see the hole from where the cables come out from the sting and the slot where the cables come in the inclined bar.

3.4 Connection with the balance

No balances have already been built for the new wind tunnel test in both scales. The only balance available for the SOAR is in scale 1:180 and it was used for the previous wind tunnel test. It is not possible to use this device again because it was built to be connected with a completely different kind of sting (connection from the superior part). For this reason it has not been possible to perform the connection yet. Only to understand the feasibility and the typology of junction a connection with the previous balance, in scale 1:180, was performed. The same kind of connection can be used also in scale 1:80.

To realize this match the extremity of the balance was modified with a nut while at the end of the sting a threaded part (with a hole for the cables as in the sting) is added (See Figure 21).

For the elliptic sting a circular threaded part is joined with a fasteners to the sting (See Figure 22). It is useful to remember that these connections are only indicative.

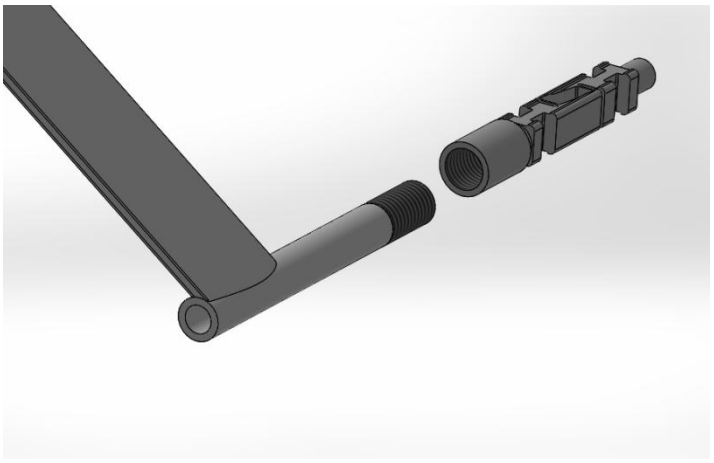

Figure 21. The sting and the balance before the connection, scale 1:180.

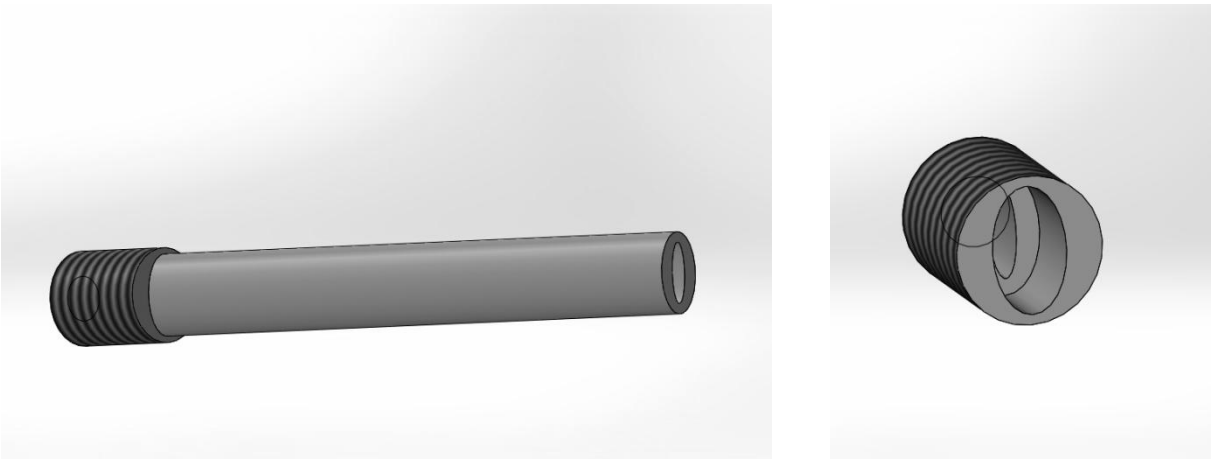

Figure 22. The elliptic sting with the threaded part for the connection, scale 1:80.

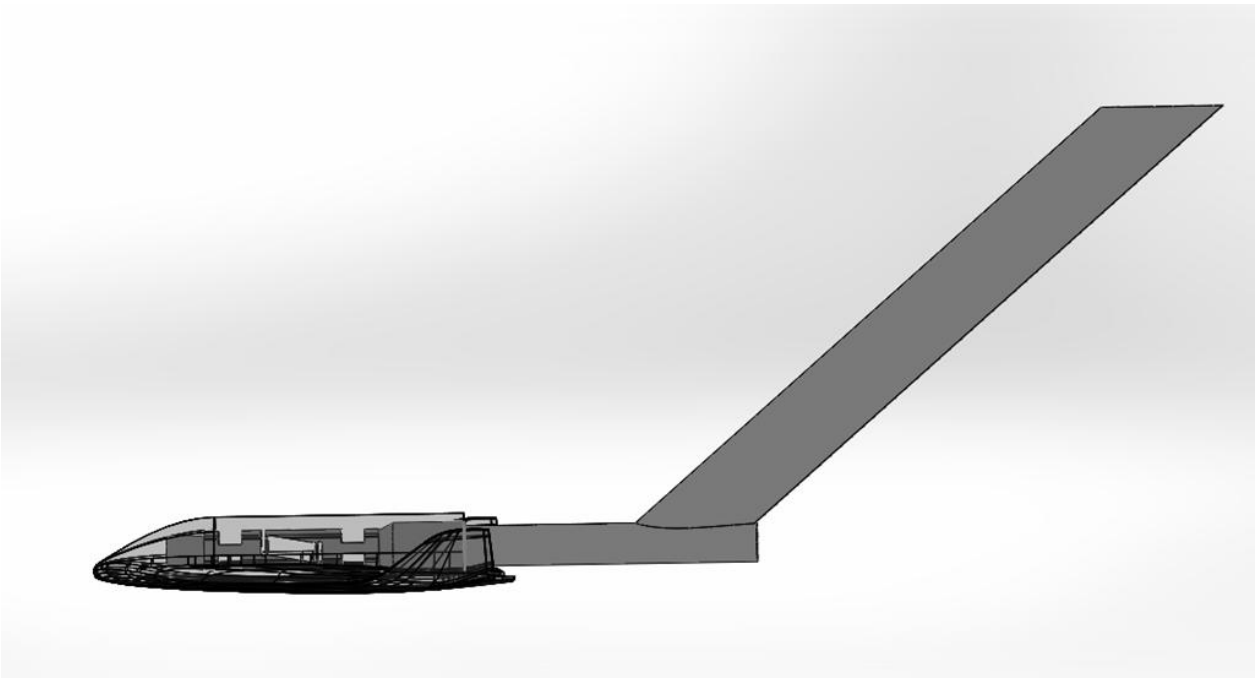

Figure 23. The sting connected to the balance inserted in the SOAR, scale 1:180.

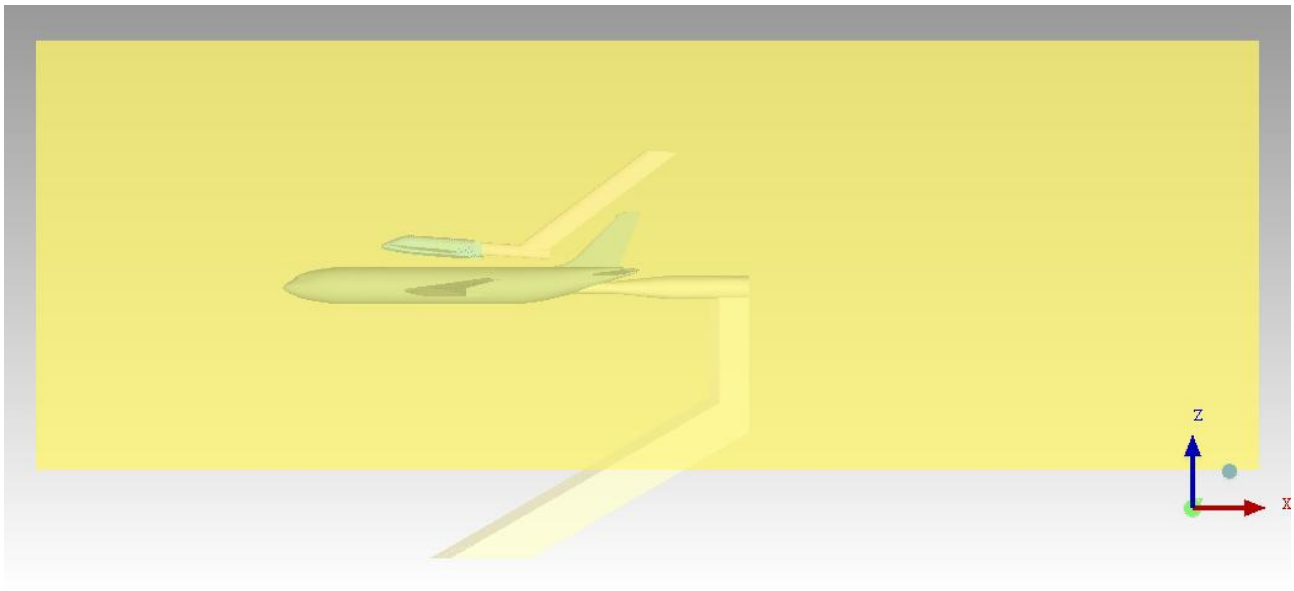

Figure 24. View of the completed configuration of the SOAR with the sting in the nominal position over the Airbus. It is also possible to see the wind tunnel test section contour. The sting used for the Airbus is the one of the previous wind tunnel test. This picture is from the CFD file; scale 1:180.

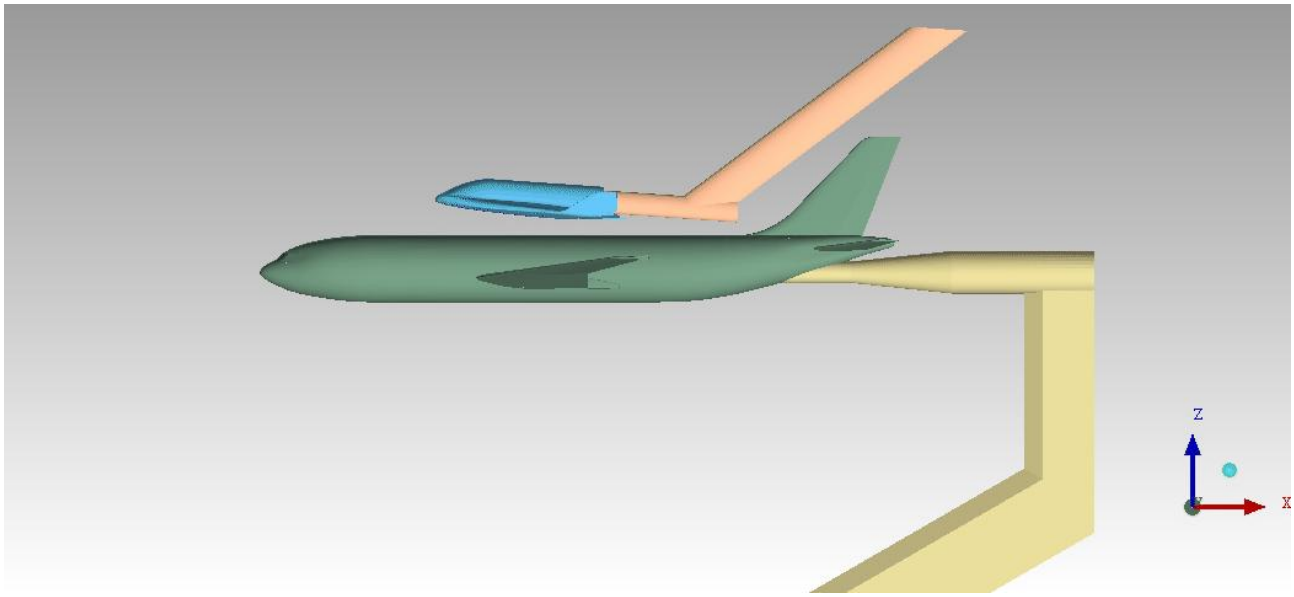

Figure 25. Zoom of the SOAR (light blue) with support (orange) over the Airbus (dark green) in the nominal position; scale 1:180.

4 Structural analysis

In this chapter there are the results of the static structural analysis and of the vibrational analysis of the supports. The analysis is done using the FEM method with the appropriate toolbox of Solidworks 2015 package. The goal of this analysis is to evaluate the reaction of different supports at the external loads present during the wind tunnel test.

For the Finite Element Method the sign convention and the frame of reference are the followings:

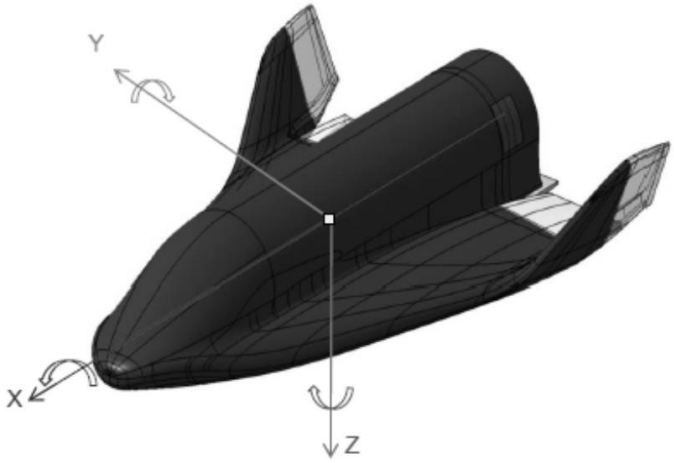

Figure 26. Sign convention.

4.1 Initial condition

In the next table the masses of every models are reported:

Table IV. Mass properties of each model. For the scale 1:80 model the total mass is the result of a proportion because this model is not built yet.

Model scale	Body [g]	Nose [g]	Balance [g]	Total mass [g]
1:180	64.6	2.5	13.8	80.9
1:80	Na	Na	Na	833,3

Furthermore the following loads descending from the previous wind tunnel test campaign are considered [1]. In the next tables only the magnitudes of forces and moment are reported, obviously the Fx and the Fz are negative and the My is a pitching up moment (positive).

Table V. Force and moment acting on the SOAR in relation with the Mach number; scale 1:80.

M	Fx[N]	Fz[N]	My[Nm]
0.50	10.66	26.65	0.31
0.60	14.39	35.98	0.42
0.70	17.75	44.38	0.52
0.75	19.75	49.38	0.58
0.80	21.23	53.08	0.62
0.85	23.19	57.97	0.68
0.90	24.35	60.88	0.71
2.00	9.14	22.85	0.27

Table VI. Force and moment acting on the SOAR in relation with the Mach number; scale 1:180.

M	Fx[N]	Fz[N]	My[Nm]
0.50	2.11	5.26	0.03
0.60	2.84	7.11	0.04
0.70	3.51	8.77	0.05
0.75	3.90	9.75	0.05
0.80	4.19	10.49	0.05
0.85	4.58	11.45	0.06
0.90	4.81	12.03	0.06
2.00	1.81	4.51	0.02

Where the Fx represent the drag force, Fz the lift force and My the pitching moment. It is necessary to consider also the moment due to the Fz at the extremity of the sting:

Table VII. Values of the moments due to the lift.

Scale	My_{Fz} [Nm]
1:80	5.742
1:180	0.79

The structural analysis, obviously, is done using the maximum values taken with an adequate safety margin[7]. Then the following values are used:

Table VIII. Values of forces and moment used for the simulation.

Scale	Fx[N]	Fz[N]	My_{ris} [Nm]
1:80	30.00	70.00	7
1:180	10.00	20.00	1.2

[7] In My_{Fz} is computed also an additional safety coefficient even though the moment is already calculated with a value of Fz taken with a safety margin.

Where $My_{ris} = My_{Fz} + My + \nu$

with ν that is a margin coefficient.

The material used in the simulation for all supports is a generic steel alloy with these characteristics:

Table IX. Properties of a generic steel alloy.

Properties	Values	Unit
Elastic module (E)	2.1•10^11	N/m^2
Poisson's ratio	0.28	N/A
Shear module	7.9•10^10	N/m^2
Mass density	7700	Kg/m^3
Tensile strength	7.238•10^8	N/m^2
Yield strength	6.204•10^8	N/m^2

At the beginning of the different supports (for the scale 1:180 model the beginning is the upper terminal part of the inclined support) a fixed constraint is applied, whereas the other extremity, where the vehicle will be joined is free.

In the composite device (scale 1:180) between the two parts (straight sting and inclined part) there is a rigid connection.

The mesh built is a standard mesh automatically generated by the Solidworks mesher. In the following table it is possible to find the general characteristics of each mesh.

Table X. Characteristics of the different meshes.

Model of support	1:80 circular sting	1:80 elliptic sting	1:180 inclined support with circular sting	1:180 inclined support with elliptical sting
Kind of mesher	Standard	Standard	Standard	Standard
Number of nodes	40538	34797	33069	31321
Number of elements	23891	20714	19367	18194
Element dimension [mm]	1.297	1.2670	1.8641	2.00

4.2 Results of the static analysis with the main loads

In this part the results of FEM simulations are reported and examined. For every model it is possible to see the stress, strain and displacement distributions. The external forces comport a plain stress and plain strain system in every case. The stress values are always Von Mises equivalent tensile stress, while the strain is the ESTRN equivalent strain and the displacement is the resultant displacement.

4.2.1 Scale 1:80 circular sting

The first support studied is the rectilinear sting in scale 1:80 for the wind tunnel test of the SOAR model alone.

4.2.1.1 Stress distribution

It is possible to see a stress concentration at the fixed constraint located at the beginning part of the sting (right). But the maximum stress value (Von Mises) is lower than the yielding one of the material with margin. Then it is expected that this stress distribution does not create any problem to the sting strength also for the not large time duration of each test.

$$\sigma_{max} = 1.24 \cdot 10^8 \text{ Pa} \quad \sigma_y = 6.20 \cdot 10^8 \text{ Pa}$$

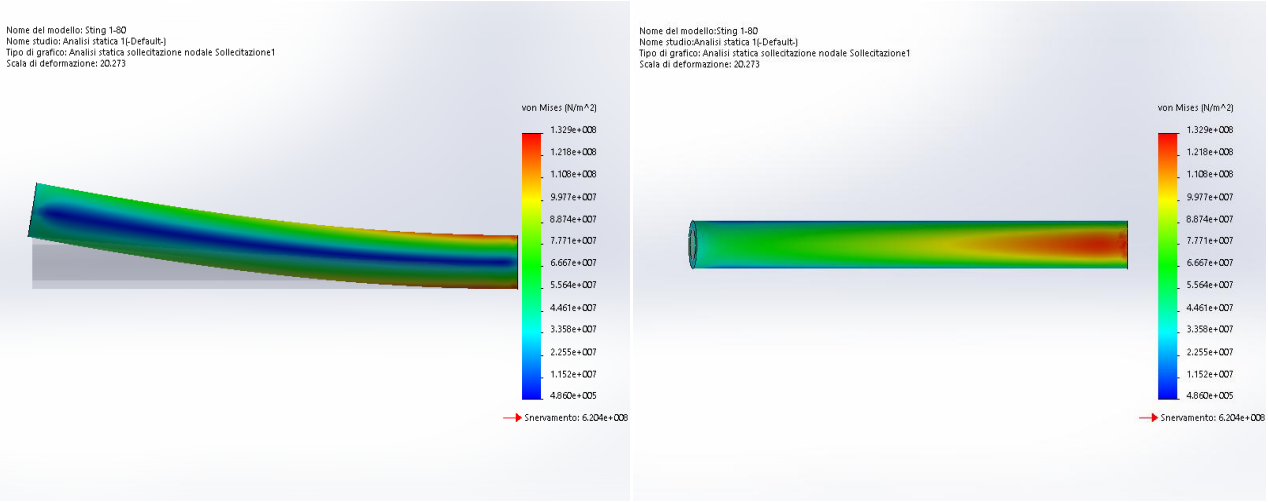

Figure 27. Lateral and top view of the circular sting stress distribution; scale 1:80.

4.2.1.2 Strain distribution

It is reported the equivalent strain (ESTRN) and its range is between $3.15 \cdot 10^{-6}$ and $5.15 \cdot 10^{-4}$. All these values are small enough not to be considered as a risk factor.

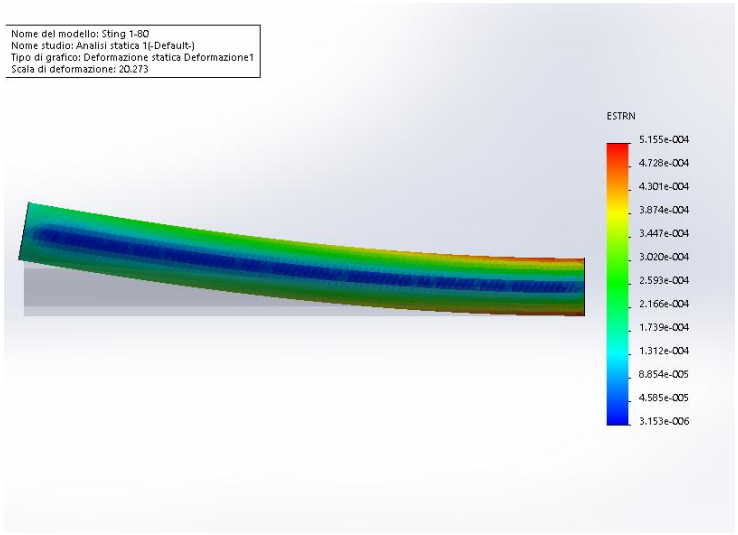

Figure 28. Lateral view of the circular sting strain distribution; scale 1:80.

4.2.1.3 Displacement distribution

After the structural analysis it results that the maximum displacement (resultant), as expected, is upward at the end of the sting (where the vehicle is attached) and it results:

$$\Delta z = 5.68 \cdot 10^{-1} \text{mm}$$

More important than this displacement is the bending angle of the sting extremity, where the SOAR is connected. In fact it is essential to know the variation of the model inclination induced by the load to have precise aerodynamics measurements in wind tunnel test. The meaning of this evaluation is only to know if it is possible to neglect or not this angle. Finally in the worse case if it is definitely too big it is not possible to avoid accurate wind tunnel measurement with the sting. For a calculation as realistic as possible, considering the fact that the bending of the sting is not uniform, the angle is calculated only on the last part of the sting, where the displacements are bigger[8].

Finally the resulting bending angle is $\theta = 0.46°$. This value is significant but acceptable and then it will be necessary to take into account it during the experiment. This estimation will be more precise during the calibration in the wind tunnel using strain gages positioned on the sting.

8 More in detail the bending angle is calculated between the maximum displacement (node 2155 with displacement $\Delta z = 5.68 \cdot 10^{-1}$mm) at the end of the sting and another point (node 15869 with displacement $\Delta z = 4.87 \cdot 10^{-1}$mm) located at 10 mm. The resulting angle is a mean angle yet but the average is done in a smaller length giving back a more realistic result. In this calculation there are the approximations of considering the displacements as only vertical and the strain is not take into account.

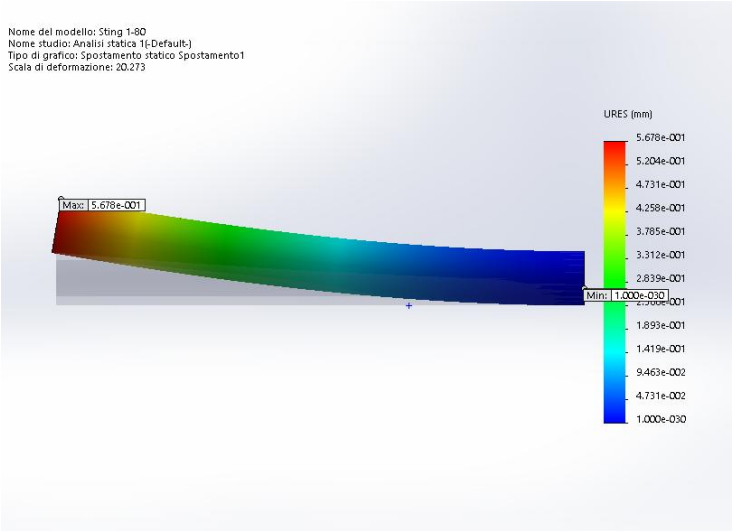

Figure 29. Lateral view of the displacement distribution, circular sting, scale 1:80.

4.2.2 Scale 1:80 elliptic sting

For the SOAR alone test, as written, also another possible shape of sting with an elliptic section is evaluated.

4.2.2.1 Stress distribution

For the elliptic sting it is immediately clear that the stresses are higher than with the circular one. The maximum stress (Von Mises) value is lower, with a good margin of safety yet, than the yield strength. Also in this case the stresses are bigger at the top (especially at the fixed constraint) than at the bottom. Afterwards, for the lower width of the sting, the peak of strength at the top and at the bottom is narrower than in the circular sting.

$$\sigma_{max} = 2.02 \cdot 10^8 \text{ Pa} \quad \sigma_y = 6.20 \cdot 10^8 \text{ Pa}$$

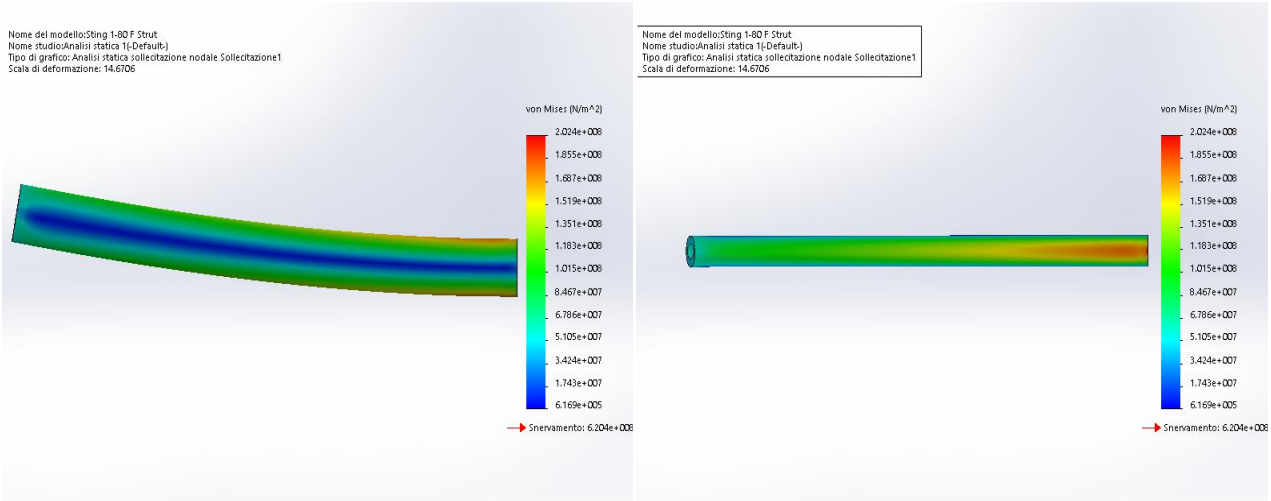

Figure 30. Lateral and top view of the elliptic sting stress distribution; scale 1:80.

4.2.2.2 Strain distribution

The equivalent strain (ESTRN) it is between $3.90 \cdot 10^{-6}$ and $7.51 \cdot 10^{-4}$. Also in this case all values are small enough for not to be considered as a risk factor.

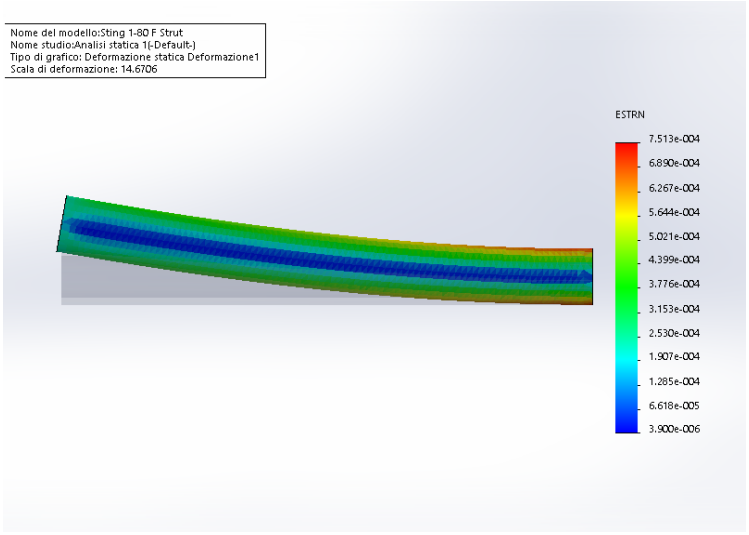

Figure 31. Lateral view of the elliptic sting strain distribution; scale 1:80.

4.2.2.3 Displacement distribution

It results that the maximum displacement (resultant) as expected is upward at the end of the sting (where it is attached at the vehicle) and it results:

$$\Delta z = 7.86 \cdot 10^{-1} \text{mm}$$

Also in this case the bending angle is calculated only in the last part of the sting where the displacements are larger and it result of $\theta = 0.67°$ [9]. These values are bigger than the bending angle of the circular sting, therefore, also in this case, it will be necessary to take into account it during the experiment.

[9] The bending angle is calculated between the maximum displacement (node 1937 with displacement $\Delta z = 7.86 \cdot 10^{-1}$mm) at the end of the sting and another point (node 16165 with displacement $\Delta z = 6.60 \cdot 10^{-1}$mm) located at 10.7 mm. In this measure the same consideration and approximations of footnote 8 are present.

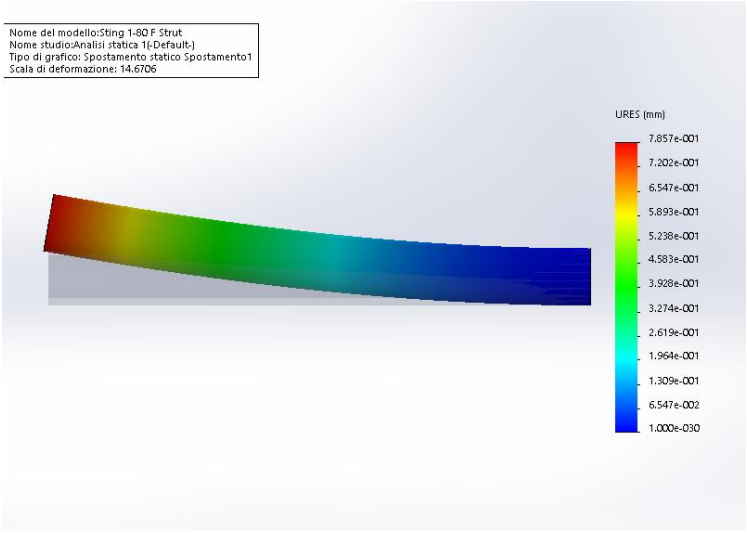

Figure 32. Lateral view of the displacement distribution, elliptic sting, scale 1:80

4.2.3 Scale 1:180 inclined support with circular sting

Now the results of the analysis on the supports for the scale 1:180 models (SOAR with Airbus test) will be reported, first with the circular sting in the rectilinear part, second with the elliptic one.

4.2.3.1 Stress distribution

The stress distribution presents a concentration at the junction between the straight sting and the inclined part. The maximum stress value (Von Mises) is more than one order of magnitude lower than the yielding values of the material and it is present only in a small region. For the most of the device, except for two areas at the superior and at the inferior surface of the straight sting, stresses are almost two orders of magnitude lower than the yield strength. Other peaks of stress of about a half of the maximum value are located at the upper fixed constraint and in the back of the airfoil plant of the inclined part. Then it is expected that this stress distribution does not create any problems during the experiment.

$$\sigma_{max} = 5.71 \cdot 10^{7}\ \text{Pa} \quad \sigma_{y} = 6.20 \cdot 10^{8}\ \text{Pa}$$

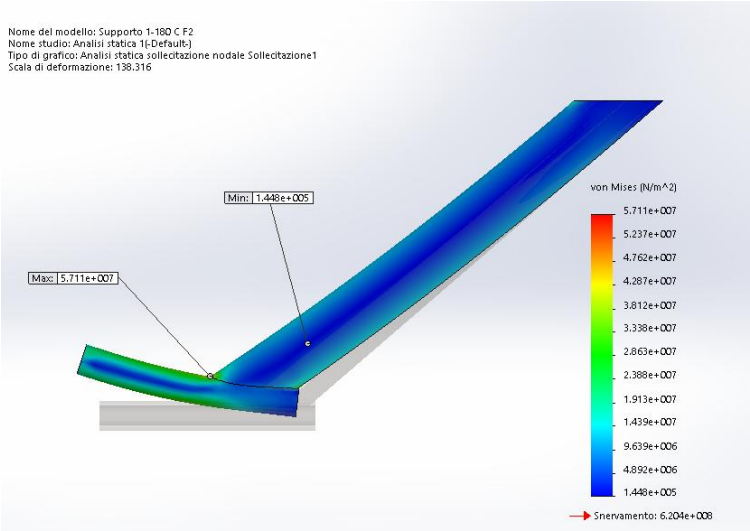

Figure 33. Lateral view of the stress distribution, inclined support with circular sting, scale 1:180.

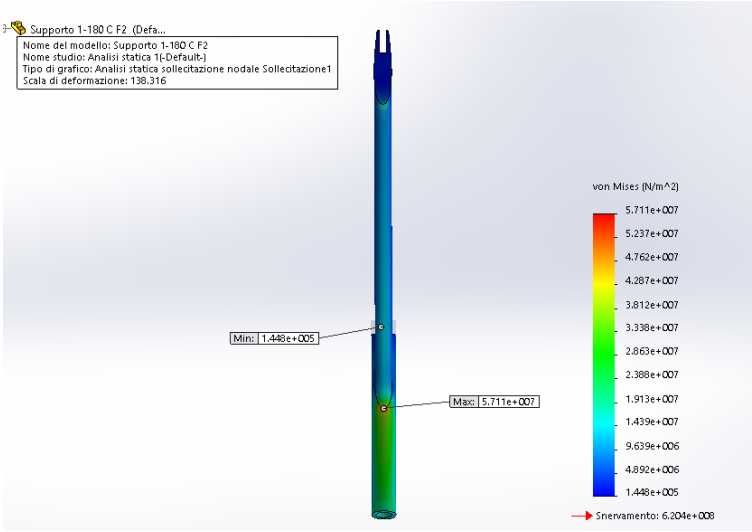

Figure 34. Top view of the stress distribution, inclined support with circular sting, scale 1:180. It is possible to see the maximum stress at the junction between the inclined part and the sting and the small area of high stress at the upper fixed constraint.

4.2.3.2 Strain distribution

The equivalent strain (ESTRN) it is between $6.26 \cdot 10^{-7}$ and $1.73 \cdot 10^{-4}$. All these values are small enough not to be considered as a risk factor.

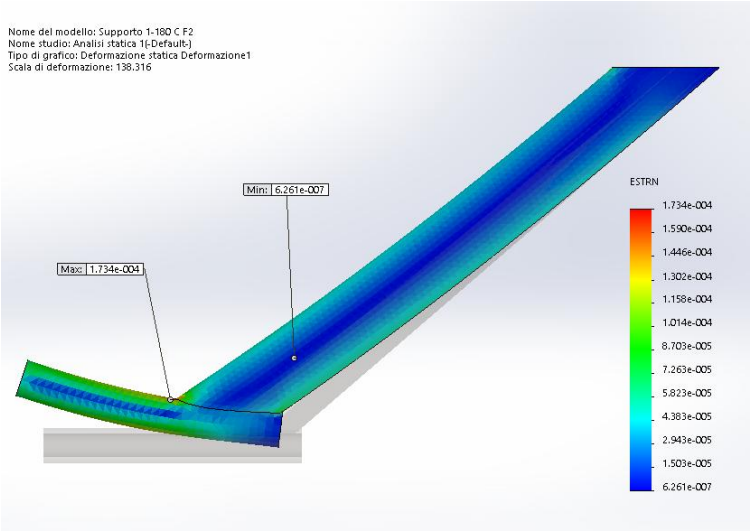

Figure 35. Lateral view of the strain distribution, inclined support with circular sting; scale 1:180.

4.2.3.3 Displacement distribution

The maximum displacement (Resultant) once again is upward at the end of the rectilinear sting (where the vehicle is attached) and it results:

$$\Delta z = 1.26 \cdot 10^{-1} \text{mm}$$

The bending angle for the rectilinear sting is calculated in the same way as at paragraphs 4.2.1.3 and 4.2.2.3. It results $\theta = 0.12°$ [10]. The value is lower than the previous cases, but also in this case it is not small enough to be negligible during the wind tunnel test. Furthermore the same angle is calculated also for the inclined part and it results $\theta = 0.05°$ [11] (see Figure 36and Figure 37).

4.2.4 Scale 1:180 inclined support with elliptic sting

Also for the separation test in the configuration with the SOAR and the Airbus carrier the possibility to use an elliptic sting for the rectilinear part of the support is investigated. The inclined bar is the same of the previous example. Once again a deep analysis is necessary for the short literature about elliptic sting.

[10] The bending angle is calculated between the maximum displacement (node 23658 with displacement $\Delta z = 1.26 \cdot 10^{-1}$mm) at the end of the sting and another point (node 22908 with displacement $\Delta z = 1.05 \cdot 10^{-1}$mm) located at 10 mm from the previous one. In the measure the same considerations and approximations of footnotes 8 and 9 are present.

[11] In this case the bending angle is calculated between the maximum displacement in the inclined part, located at the bottom, (node 32479 with displacement $\Delta z = 5.98 \cdot 10^{-2}$mm) and another point (node 32519 with displacement $\Delta z = 5.09 \cdot 10^{-2}$mm) located in a line with the same inclination of the support at 10.2 mm from the previous one. The approximations in this measure are that the displacements are considered both normal at the base line with the two points and the deformation is not take into account (See Figure 37).

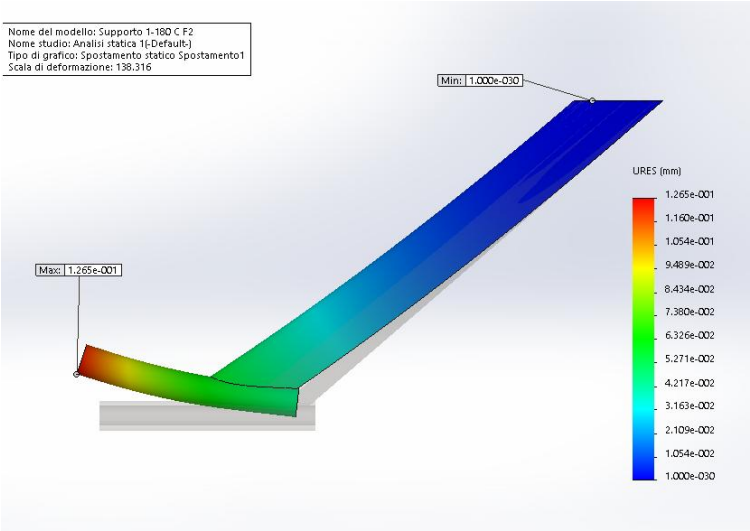

Figure 36. Lateral view of the displacement distribution, inclined support with circular sting; scale 1:180.

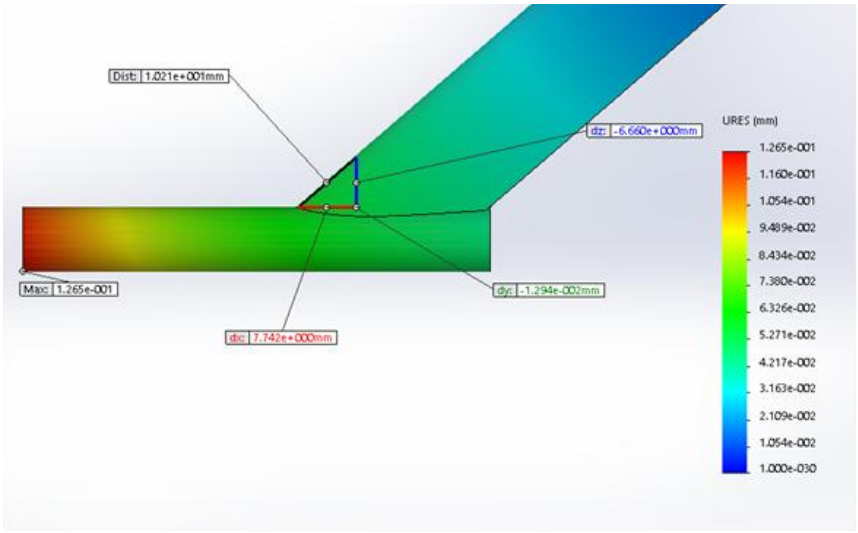

Figure 37. Representation of the two nodes used for measure the bending angle for the inclined part. Inclined support with circular sting; scale 1:180

4.2.4.1 Stress distribution

With respect to the circular sting (paragraph 4.2.3.1) the stress distribution is similar. In this case the maximum stress value (Von Mises), located in the same zone of the previous case, is slightly lower. This last fact may be due to the insertion of the inclined part in a longer distance than it happens for the previous support (See paragraph 3.3). Anyway all the stresses are lower with margin than the yielding value. Also in this case it is expected that this margin will be enough considering further the time duration of the experiment.

$$\sigma_{max} = 5.64 \cdot 10^7 \text{ Pa} \quad \sigma_y = 6.20 \cdot 10^8 \text{ Pa}$$

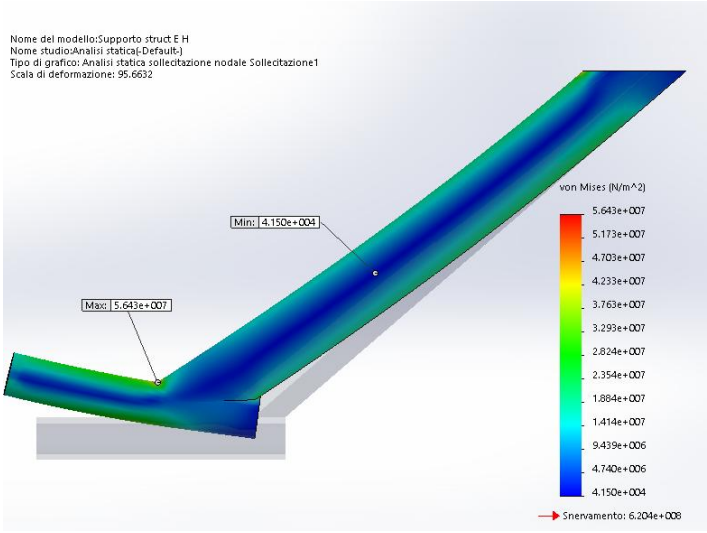

Figure 38. Lateral view of the stress distribution, inclined support with elliptic sting, scale 1:180.

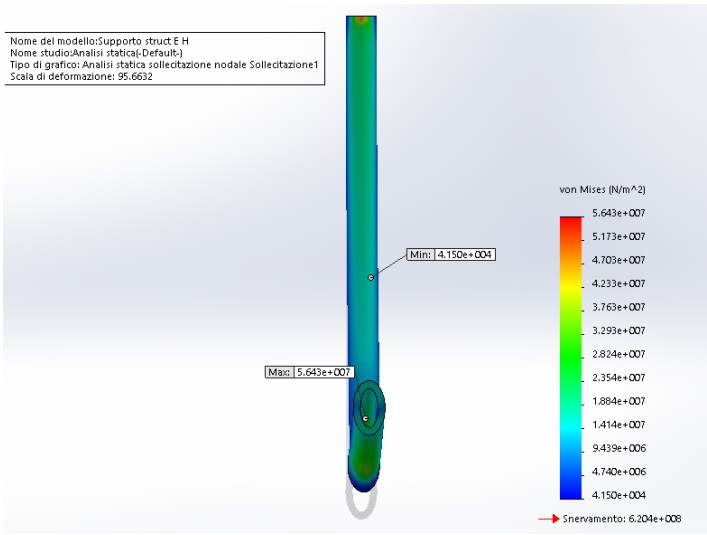

Figure 39. Front view of the stress distribution, inclined support with elliptic sting, scale 1:180.

4.2.4.2 Strain distribution

The equivalent strain (ESTRN) is between $1.94 \cdot 10^{-7}$ and $1.64 \cdot 10^{-4}$, slightly lower than the previous case, paragraph 4.2.3.2. All these values are small enough not to be considered as a risk factor (see Figure 40).

4.2.4.3 Displacement distribution

The maximum displacement (Resultant) as expected is upward at the end of the sting (where the vehicle is attached) and it results:

$$\Delta z = 1.90 \cdot 10^{-1} \text{mm}$$

The bending angle for the rectilinear sting is calculated in the same way as the previous cases. It results $\theta = 0.13°$ [12] and for this value the same consideration of the preceding paragraphs about displacement are valid. Furthermore the same angle is calculated also for the inclined part and it results $\theta = 0.12°$ [13]. All displacements are greater than the inclined support with circular sting, especially for the inclined bar and it will be necessary to take them into account (see Figure 41).

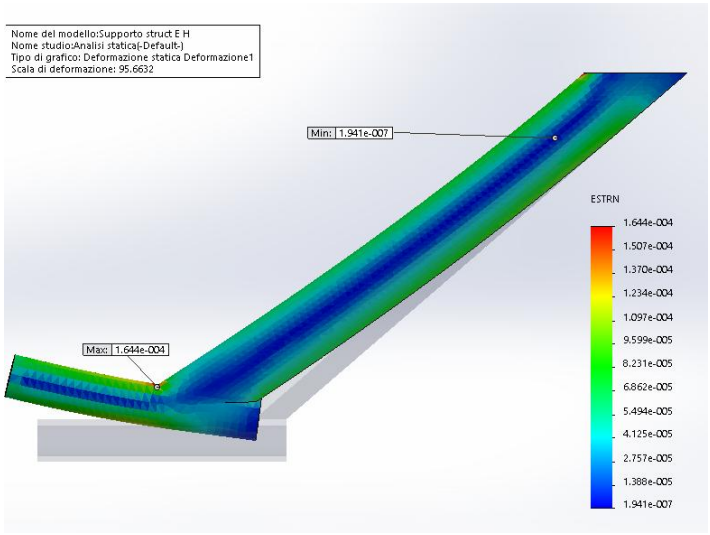

Figure 40. Lateral view of the strain distribution, inclined support with elliptic sting, scale 1:180.

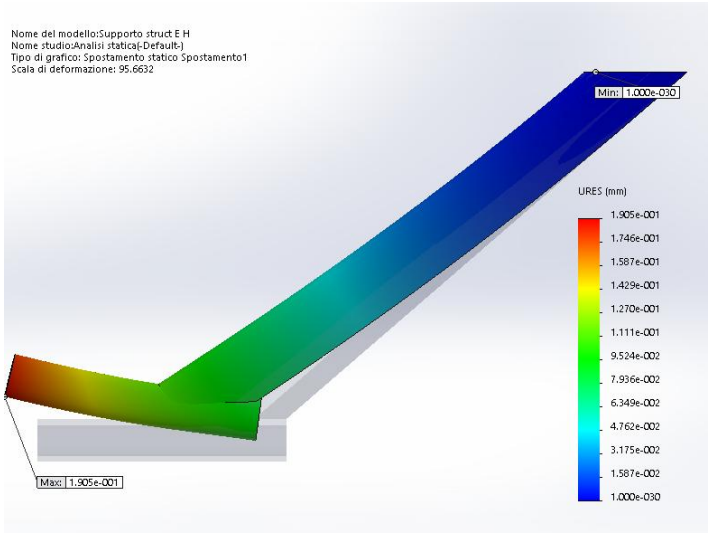

Figure 41. Lateral view of the displacement distribution, inclined support with elliptic sting, scale 1:180.

[12] The bending angle is calculated between the maximum displacement (node 386 with displacement $\Delta z = 1.90 \cdot 10^{-1}$mm) at the end of the sting and another point (node 427 with displacement $\Delta z = 1.68 \cdot 10^{-1}$mm) located at 10 mm from the previous one. The same considerations of the previous footnotes are valid again.

[13] In this case the bending angle is calculated between the maximum displacement in the inclined part, located at the bottom, (node 345 with displacement $\Delta z = 1.12 \cdot \mathbf{10^{-1}}$mm) and another point (node 26966 with displacement $\Delta z = 9.66 \cdot \mathbf{10^{-1}}$mm) located in a line with the same inclination of the support at 10.85 mm from the previous one. The same considerations and approximations of footnote 11 are present. See Figure 37 yet as an explication of measurement technique.

4.3 Lateral forces

For the next wind tunnel test campaign the possibility of evaluate the performance of the SOAR vehicle in presence of lateral forces may be requested. This because in the mission profile it might be that the SOAR turn in the following instant after the separation moment. Therefore it is necessary to know the behaviour of the support in presence of lateral forces and then the successive forces are taken into account in this simulation.

Table XI. Lateral forces used in the simulations. These forces do not come from previous wind tunnel tests but are estimated with an adequate safety margin.

Scale	F_y [N]
80.00	50
180.00	15

4.3.1 Results of the static analysis with the lateral force

In this paragraph the results of the simulations with the lateral forces are reported. Once again the stress values are always Von Mises equivalent tensile stress, while the strain is the ESTRN equivalent strain. It must be emphasized that the lateral forces are taken into account in addition to the forces already considered in chapter 4 to obtain all results, except for the lateral displacement that is calculated with only the lateral force F_y.

4.3.1.1 Scale 1:80 circular sting

The impact of the lateral force on the stress distribution is small enough not to require a particular attention. Obviously the maximum stress (Von Mises) is a little increased and the peak areas, in the superior and in the inferior part, are slightly rotated in the direction of the force.

$$\sigma_{max} = 1.65 \cdot 10^8 \text{ Pa} \quad \sigma_y = 6.20 \cdot 10^8 \text{ Pa}$$

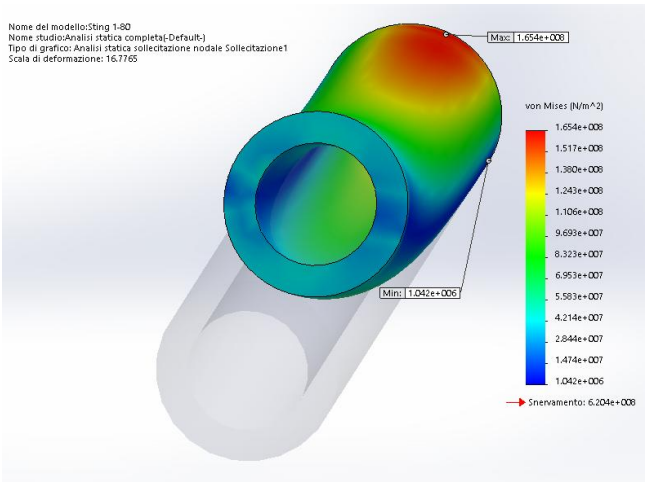

Figurer 42. Front view of the stress distribution in the circular sting; scale 1:80.

The strain distribution does not change significantly, all values of the equivalent strain (ESTRN) are between $5.05 \cdot 10^{-6}$ and $6.66 \cdot 10^{-4}$and then it is possible to neglect them again.

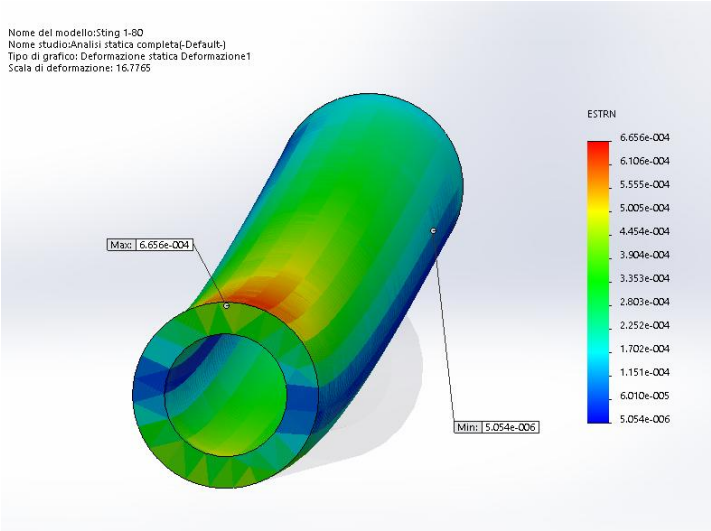

Figure 43. Rear view of the strain distribution in the circular sting; scale 1:80.

A simulation with only the lateral force is made for calculate the lateral displacement, then also the total bent shape is reported. The bending angle is calculated in the same way of the previous paragraphs and it result $\theta = 0.12°$ [14].

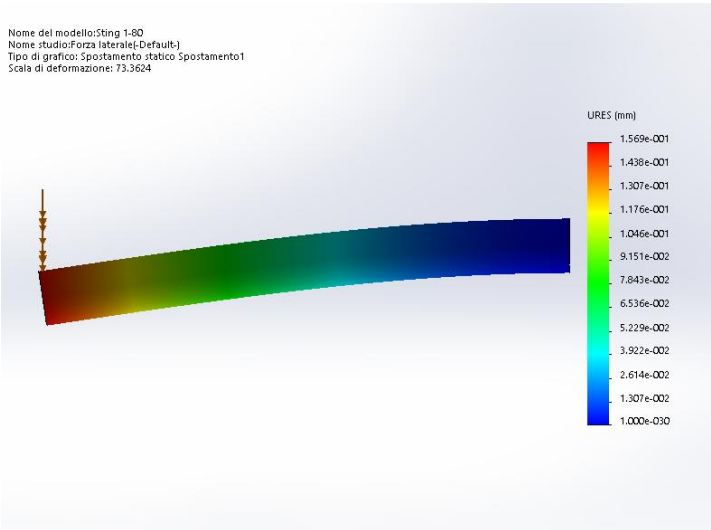

Figure 44. Top view of the displacement distribution, circular sting, scale 1:80. This picture shows the displacement due to only the lateral force.

[14] The bending angle is calculated between the maximum displacement (node 1445 with displacement $\Delta y = 1.57 \cdot 10^{-1}$mm) and another point (node 1996 with displacement $\Delta y = 1.37 \cdot 10^{-1}$mm) located at 10 mm in the length direction from the previous one. Also now the resulting angle is a mean angle, the displacement is considered only lateral and the strain is not taken into account.

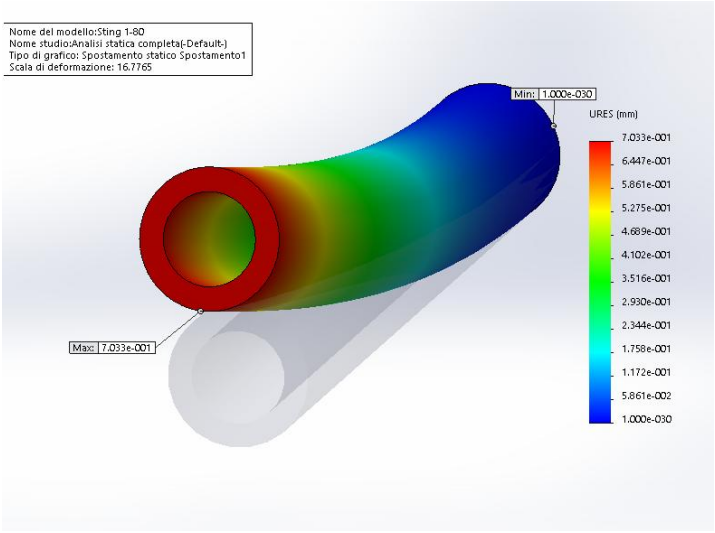

Figure 45. View of displacement due to the total forces, circular sting, scale 1:80

4.3.1.2 Scale 1:80 elliptic sting

Also in this case the impact of the lateral forces on the stress distribution is small enough not to require a particular attention. The maximum stress (Von Mises) is a little increased and the peak areas, in the superior and in the inferior part, are rotated, mainly than for the circular sting, in the direction of the force.

$$\sigma_{max} = 2.14 \cdot 10^8 \text{ Pa} \quad \sigma_y = 6.20 \cdot 10^8 \text{ Pa}$$

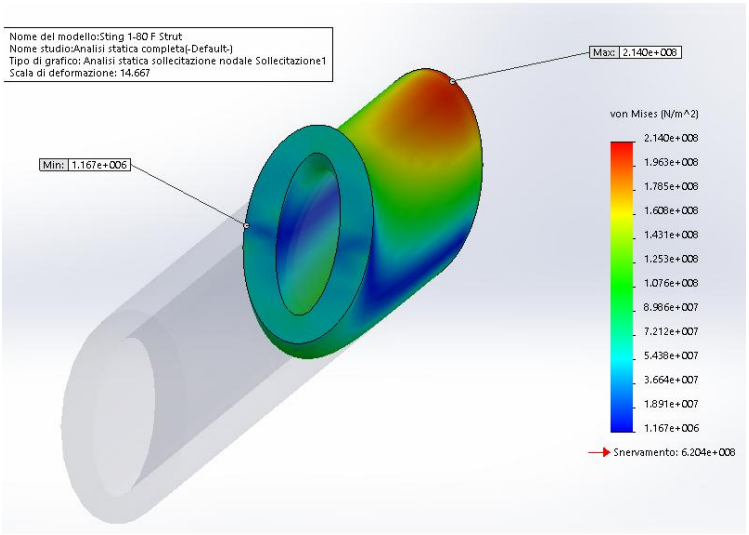

Figure 46. View of the stress distribution in the elliptic sting, scale 1:80.

The strain distribution is negligible yet, all values of the equivalent strain (ESTRN) are between $4.81 \cdot 10^{-6}$ and $8.21 \cdot 10^{-4}$.

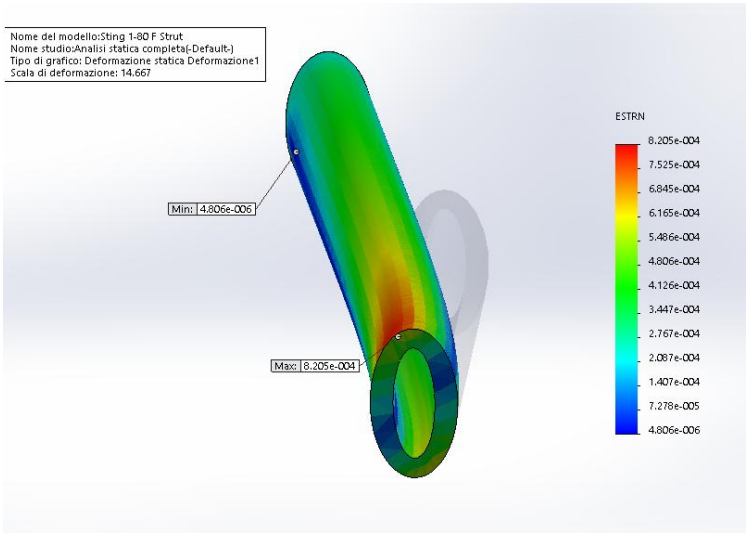

Figure 47. Rear view of the strain distribution in the elliptic sting, scale 1:80.

Once again the displacement are the most critical point. A simulation with only the lateral force taken in account is made to evaluate the lateral displacement. Then also the total bent shape is reported. The bending angle is calculated in the same way of the previous paragraphs and it result $\theta = 0.46°$ [15].

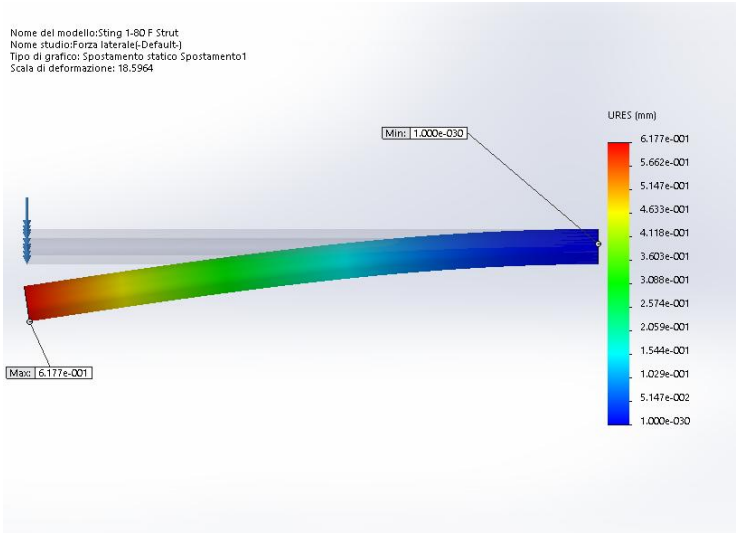

Figure 48. Top view of the displacement distribution, elliptic sting, scale 1:80. This picture shows the displacement due to only the lateral force.

[15] The bending angle is calculated between the maximum displacement (node 9126 with displacement $\Delta y = 5.88 \cdot 10^{-1}$mm) and another point (node 8040 with displacement $\Delta y = 5.01 \cdot 10^{-1}$mm) at 10.05 mm in the length direction from the previous one. The same approximations of footnote 14 are present.

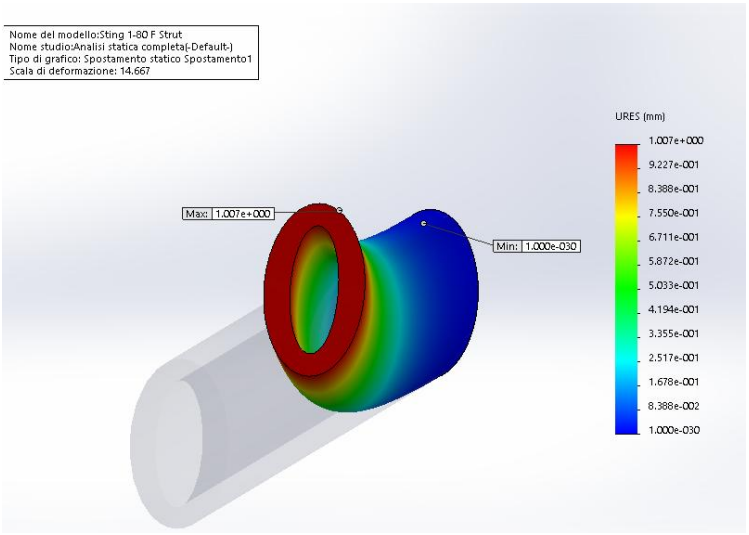

Figure 49. View of displacement due to the total forces, elliptic sting, scale 1:80.

4.3.1.3 Scale 1:180 inclined support with circular sting

The addition of the lateral force increases the maximum stress (Von Mises) value and involves a rotation of the high stress areas with now a larger part of the support affected by important stresses. Anyway all values are lower with margin than the yielding one and this stress distribution should not create any problems also for the short time duration of the experiment.

$$\sigma_{max} = 9.18 \cdot 10^7 \text{ Pa} \quad \sigma_y = 6.20 \cdot 10^8 \text{ Pa}$$

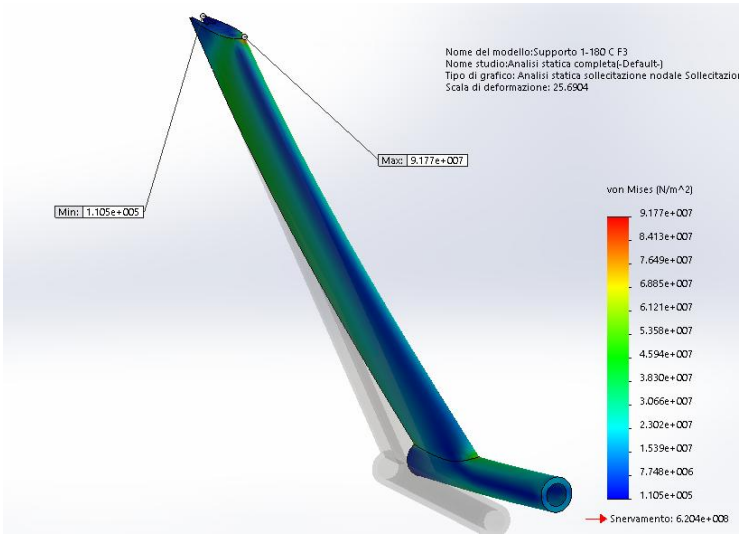

Figure 50. Lateral view of the stress distribution, inclined support with circular sting, scale 1:180.

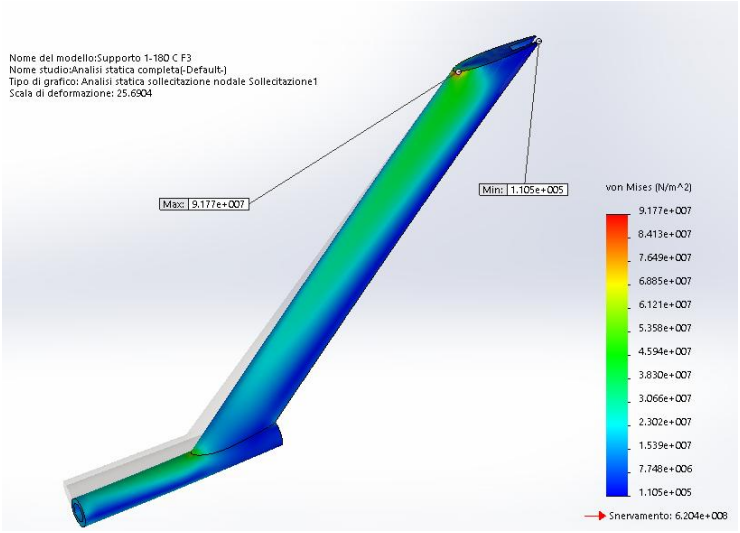

Figure 51. Lateral view of the stress distribution, inclined support with circular sting, scale 1:180. From the comparison between this two pictures and Figure 33 it is possible to see the effect of the lateral force in the rotation of the stress distribution.

Once again the strain distribution is negligible, all values of the equivalent strain (ESTRN) are between $5.36 \cdot 10^{-6}$ and $2.78 \cdot 10^{-4}$.

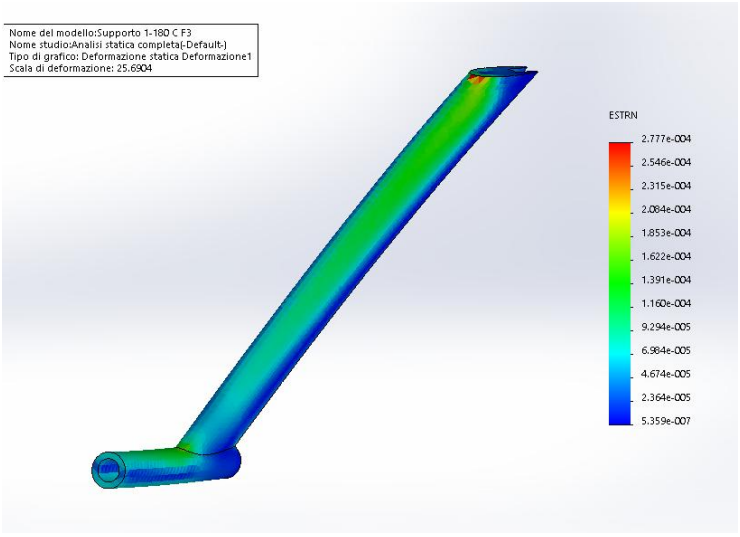

Figure 52. View of the strain distribution, inclined support with circular sting, scale 1:180.

In regard to the displacement only the lateral displacement of the sting (and not the displacement of the inclined bar) is considered as a significant value and it is calculated taking into account only the lateral force. The bending angle is calculated in the same way of the previous paragraphs and it results $\theta = 0.27°$ [16]. Then also the total bent shape is reported.

[16] The bending angle is calculated between the maximum displacement (node 21793 with displacement $\Delta y = 6.31 \cdot 10^{-1}$mm) and another point (node 21156 with displacement $\Delta y = 5.83 \cdot 10^{-1}$mm) located in a line with the same inclination of the support at 10.05 mm from the previous one. The same approximations of footnote 14 and 15 are present.

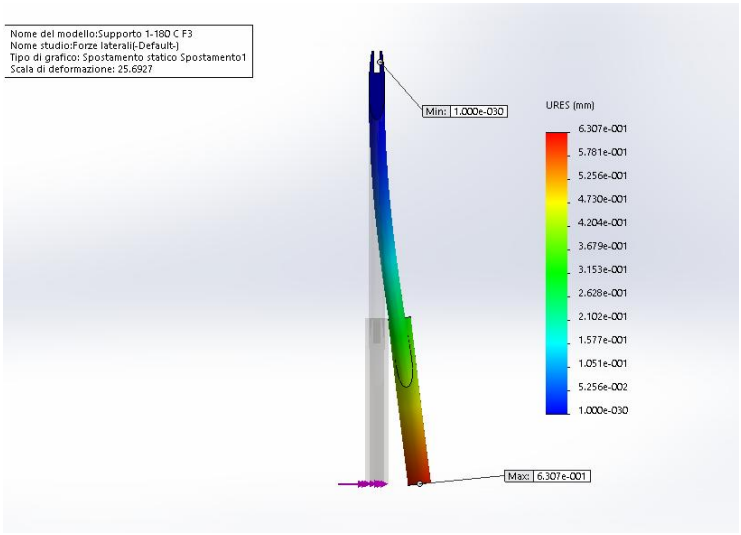

Figure 53. Top view of the displacement distribution for the inclined support with circular sting; scale 1:180. This picture shows the displacement due to only the lateral force.

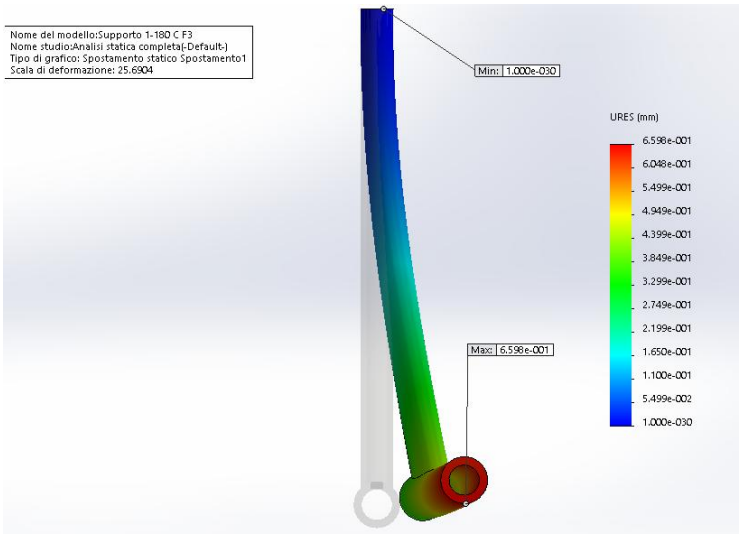

Figure 54. View of the displacements due to the total forces, inclined support with elliptic sting, scale 1:180.

4.3.1.4 Scale 1:180 inclined support with elliptic sting

The addition of the lateral force increases the maximum stress value (Von Mises) and involves a rotation of the front and rear high stress areas in the direction of the lateral force. Therefore a larger part of the support suffers more important stresses. Anyway all values are lower than the yielding one and this stress distribution should not create any problems also for the short time duration of the experiment.

$$\sigma_{max} = 9.70 \cdot 10^7 \text{ Pa} \quad \sigma_y = 6.20 \cdot 10^8 \text{ Pa}$$

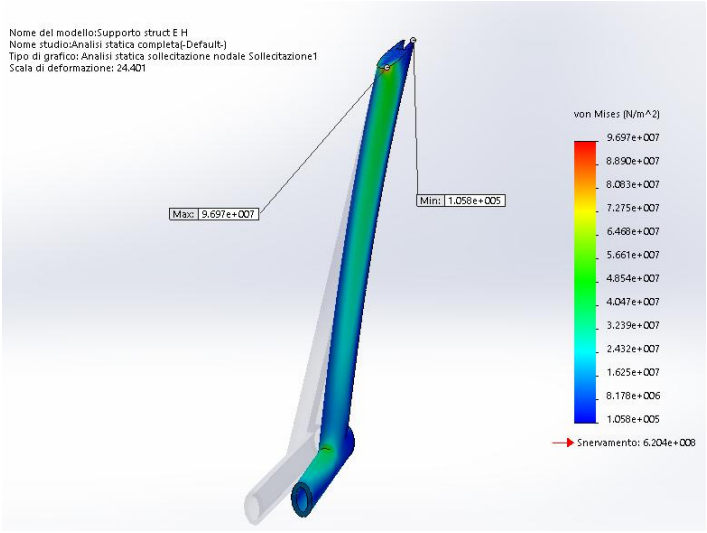

Figure 55. View of the stress distribution, inclined support with circular sting; scale 1:180.

The strain distribution is negligible again, all values of the equivalent strain (ESTRN) are between $6.76 \cdot 10^{-7}$ and $2.92 \cdot 10^{-4}$.

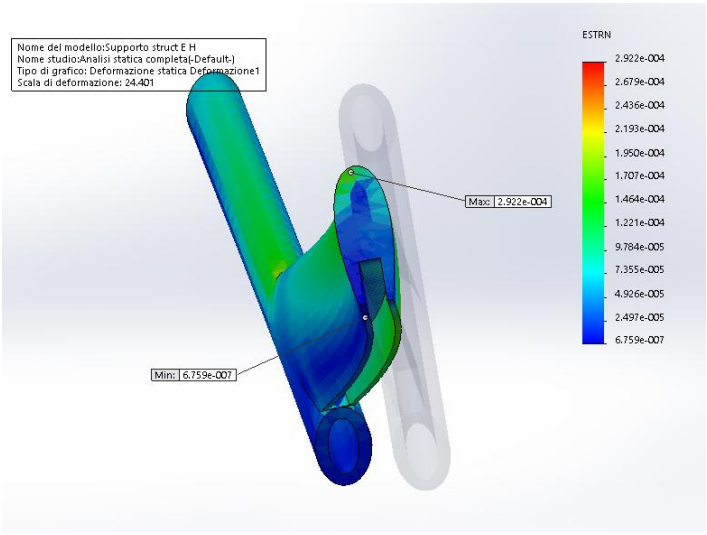

Figure 56. View of the strain distribution, inclined support with circular sting; scale 1:180.

In the same way of the paragraph 4.3.1.3 only the lateral displacement of the sting is considered and it is calculated taking into account only the lateral force. The bending angle is calculated again as in the previous paragraphs and it results $\theta = 0.30°$ [17]. Then also the total bent shape is reported.

[17] The bending angle is calculated between the maximum displacement (node 386 with displacement $\Delta y = 6.48 \cdot 10^{-1}$mm) and another point (node 427 with displacement $\Delta y = 5.96 \cdot 10^{-1}$mm) located in a line with the same inclination of the support at 10 mm from the previous one. The same approximations of footnote 14, 15 and 16 are present.

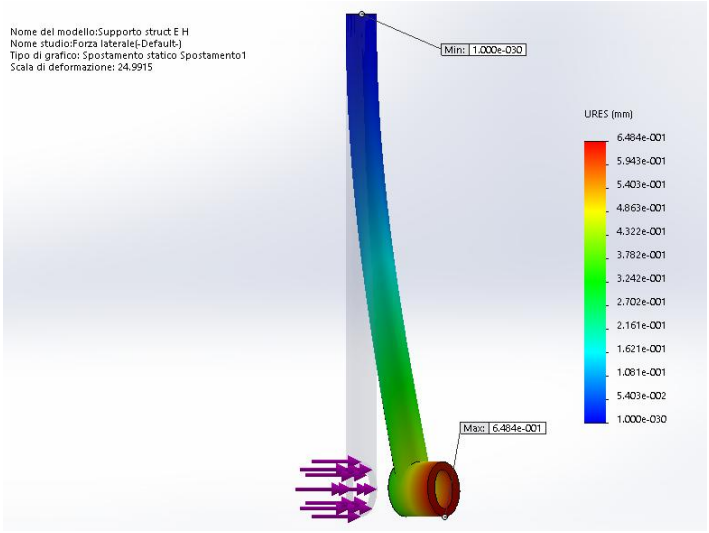

Figure 57. Front view of the displacement distribution for the inclined support with circular sting, scale 1:180. This picture shows the displacement due only to the lateral force.

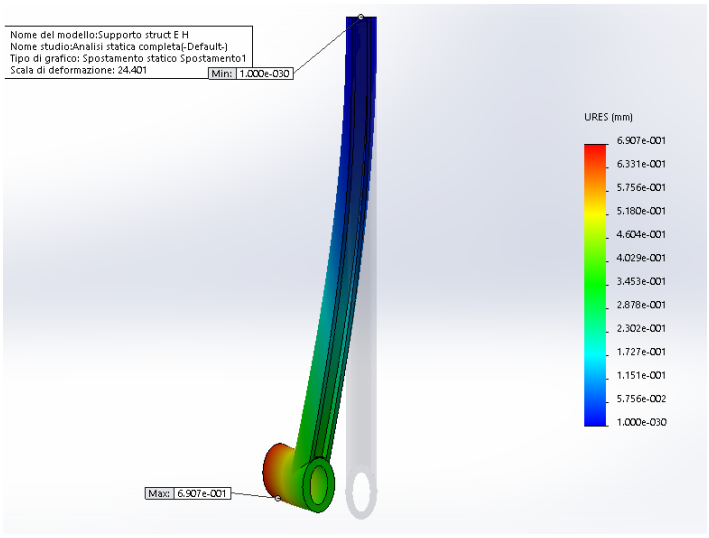

Figure 58. View of displacement due to the total forces, inclined support with elliptic sting, scale 1:180.

4.4 Frequency analysis

The frequency analysis is done applying a mass with the same weight of the wind tunnel model at the end of the support and a fixed constraint at the other extremity[18]. The aim of this analysis is to make sure that the excitation frequencies during the experiments will be far enough from the resonance frequency of the support. The main vibrational external disturbance for the stings is the frequency of the vortex shedding of the SOAR model. These stings are not designed for forced oscillation tests but it is interesting to evaluate their performance also in this circumstance. In case of a positive response it will be possible to get a qualification for this kind of experiments too. These frequencies are calculated thanks to dimensional analysis with a similarity law between the flight vehicle and the model in the wind tunnel. It is considered a system with one degree of freedom system, described by the following equation:

$$I\ddot{\theta} - \left(C_{m_q} + C_{m_{\dot{\alpha}}}\right)\frac{q_\infty SD^2}{2U_\infty}\dot{\theta} - q_\infty SD\frac{\partial C_m}{\partial \theta}\theta = M(t) \quad (2)$$

with:

$$C_{m_{\dot{\alpha}}} = \frac{\partial C_m}{\partial \frac{\dot{\alpha} D}{U_\infty}} \quad \text{and} \quad C_{m_q} = \frac{\partial C_m}{\partial \frac{\dot{\theta} D}{U_\infty}}$$

where:

I is the SOAR moment of inertia around the pitching axis, $I_{yy} = 92466\ Kgm^2$ [19]

θ is the pitch angle

α is the angle of attack

C_m is the pitch moment coefficient

q_∞ is the free stream dynamic pressure

S is the SOAR reference area, S = 87.98 m^2

D is the SOAR characteristic length, D = 17 m

U_∞ is the total free stream velocity

M(t) is the external forcing moment as function of time.

Solving this second order differential equation, for the flight vehicle (*ft*) it is possible to obtain the following solution:

[18] It is useful to remember that this is a not negligible approximation because in reality the extremity of the support is not fixed but it is jointed to a mechanical arm that arrange the sting in the correct position. Then the real natural frequency of the supports will be slightly lower than what is measured in this analysis.

[19] For all data about the SOAR vehicle see [9].

$$(\omega_n)_{ft} = \left(\sqrt{\frac{q_\infty SD \left|\frac{\partial C_m}{\partial \theta}\right|}{I} - \left(\frac{q_\infty SD \left(C_{m_q} + C_{m_{\dot{\alpha}}} \right)}{2I} \right)^2} \right)_{ft}$$

(3)

Where the second term is negligible and $q_\infty = \frac{1}{2}\rho_\infty U_\infty^2$.

To reproduce the dynamic behaviour of the wind tunnel model it is necessary to apply a similitude law with the Strouhal number which is a dimensionless coefficient:

$$S_t = \frac{\nu D}{U_\infty}$$

(4)

Where ν is the frequency of the oscillation.

This dimensionless coefficient has to be the same for the real vehicle and for the wind tunnel model. Therefore it is possible to rewrite the Strouhal number for the flight vehicle as:

$$S_t = \left(\frac{\omega_n D}{2\pi U_\infty}\right)_{ft} = \left(\sqrt{\frac{\rho_\infty SD^3 \left|\frac{\partial C_m}{\partial \theta}\right|}{8\pi^2 I}} \right)_{ft}$$

(5)

Matching this equation with the expression of the Strouhal number for the wind tunnel model (*exp*) it is possible to obtain the following expression:

$$\nu = \left(\frac{1}{2\pi} \sqrt{\frac{\rho_\infty SD^3 \left|\frac{\partial C_m}{\partial \theta}\right|}{2I}} \right)_{ft} \left(\frac{U}{D}\right)_{exp}$$

(6)

From the equation (6) it is possible to calculate the external frequencies acting on the sting due to the forced oscillations of the vehicle. In this calculation the reference conditions of Table XII and Table XIII are used.

The derivative of the pitching moment coefficient is obtained from the previous wind tunnel campaign data. It is reported here in Figure 59 and in the tabulated data in ANNEX C [20].

[20] The choice to use the wind tunnel data is an acceptable approximation necessary because not flight data are available. For all data from the previous wind tunnel testing see [1].

Table XII. Free stream reference condition for the SOAR vehicle based on the U.S. Standard Atmosphere 1976.

Mach	0.7
P_{ref} [Pa]	26436
T_{ref} [K]	223.15
U_{ref} [m/s]	209.62
ρ_{ref} [Kg/m^3]	0.412
$Re_{SOAR}\cdot10^{-6}$ (L_{ref}=17 m)	100.155

Table XIII. Reference condition for the wind tunnel model.

Mach	0.7
P_{ref} [Pa]	19223
T_{ref} [K]	273.22
U_{ref} [m/s]	231.95
ρ_{ref} [Kg/m^3]	0.245
$Re_{SOAR}\cdot10^{-6}$ (L_{ref}=0.0944 m)	0.3092

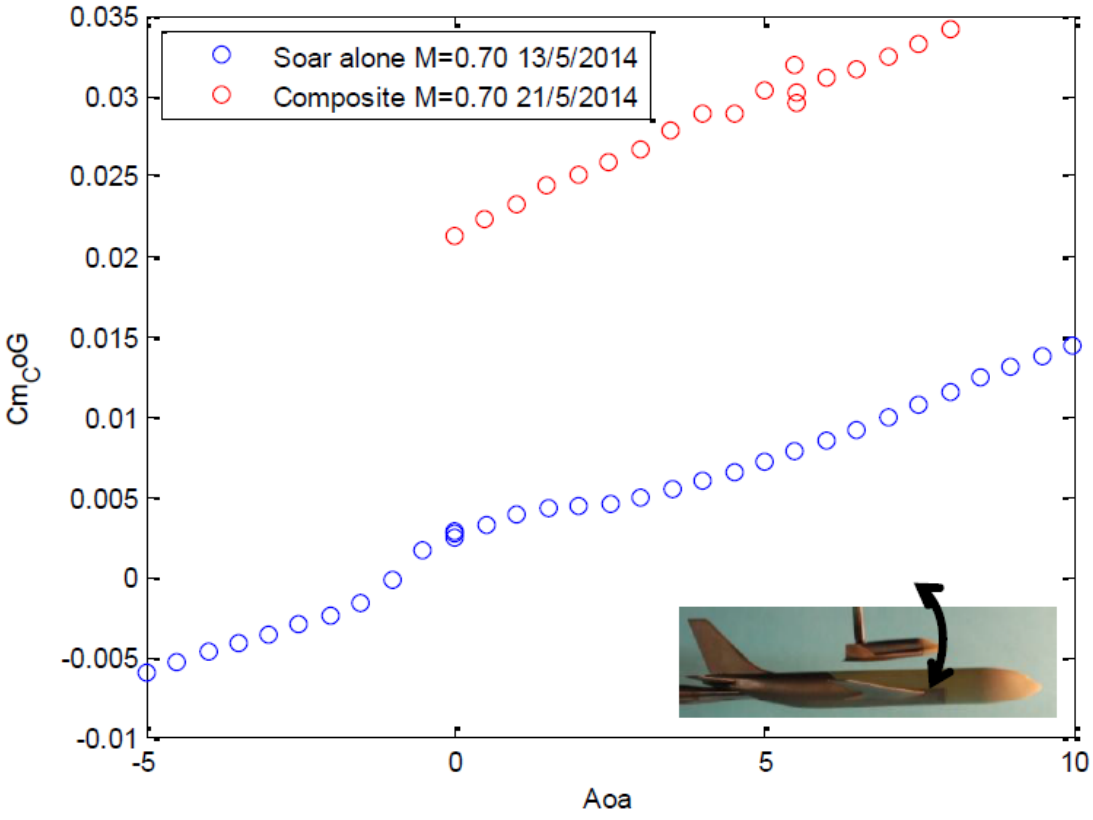

Figure 59. Pattern of the SOAR pitching moment slope. In red the values when also the presence of the Airbus.

The results of the solution for the equation (6) are reported in the next table:

Table XIV. Results of the equation (6) and respective values of the derivative of the pitching moment coefficient. Due to the not constancy, the maximum, minimum and the value of the constant segment are reported (See Figure 59).

Scale	1:180			1:80		
$\dot{C}_m$	$\dot{C}_{m_{max}}$	$\dot{C}_{m_{min}}$	$\dot{C}_{m_{cost}}$	$\dot{C}_{m_{max}}$	$\dot{C}_{m_{min}}$	$\dot{C}_{m_{cost}}$
	$3.122 \cdot 10^{-3}$	$1.341 \cdot 10^{-3}$	$2.101 \cdot 10^{-3}$	$3.122 \cdot 10^{-3}$	$1.341 \cdot 10^{-3}$	$2.101 \cdot 10^{-3}$
ν_e[Hz]	26.809	17.564	21.991	11.961	7.801	9.675

Finally the oscillation frequency due to the vortex shedding is computed using the Strouhal number of a cylinder:

$$S_t = 0.2$$

(7)

From what it is possible to reverse the formula (4) and obtain:

$$\nu = \frac{S_t U_\infty}{D}$$

(8)

It is calculated the vortex shedding frequency of the main body and of the tail plane, using the following dimensions as characteristic length:

Table XV. Reference length. D1 is the diameter of the body, D2 is the maximum chord of the tail plains.

Reference length	1:180	1:80
D1 [m]	0.013	0.031
D2 [m]	0.022	0.051

The vortex shedding frequencies are:

Table XVI. Vortex shedding frequency for both the wind tunnel SOAR models.

Scale	1:180		1:80	
Reference length	D = D1	D = D2	D = D1	D = D2
ν_{Sh} [Hz]	3480	2078	1487	927.8

4.4.1 Results of the frequency analysis

First there are the pictures of the shape of the first vibration mode for each case, then the firsts four natural frequencies are reported.

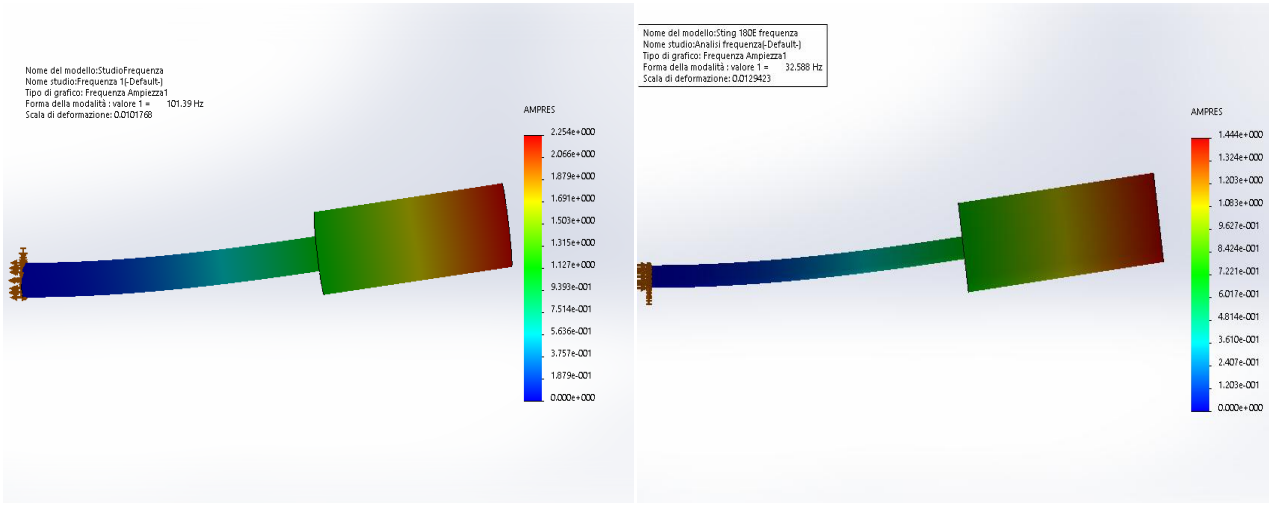

Figure 60. First mode of vibration, circular sting on the left and elliptic on the right; scale 1:80.

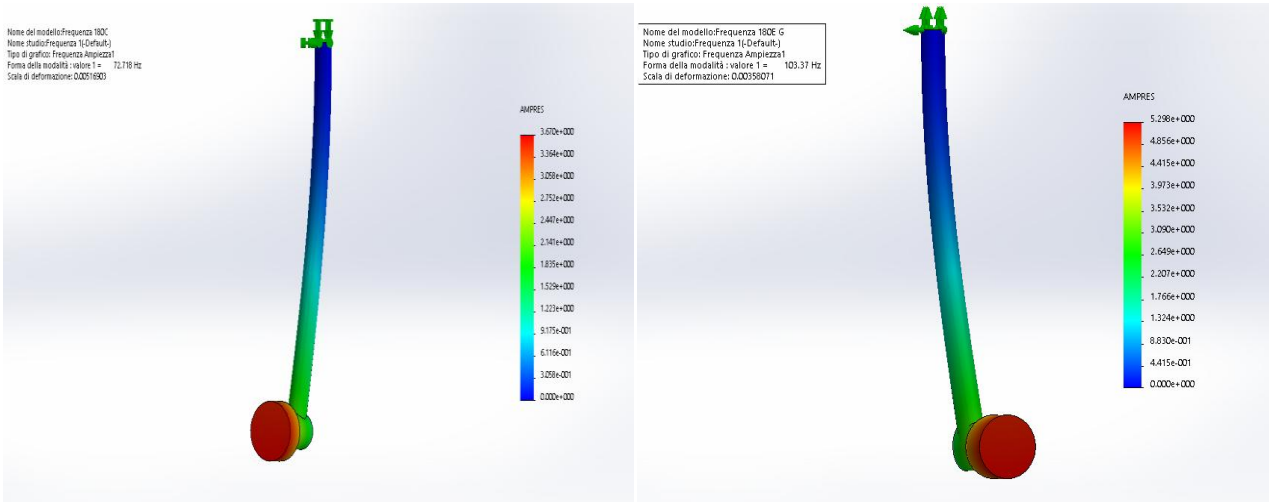

Figure 61. First mode of vibration, inclined support with circular sting on the right and with elliptic one on the left; scale 1:180.

Table XVII. Natural frequency of the first four vibration modes, circular sting, scale 1:80.

Scale 1:80 circular sting			
Mode of vibration	**Frequency(Rad/s)**	**Frequency(Hz)**	**Period(s)**
1	637.03	101.39	0.0098633
2	637.44	101.45	0.0098568
3	5687.9	905.26	0.0011047
4	7277.2	1158.2	0.0008634

Table XVIII. Natural frequency of the first four vibration modes, elliptical sting. scale 1:80.

Scale 1:80 elliptical sting			
Mode of vibration	**Frequency(Rad/s)**	**Frequency(Hz)**	**Period(s)**
1	204.76	32.588	0.030686
2	326.16	51.91	0.019264
3	2161.9	344.07	0.002906
4	2602.3	414.18	0.002414

Table XIX. Natural frequency of the firsts first four vibration modes, inclined support with circular sting. scale 1:180.

Scale 1:180 inclined support with circular sting			
Mode of vibration	**Frequency(Rad/s)**	**Frequency(Hz)**	**Period(s)**
1	456.9	72.718	0.013752
2	1080.8	172.01	0.0058135
3	3108.2	494.68	0.0020215
4	4916.9	782.54	0.0012779

Table XX. Natural frequency of the firsts first four vibration modes, inclined support with elliptical sting. scale 1:180.

Scale 1:180 inclined support with elliptic sting			
Mode of vibration	**Frequency(Rad/s)**	**Frequency(Hz)**	**Period(s)**
1	649.5	103.37	0.009674
2	1580	251.46	0.003976
3	3218.6	512.25	0.001952
4	6934.1	1103.6	0.000906

Table XXI. Summary of the external frequencies.

	1:80	**1:180**
ν_{eMax}**[Hz]**	11.96	26.81
ν_{ShD1} **[Hz]**	1487	3480
ν_{ShD2} **[Hz]**	927.8	2078

4.5 Conclusions of the structural analysis

The conclusions of the preliminary structural analysis are in the following order:

- considerations about the results of the static analysis with the main loads acting;
- considerations about the results of the static analysis with the lateral force;
- considerations about the results of the frequency analysis.

4.5.1 Results of the static analysis with the main loads

In general the external loads taken with an adequate safety margin do not involve problematic stresses and strains. The followings critical points are reported:

- **Bending angle.** The value of this angle cannot be ignored in any case, especially in scale 1:80, but also both the bending angles of the scale 1:180 support. It is useful to remind that they are approximate (See paragraphs 4.2.1.3 and 4.2.2.3) and an accurate evaluation will be indispensable before the experiment. See Table XXII for the summary of all results.
- **Maximum stress for the elliptic sting in scale 1:80.** It is about the double of what is for the circular sting in the same scale and one third the yielding value. Then a margin is present yet but now it is lower. This huge difference is due to the smaller thickness of the elliptic sting walls and it entail also a smaller worsening on the displacement.

In addition to this it is important to highlight the next facts:

- **Stress concentrations at the junction between the stings and the inclined bars (scale 1:180)** With both sting shapes a stress concentration is present at the frontal top junction between the two parts. The different insertion (see paragraph 3.3) probably increases the maximum stress with the circular sting.
- **Stress concentrations at the top fixed constraints (scale 1:180).** Others stress peak (half of the maximum stress) are always at the fixed superior constraint where the supports will be attached to the mechanism.
- **Differences between the two sting shapes (scale 1:180).** Also in scale 1:180 the elliptic sting would suffer greater stress but in this case it was possible to perform a better connection with the inclined bar (again see paragraph 3.3). The smaller insertion of the inclined part in the circular sting seems to increase the maximum stress. It is difficult to quantify the amount of this.

4.5.2 Results of the static analysis with the lateral force

The lateral force does not involve any new criticality even if all stresses values are slightly increased. The following points are highlighted again:

- **Increasing of the maximum stress.** With the lateral force there is a variation of the stress distribution with also a bigger peak value. These variations do not entail a critic point because the maximum value remains lower than the yielding strength.
- **Bending angle.** Also the lateral force involves a bending angle that it is necessary to take into account. It is useful to remind that this angle is not the total bending angle but it is only a contribution at the deformation. In the inclined supports this is the highest term.

4.5.3 Results of the frequency analysis

The natural frequencies of vibration of the stings are lower than the vortex shedding frequencies, with an adequate margin in every case. The fact that the vortex shedding frequency of the tail plain might be close to the third natural frequency of the scale 1:80 circular sting is not considered as a possible problem. It is preferable does not use both scale 1:80 stings for the forced oscillation testing. In fact their resonance frequencies are quite close to the external vibration frequency of the SOAR model, also remembering the approximation done in paragraph 4.4.

In the following table all results are summarized.

Table XXII. Summary of the preliminary structural analysis results and frequency analysis.

Scale	Principal forces			Lateral forces			Frequencies				
	σ_{max}[MPa]	ε_{max}	θ [°]	σ_{max}[MPa]	ε_{max}	θ [°]	ν_n [Hz]	ν_{ShD1} [Hz]	ν_{ShD2} [Hz]	ν_{eMax} [Hz]	σ_y[Mpa]
1:80 C	123.9	5.1·10-4	0.46	165.4	$6.6 \cdot 10^{-4}$	0.12	101.3	1487	927.8	11.96	620.4
1:80 E	202.4	7.5·10-4	0.67	214.0	$8.2 \cdot 10^{-4}$	0.46	32.59	1487	927.8	11.96	620.4
1:180 C	57.1	1.7·10-4	0.12	91.77	$2.7 \cdot 10^{-4}$	0.27	72.72	3480	2078	26.81	620.4
1:180 E	56.4	1.6·10-4	0.13	96.97	$2.9 \cdot 10^{-4}$	0.30	103.3	3480	2078	26.81	620.4

4.6 Recommendations after the structural analysis

For the further developments the attention will be focused on:

- Research a steel alloy with an high yield strength to have a larger margin especially for the elliptic sting (scale 1:80).
- It is suggested also a slight increase of the wall thickness of the elliptic sting (scale 1:80) in particular if it is not possible to use a material with higher performance.
- An exact calculation of all displacements and strains with the application of strain gages at the supports, especially for the bending angle.

To reduce the high region of stress present on the circular sting of the inclined support it is suggested to increase the insertion of the support in the sting, if possible.

It is necessary to perform some modifications to use scale 1:80 stings for forced oscillation test, otherwise its utilization is not precluded in static tests.

In general the use of elliptic stings, from a structural point of view is possible, even if the stress distributions are more problematic.

5 Computational Fluid Dynamics analysis

In this chapter the steps taken in order to perform the computational campaign are listed. In the introduction the strategy, the simulations and other general information are explained, followed by the meshing, the computational procedure and the post processing.

5.1 Introduction

The Computational Fluid Dynamics (CFD) simulations represent one of the most important contributions in this project. In fact the flow field and the force interferences due to the support were studied by comparing simulations with and without support. To study the alteration of the flow during the wind tunnel test due to the presence of the artificial strut is fundamental for two reasons:

- To help design it as discrete as possible
- To understand the right correction to the wind tunnel results.

In particular the impact of different shape of stings (circular and elliptic), dimensions, presence of an inclined part (with different inclination) and the effect of an angle of attack were studied. To do this for each scale the SOAR alone was tested at 0, 5, 10 and 15 degree of angle of attack, as reference. Then every shape of support (circular or elliptic) was tested, with the nominal dimensions, connected to the vehicle, at the same angles of attack. After this, the variation of the dimensions were evaluated at 0 degree of angle of attack, with the sting longer or shorter by 10 percent. Also simulations with the diameter bigger than the 10 percent were performed but not with a smaller one that is not possible the cables are to be brunched inside the sting[21]. A change in the dimensions (10% length and diameter increase) is applied also with the presence of an angle on attack to understand how these two different aspects can interact. The effect of the inclined part (scale 1:180) was studied by simulations with the nominal inclination of the vertical part respect to the straight sting (40,8°) and adding respectively 5, 10 and 15 degree of inclination. All simulations done are summarized in the following table.

[21] For the elliptic sting and increase in the diameter means a growth of the 10% for both axis.

Table XXIII. Simulations plan. with the V the simulations performed.

Scale	Kind of simulation	Characteristics of the sting		Angle of attack [°]			
				0	5	10	15
	SOAR alone			**V**	**V**	**V**	**V**
1:180	SOAR with Circular support	Nominal dimensions		**V**	**V**	**V**	**V**
		Length	+10%	**V**			**V**
			-10%	**V**			
		Diameter	+10%	**V**			**V**
		Inclination	+ 5	**V**			
			+ 10	**V**			
			+ 15	**V**			
	SOAR with elliptic support	Nominal dimensions		**V**	**V**	**V**	**V**
		Length	+10%	**V**			**V**
			-10%	**V**			
		Diameter	+10%	**V**			**V**
		Inclination	+ 5	**V**			
			+ 10	**V**			
			+ 15	**V**			
1:80	SOAR alone			**V**	**V**	**V**	**V**
	SOAR with circular sting	Nominal dimensions		**V**	**V**	**V**	**V**
		Length	+10%	**V**			**V**
			-10%	**V**			
		Diameter	+10%	**V**			**V**
	SOAR with elliptic sting	Nominal dimensions		**V**	**V**	**V**	**V**
		Length	+10%	**V**			**V**
			-10%	**V**			
		Diameter	+10%	**V**			**V**

This study is organized with a CFD mesh-solve-process structured in the following points:

- cleanup of the CAD file;
- meshing;
- computation;
- post processing.

The cleaning of the geometry and the mesh were done using Ansys ICEM CFD version 15.0 and Gambit version 2.4.6 for the mesh conversion, whereas the selected CFD tool was Metacomp CFD++ version 14.1. The post-processing was performed with Tecplot, Matlab, Microsoft Excel and avail script of VKI.

The computations were carried out on the Arlin6 machine[22] of VKI at the beginning to adjust the numerical setup. Once achieved and optimized the right set for the convergence the simulations were performed on the ClusterVision cluster[23] of VKI.

5.2 Geometry cleanup

When a CAD geometry is imported into a mesh generator software many inconsistencies can appear. This is due to different tolerance between the two software and the imported geometry could not be meshed adequately[24]. Then a work on the geometry becomes necessary and it was developed by three different points:

- simplifying the SOAR geometry file;
- simplifying all support files;
- connecting the support with the SOAR.

Work on the SOAR file was performed in order to have a lighter file easier manageable on different machines. For this reason the shape was not modified over a tolerance of 1^{-2}mm but only the parameterization of some surfaces were simplified. This operation reduced the file size from 312 MB to 17.8 MB. At the same time a real cleanup of the geometry was done, correcting all errors introduced at import from the CAD file.

On the support (in addition to the same cleanup procedure of the CAD file) also the shape was modified to achieve a better mesh on the surfaces. In the CFD model the holes for the cables were removed[25] and the geometry simplified. The only modification that can have an impact on the flow regard the scale 1:180 where on the rear part of the sting was necessary to modify the junction with the inclined part. Unfortunately it was not possible to do the same simplification with the elliptic and the circular sting. In the following picture it is possible to note the differences of the individual shapes. This choice will cause a different pressure contour on the rear parts of the supports. (See paragraph 5.7.1.1)

[22] Arlin6 performance: dual 10 core Intel Xeon E5-2670, 2.5GHz with 4TB raid storage and 128GB RAM.
[23] ClusterVision performance: It consists of identical blades, each equipped with 4 AMD Opteron 6376 processors and 256GB RAM. Only one blade was used for each computation.
[24] For more information about the geometry clean up see [11].
[25] It is useful to remind that in the complete support the holes for cables are closed by the cables themselves or by a flat surface.

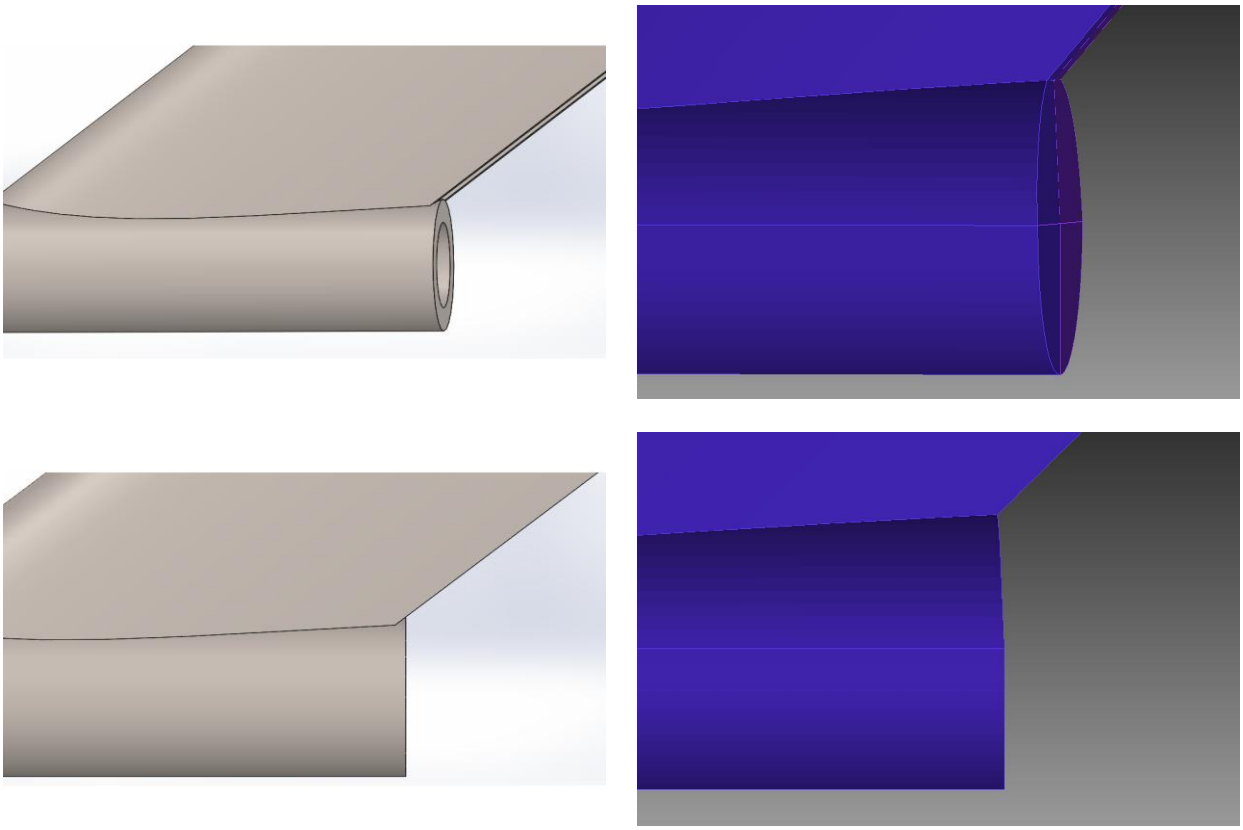

Figure 62. View of the shape variations between the CAD (right) and the CFD (left); support with circular sting.

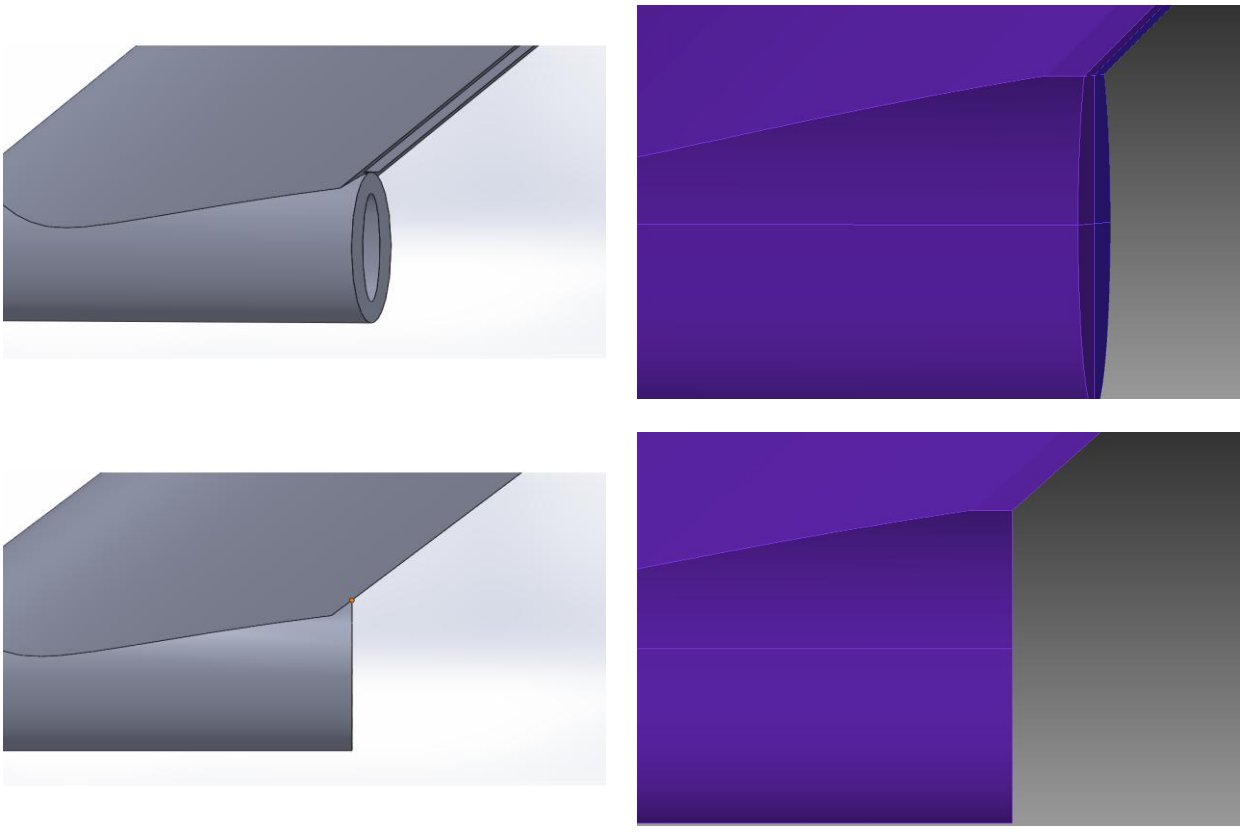

Figure 63. View of the shape variations between the CAD (right) and the CFD (left); support with elliptic sting.

5.3 Meshing

The unstructured surface mesh was performed using the autoblock method[26] present in the version 15.0 of ICEM CFD. The elements are all triangular and the body was divided into different parts in order to control the refinement (See Figure 65). Elongation surfaces were inserted near SOAR trailing edge to delay the boundary layer to tetra mesh transition away from the body (called leadouts, see Figure 64). This ensured compromising pressure jumps, it might appear far from to the trailing edge due to element transitions. See Figure 65 - Figure 68 for the achieved surface mesh. The surface mesh was build in the real scale model and the fluid domain reproduces the S1 wind tunnel test section (paragraph 1.3).

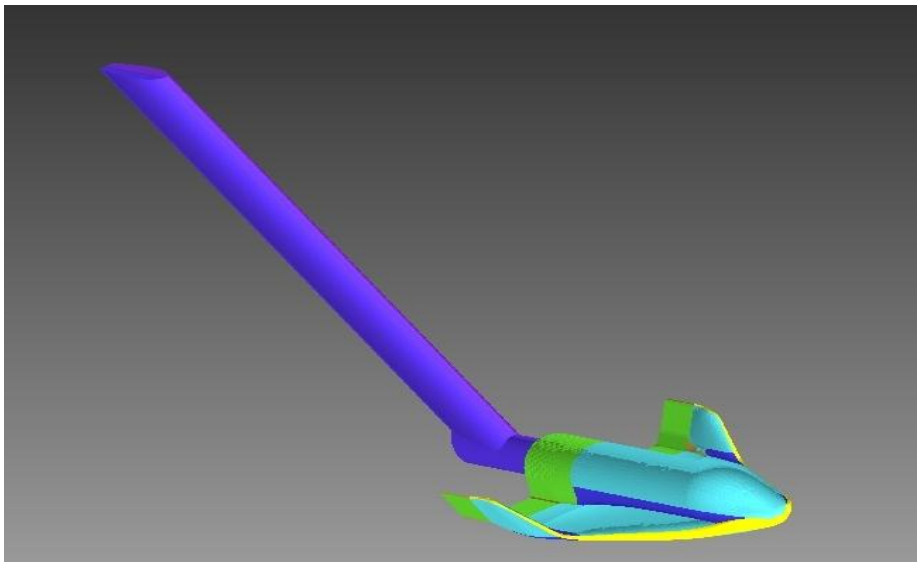

Figure 64. Solid view of the completed mesh of the SOAR with the support in the back. Elliptic, scale 1:180. In green and ochre the leadout.

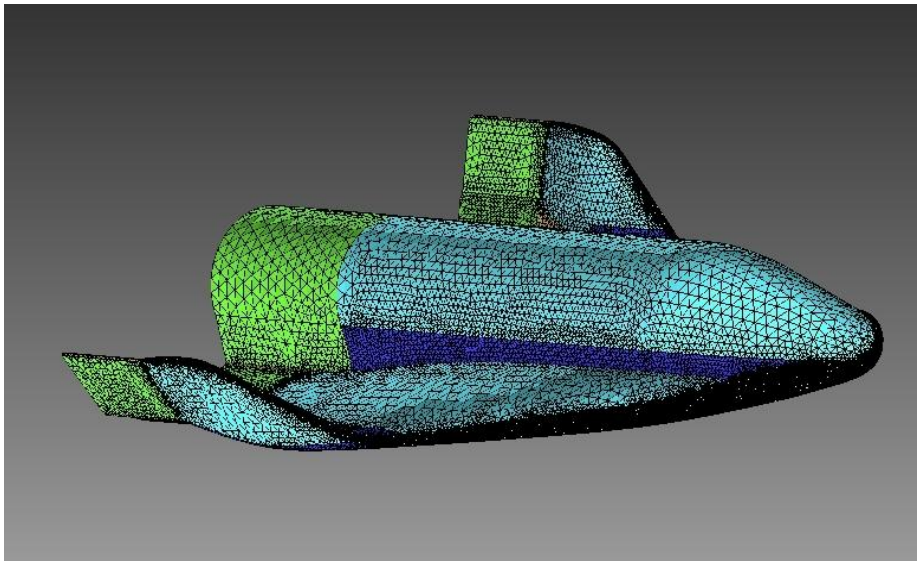

Figure 65. Solid and wire view of the SOAR mesh. It is possible to appreciate the different refinement of each parts.

[26] This method uses the mapped or block-based meshing algorithm. It automatically determines the best fit to obtain the defined minimum edge and orthogonality. For surface patches that cannot be mapped (having more or less than 4 corners), the Patch Dependent method is called through this block-based algorithm [8].

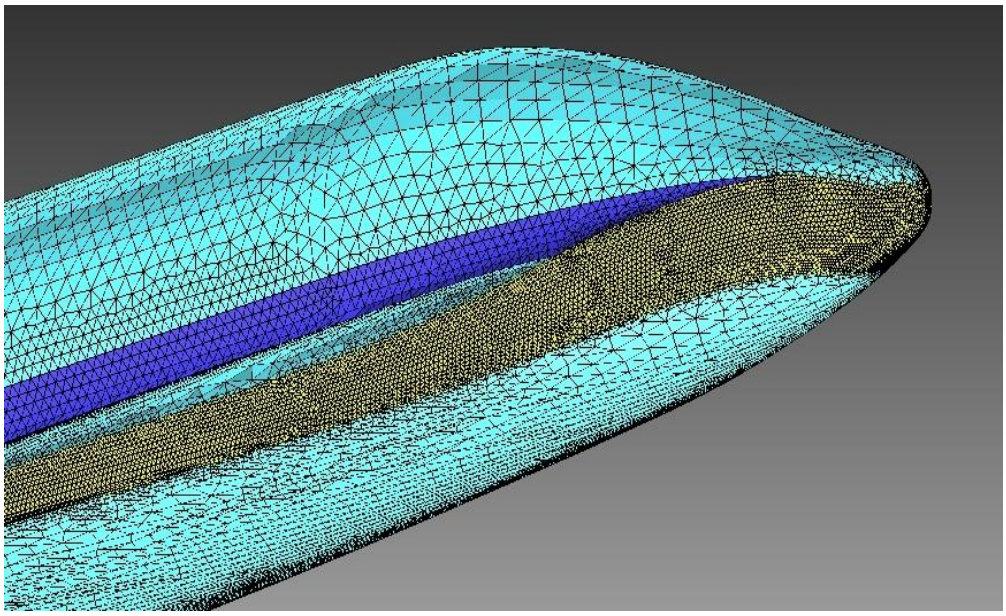

Figure 66. Solid and wire view of the SOAR nose mesh.

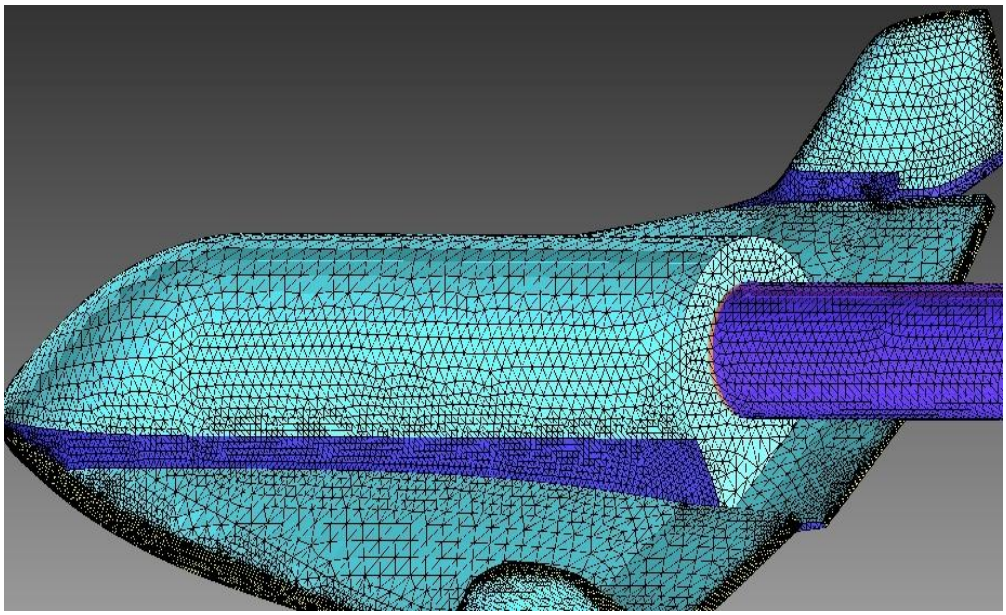

Figure 67. Solid and wire rear view of the SOAR with the junction for the support.

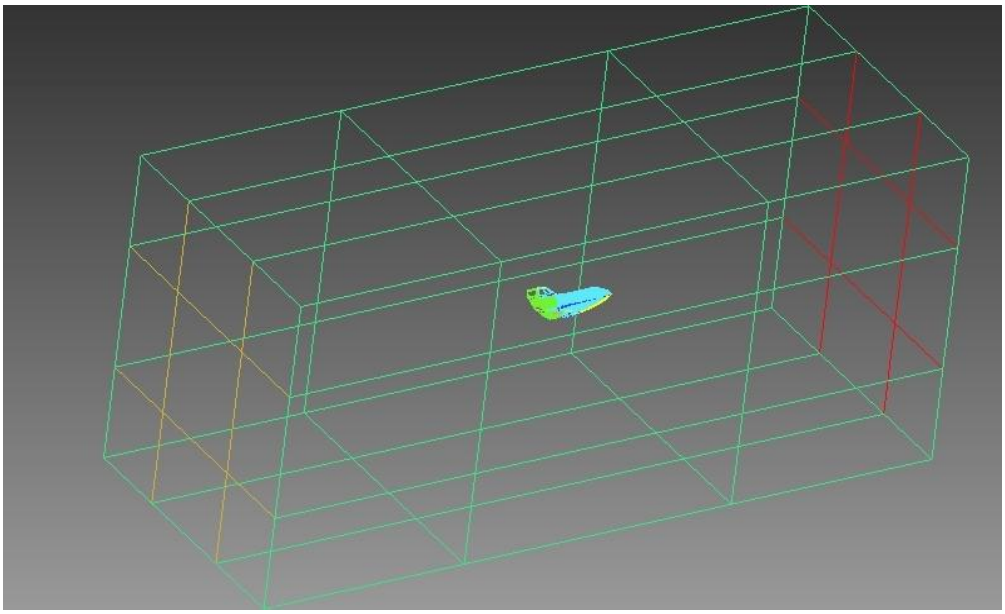

Figure 68. Wire frame view of the SOAR vehicle inside the fluid domain.

This surface mesh consists of about 86000 elements, for the SOAR alone, and about 110000 elements for the SOAR with the straight and inclined support.

From this surface mesh a volume mesh was build between the model and the fluid domain walls. The mesh type is Tetra-mixed with a Delauny method that used a Tglib scheme with the advancing front. After this an exponential "prism growing" extrusion method was applied, which is a kind of level-set technique to grow constant thickness layers around the body (with increasing thickness layer by layer). This prism layer forms the boundary layer thickness and it consists of 25 levels with an expansion ratio of 1.2 and first cell height of 0.5 mm. The total height of the boundary layer mesh is 235.99 mm [27]. During the growth a directional smoothing and a smoothing of the first layer were applied. Some pyramid elements were generated to connect the prism column end sides to the tetra mesh (see Figure 69-Figure 71).

Since the target Mach number was lowered to 0.7, it went below the critical Mach number (when pockets of supersonic flows and shockwaves appear), therefore shock-refinement became unnecessary for this study. However, very small pockets of supersonic flows were observed with Mach number less than 1.1.

At this point mesh quality checking process was performed to ensure quality is above to 10^{-6} and a minimal cell volume is not less than 10^{-20} [28]. Usually about 30-40 elements were corrected manually during this process. Then the mesh was converted into Tgrid ANSI format using Gambit. Always in Gambit the surfaces of the leadouts were cancelled leaving intact the volume mesh around them.

The total number of mesh elements is just over 1.4 million.

[27] Since tetra meshing is not efficient for capturing shear or boundary layer physics a prism mesh became necessary. In fact prism elements efficiently captures these effects near the surface while maintaining the ease and automation of tetra mesh. The spacing of the prism layers to capture the Y+ for Navier-Stokes mesh is the main constraint for the prism layer height [8].

[28] Always up than 10^{-3}

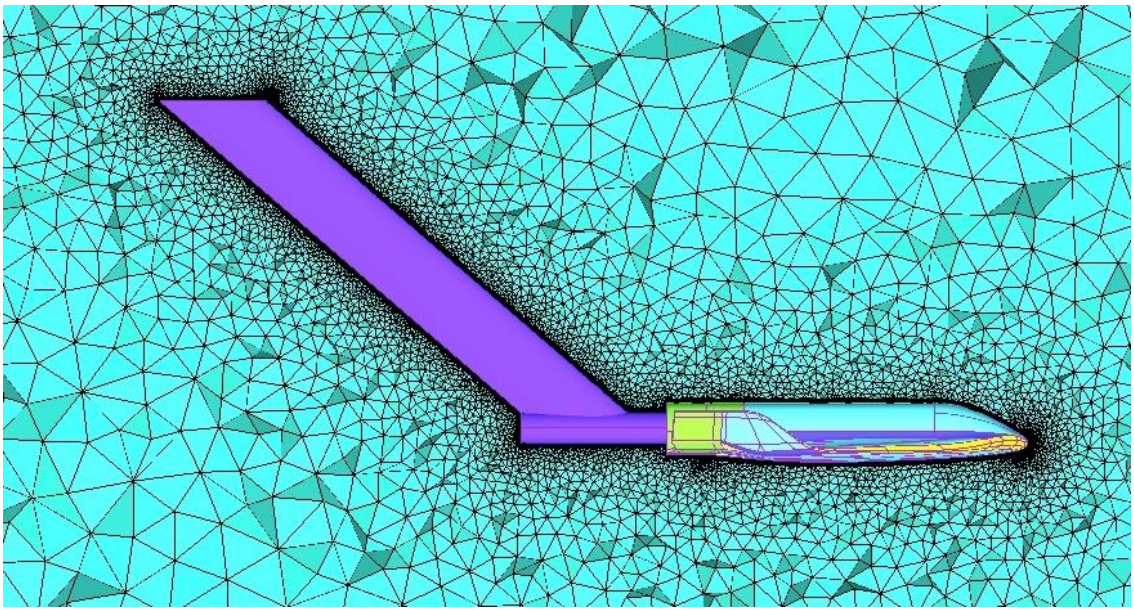

Figure 69. Solid and wire view of the completed volume mesh y middle plane.

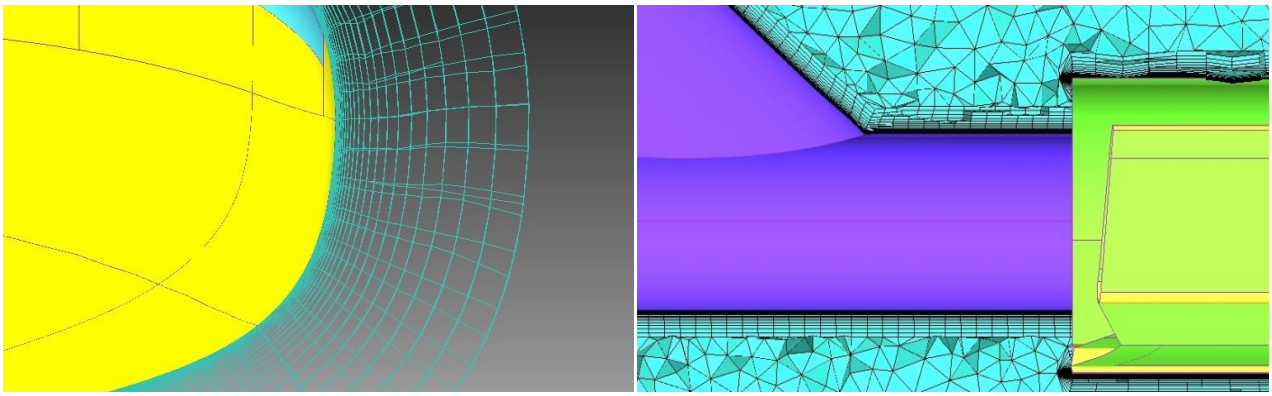

Figure 70. Zoom on the nose prism layer wire view, y middle plane, on the left. On the right zoom of the support-leading edge solid and wire view, y middle plane.

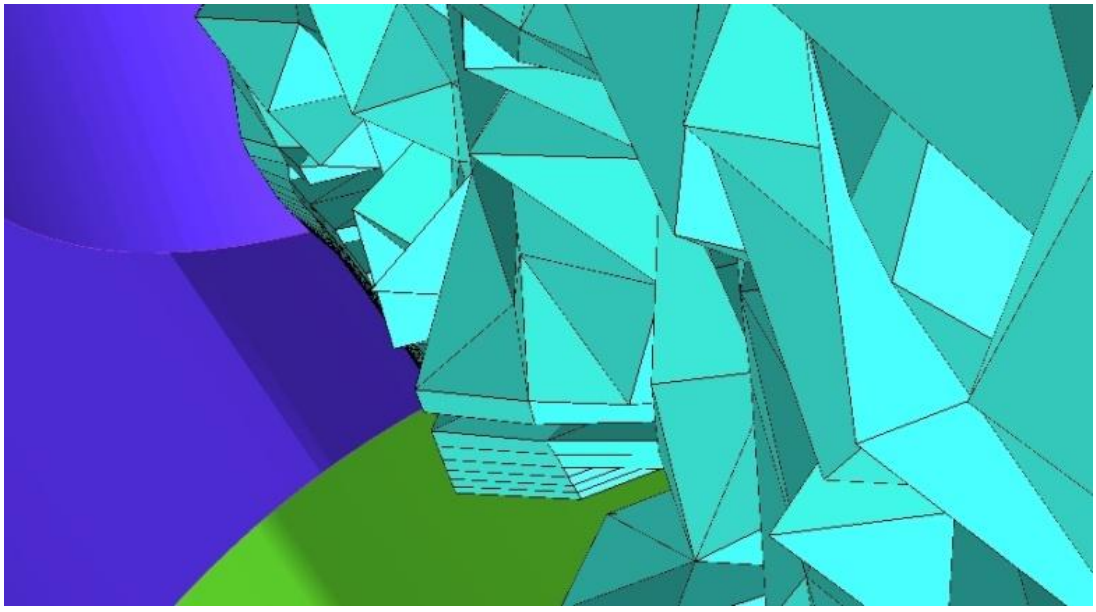

Figure 71. Zoom on the middle y plane over the leadout and the support. It is possible to see the connection between the prism and tetrahedral elements.

Once generated the first mesh the same settings were used to generate all meshes with different support geometry.

For the simulations with an angle of attack the mesh was rotated instead of changing the component of the velocity. To do this a box contained the surface mesh, the prism layer and the closer part of the tetra mesh was rotated while the rest of the free stream was re-meshed.

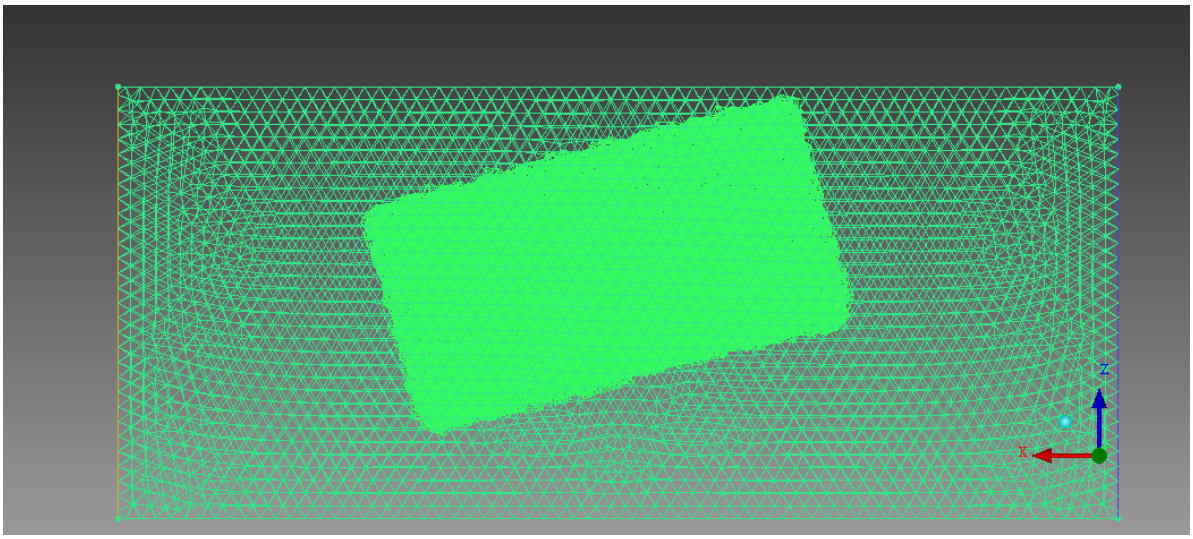

Figure 72. View of the rotated box inside the free-stream field.

5.4 Computation

In CFD++ the RANS simulations were performed with the k-ω SST model[29]. The following initial conditions were used:

Table XXIV. Initial conditions for the wind tunnel setup. Mach number, static pressure, static temperature, inlet velocity and density.

Mach	0.7
P_{ref} [Pa]	19223
T_{ref} [K]	273.22
U_{ref} [m/s]	231.95
ρ_{ref} [Kg/m^3]	0.245
K [m^2/s^2]	72.631
ω [s^{-1}]	$9.469 \cdot 10^{-3}$

About the boundary conditions:

- Navier-Stokes walls: no slip with wall function (including low-Reynolds corrections) defaulting to pure laminar no-slip friction in the laminar sublayer.
- Inlet/Outlet: combined velocity-temperature inlet and pressure outlet boundary. CFD++ automatically switches between inlet/outlet depending if the velocity vector is pointing in or outwards of the domain.

All computations were carried out in the same way: first an initial first order solution was obtained by slowly ramping CFL to 75 and when convergence was reached the solution was slowly blended to second order and let it converge again before starting the final, at least 1000 iterations for averaging[30]. The typical total number of iterations was 4600. The convergence was observed in terms of residuals, typically down to 10^{-6}(example of convergence shown in Figure 73) .

The body-support intersection is quite large and therefore its effect could not be neglected. The open part would behave as a zero pressure (vacuum) region if not corrected. Therefore the following correction was applied: around the holes of the SOAR, where the support attaches to the body, the average pressures was computed (on the red line shown in Figure 74). Based on this pressures and on the area of the hole, it is possible to introduce a compensating axial force[31].

29 The Reynolds-Averaged Naviers-Stokes equations (RANS) are time averaged equations of motion for fluid flow where the turbulence model compute the Reynolds stresses. The k-w SST model used is a two equations linear eddy viscosity model developed by Menter in 1993. See [12].

30 The aerodynamic coefficients present in this report derive from the averaging process.

31 The axial force then were decomposed in the drag and in the lift (for different from zero angle of attack) and then also in a contribution to the moment.

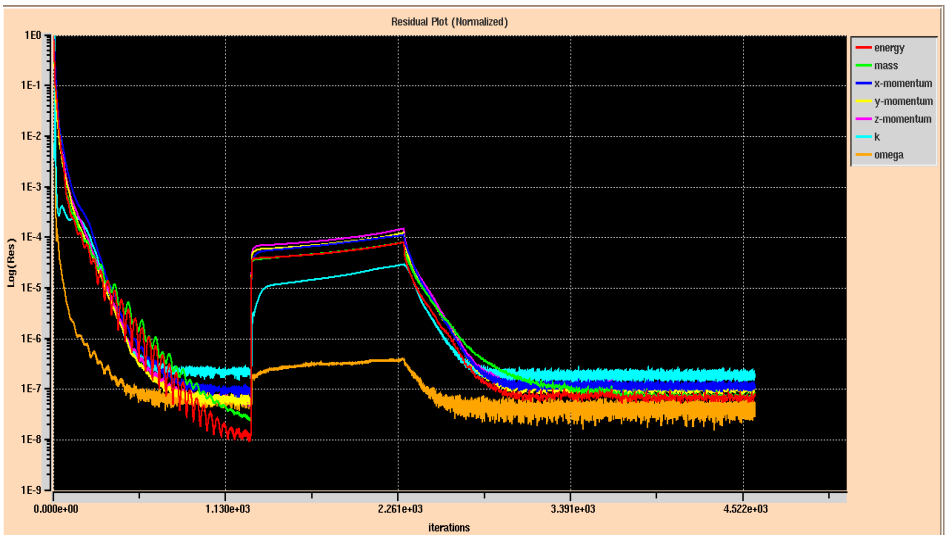

Figure 73. Typical residual plot.

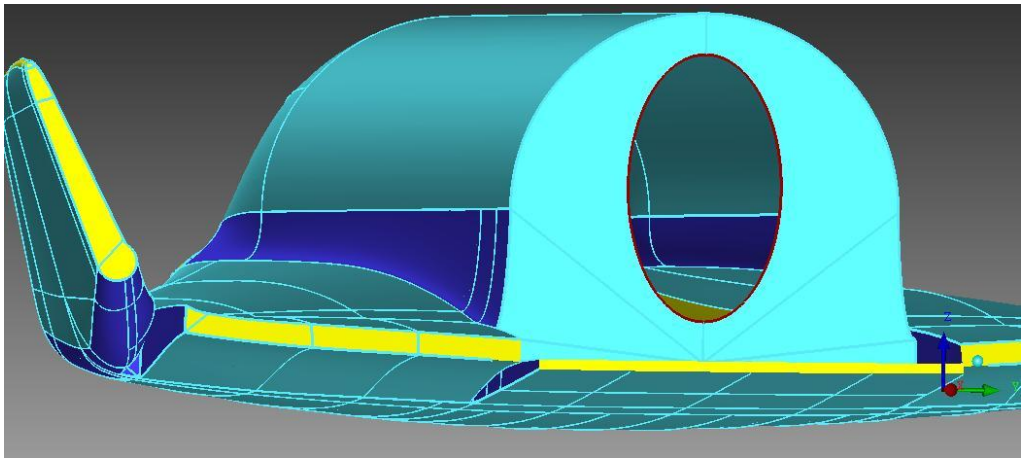

Figure 74. Rear view of the SOAR with the hole for the support. The support correction is based on average the pressure on the red line.

5.5 Mesh convergence study

A real mesh convergence study was not performed due to the availability of data from the previous SOAR CFD testing campaign with some simulations using the same conditions [1]. In that case a mesh refinement study was performed. Then it was possible to compare the results for the case of the SOAR alone in scale 1:180 with the wind tunnel conditions. In the following table the common cases are reported. It is clearly to see that the maximum error is just above 2% and this value can be assumed as the error of this computation. For the other angle of attacks the comparison was done interpolating the results of the old simulations obtaining a good agreement. They are not reported here because the confrontations is with not exact value.

Table XXV. Confrontation between the results of the old simulations with the result of the computations presented in this report. SOAR alone, scale 1:180.

	CD			CL			CM		
α	New results	Old result	Error %	New results	Old result	Error %	New results	Old result	Error %
0	0.0346	0.0340	1.8235	-0.0123	-0.0122	0.4667	0.0027	0.0027	0.2234
10	0.0771	0.0757	1.7981	0.3126	0.3060	2.1722	0.0138	0.0137	0.5150

5.6 Tabulated results

The results of the computational campaign, in a tabulated form, are given in the ANNEX B. While in the ANNEX A there are the plots of the aerodynamic coefficients.

5.7 Analysis of the results

In this section the results are evaluated. First the flow topologies are being looked at, followed by the evaluation of the generated aerodynamic database. All results of similar configurations are examined together and finally the attention is focused on the comparison between the different support shapes. First the scale 1:80 models are presented after the ones in scale 1:180.

5.7.1 Flow topology

In order to understand the flow, the main tool used in this section is the so-called Q-criterion. It is generally used to identify high curvature (vortices, waves, strong bends) structures in the velocity field. Also the skin friction lines are utilized to understand the flow over the surface, while the contour of the pressure and of the Mach number are used to understand the support impact on the SOAR.

5.7.1.1 Scale 1:180, SOAR alone and with support, α=0°

First looking at the SOAR alone, at 0° of angle of attack the main aspect that the flow presents are:

- Large induced vortices at the wingtips and behind the base;
- Partially detachment of the flow in particular under the flaps;
- The trace of the fuselage leaves a large turbulent wake behind the vehicle;

The presence of the support does not change the flow dramatically, neither the wake close to the vehicle. This is true for both elliptic and circular shapes. The most important appreciable difference is the larger detachment under the elliptic sting than with the circular one.

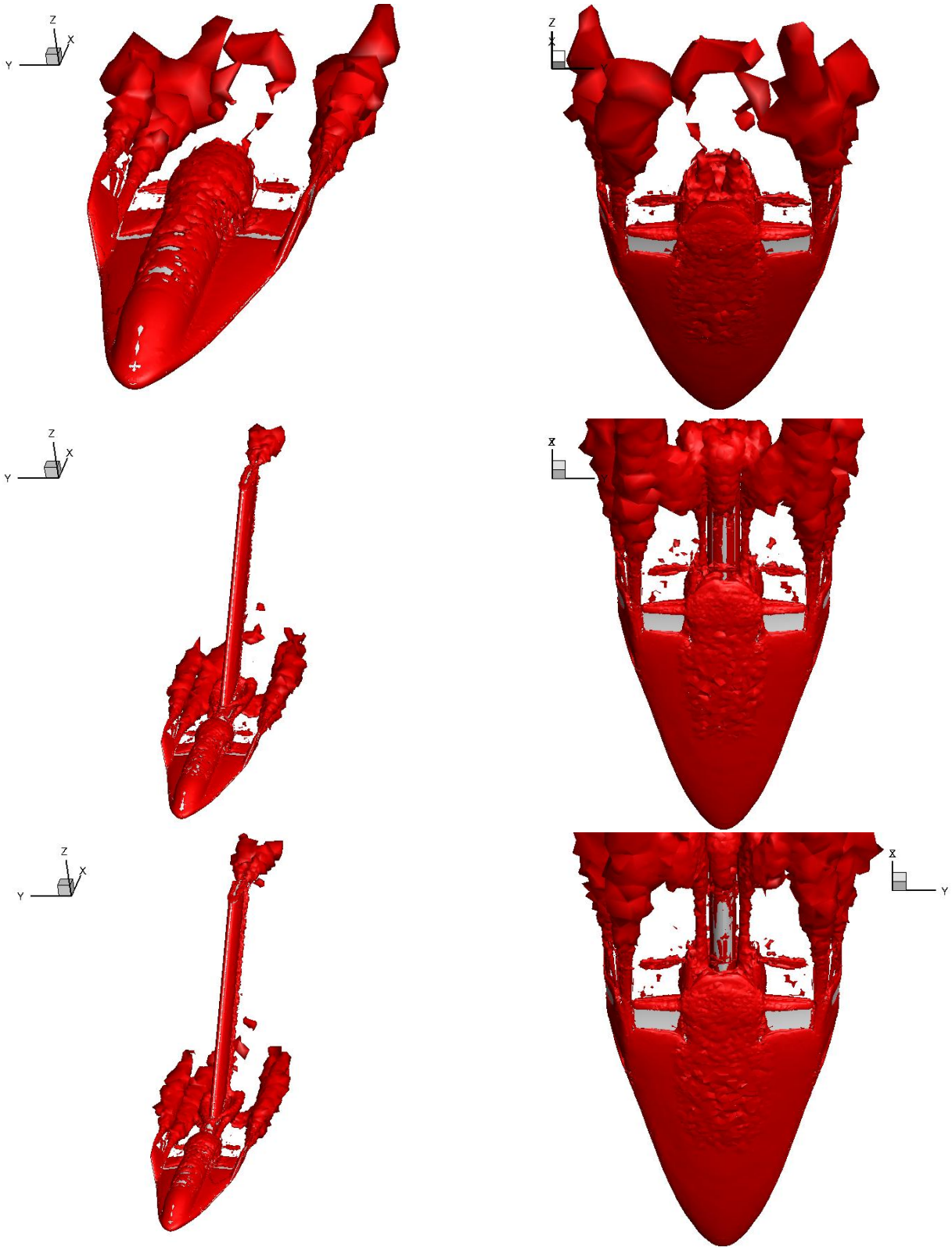

Figure 75. Q criterion=100000 ISO-surface of SOAR alone on the top, with circular sting in the middle and with elliptic on the bottom; scale 1:180, α =0.

From the skin friction lines it is possible to assess the recirculation of the flow and its path behind the vehicle and to the support (Figure 76).

The velocity component Z and Y are plotted to visualize the vortex distribution around the vehicle. It is possible to see how the circular sting induce large vortex on his top. Also the elliptic sting modify the flow pattern but with a lower impact (see Figure 77 and Figure 78).

Looking at the Mach number and at the pressure contour it is possible to observe a slowdown of the velocity and the increase of the pressure in proximity of the leading edge of the inclined support.

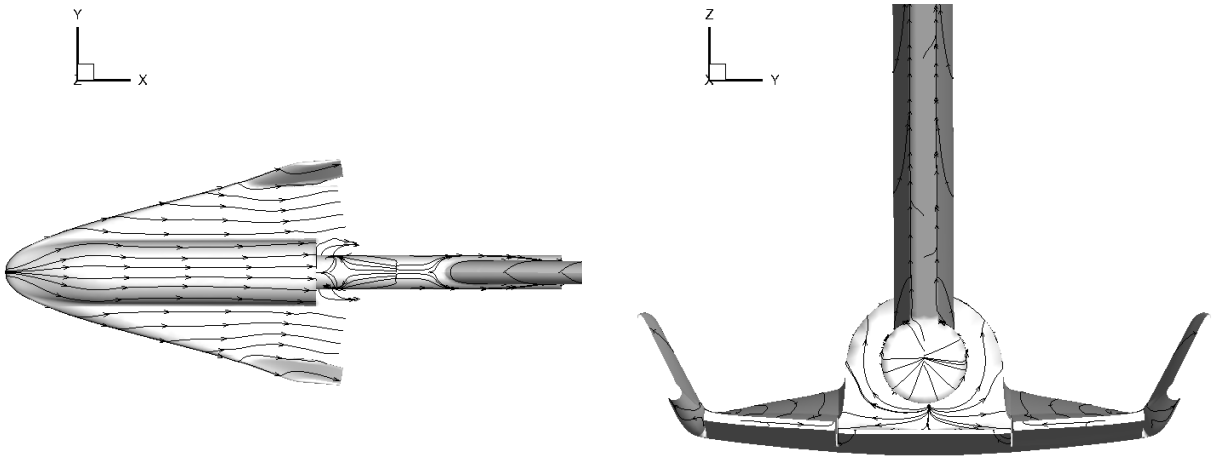

Figure 76. Skin friction lines of the SOAR with circular support scale 1:180, α =0. On the left top view, on the right back view.

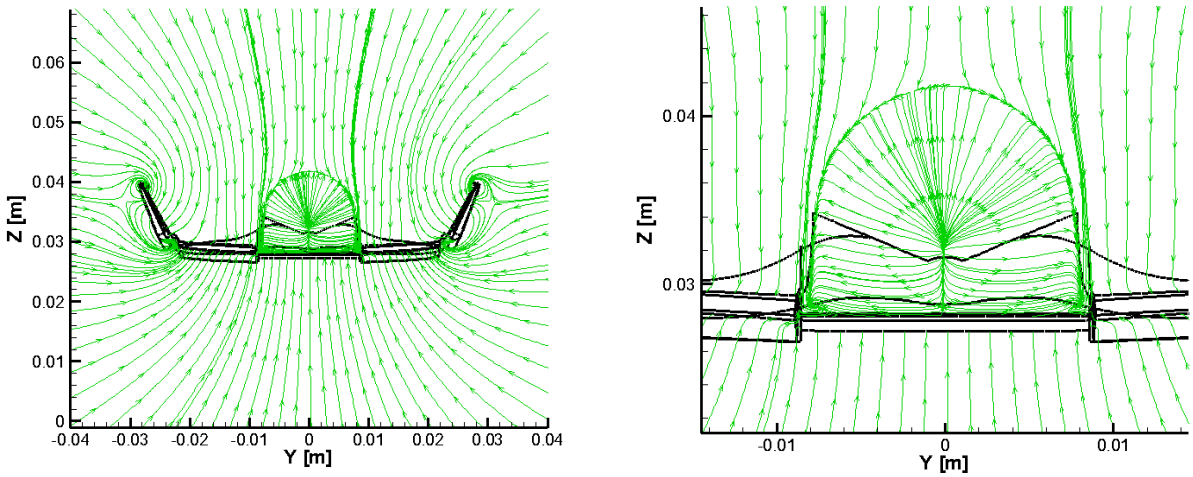

Figure 77. Plot of the y and z velocity component, SOAR alone; scale 1:180.

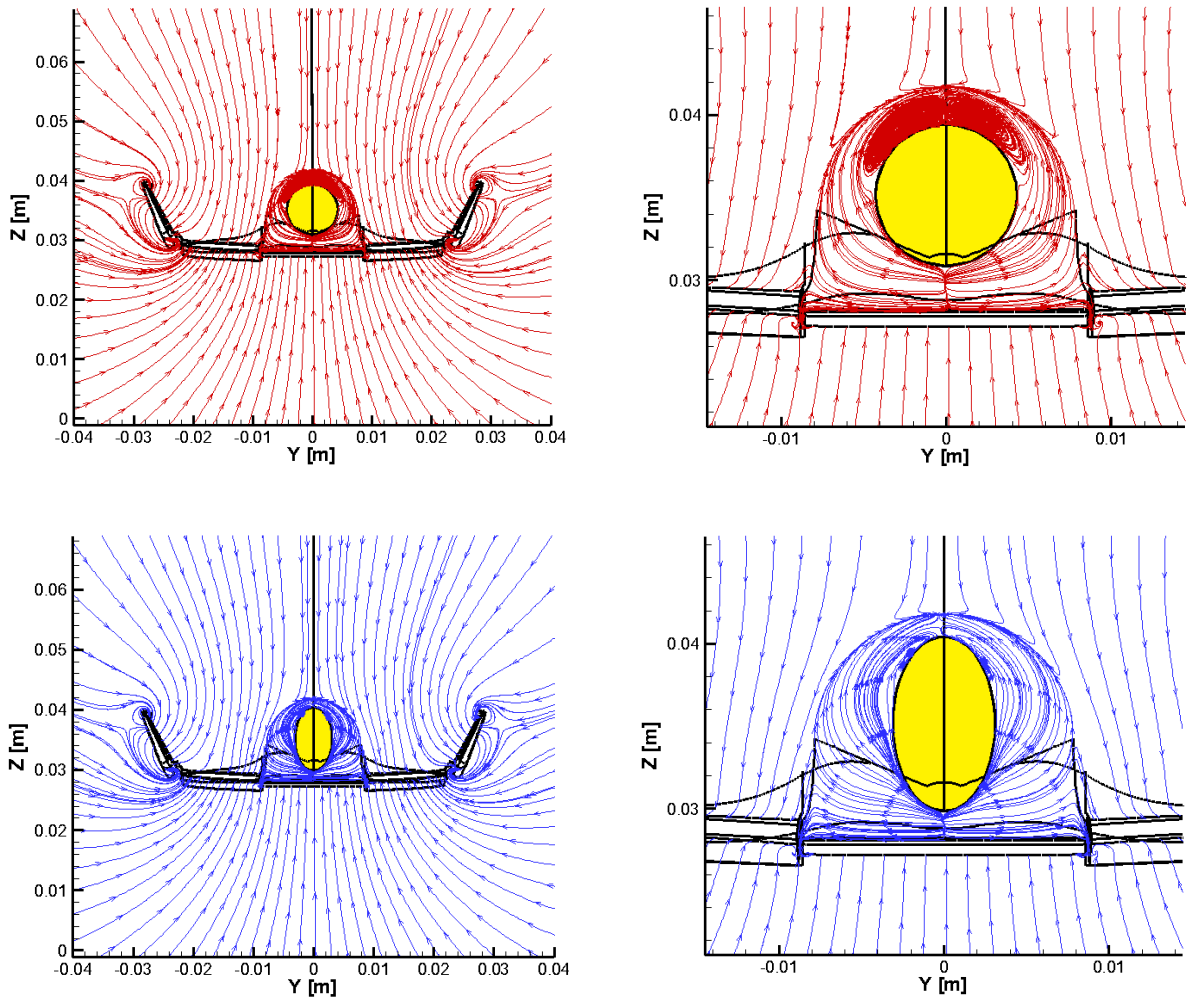

Figure 78. Plot of the y and z velocity component, SOAR with circular sting on the top, with elliptic sting on the bottom; scale 1:180.

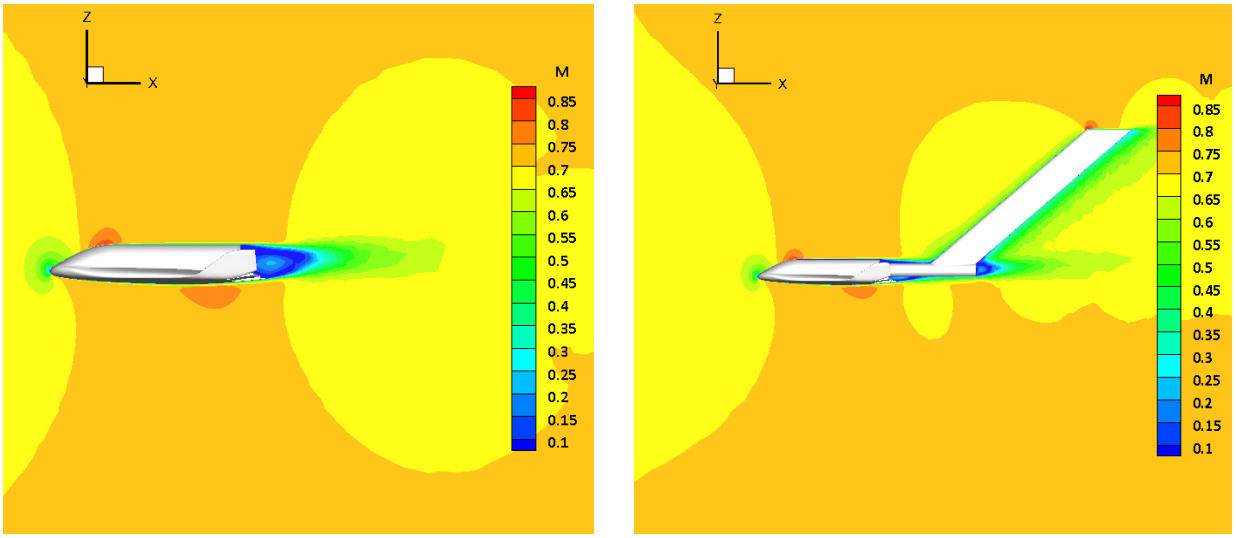

Figure 79. Mach number contour of the SOAR alone and with circular sting, scale 1:180, α =0°.

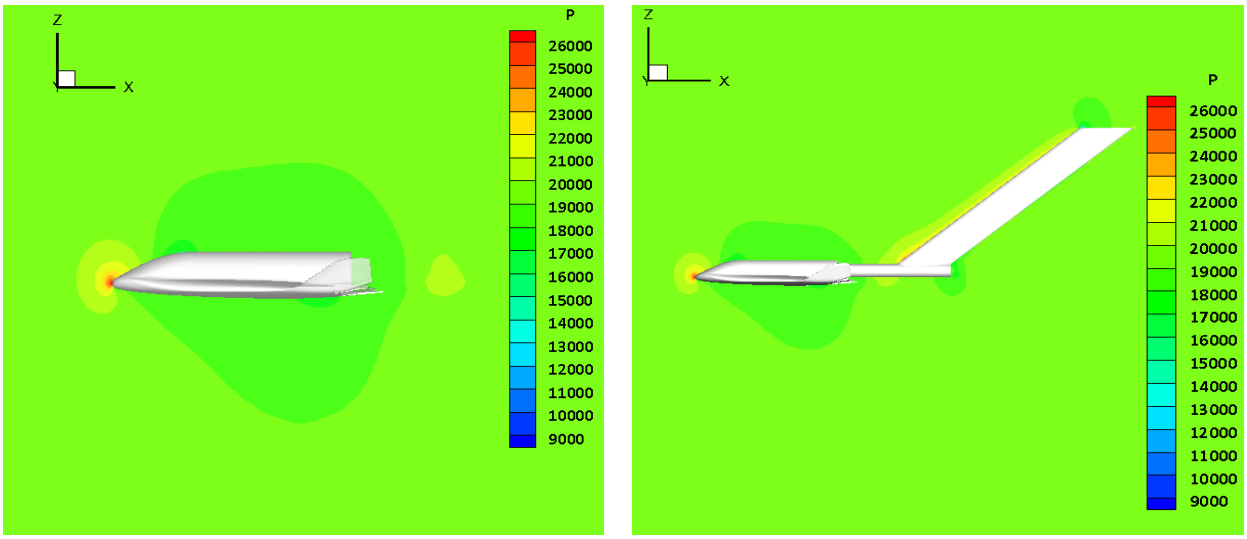

Figure 80. Pressure number contour of the SOAR alone and with circular sting, scale 1:180, α =0°.

The main effects of the support on the SOAR are the peaks of pressure on the base part, on the flaps and on the central body. These extra pressures are responsible of the decrease of the lift and of the growth of the moment. In fact the high pressure on the flaps is far away from the centre of gravity of the vehicle and its effect on the pitching moment is large.

Also the inferior surface of the vehicle reveal a higher pressure but the value are lower than what happens on the superior part and arranged more homogenously. Then the higher pressure on the bottom rather contrasts the decrease of the lift but less the increase of the pitching moment. See Figure 82, Figure 83 and paragraph 5.7.1.1.

It is possible to understand better the phenomenon just explained looking at the following picture where the increase of pressure due to the sting over the flaps is more evident.

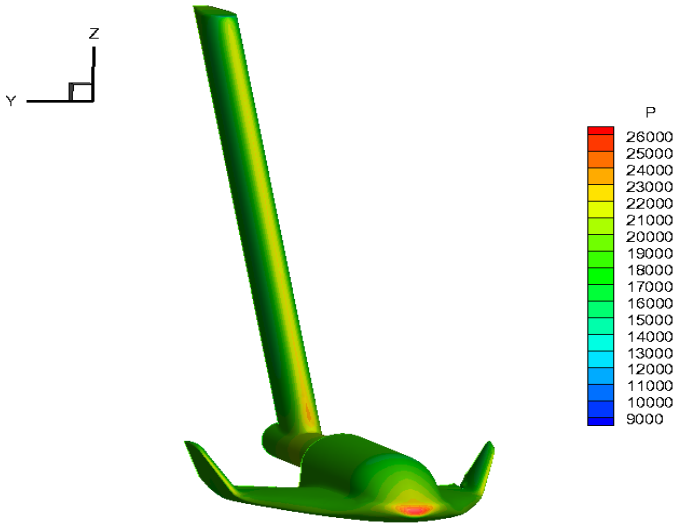

Figure 81. View of the pressure contour on the SOAR with circular sting

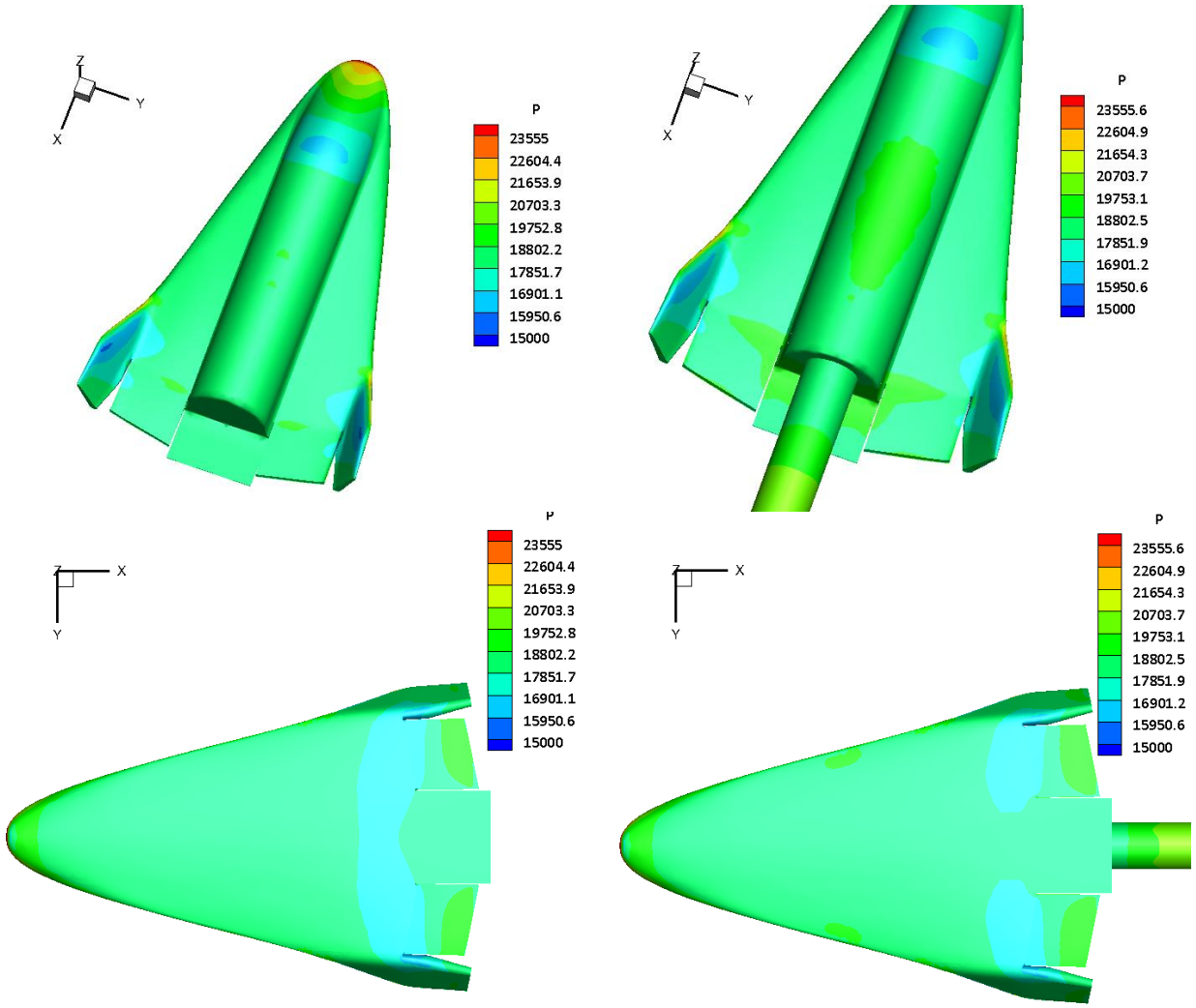

Figure 82. Top and bottom view of the pressure contour. SOAR alone on the left, SOAR with circular sting on the right.

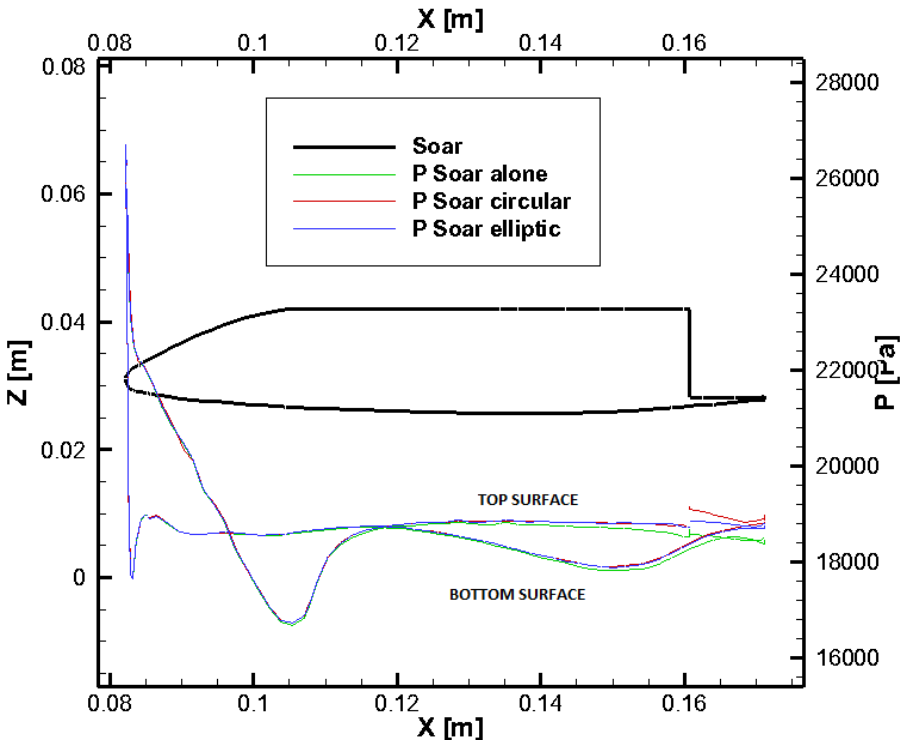

Figure 83. Pressure distribution on the SOAR middle y plane.

Afterwards looking from the back it is clearer the extra pressure induced by the sting in the rear surface of the SOAR. In fact the presence of the support blocks the flow in the wake, decrease the recirculation and increase the pressure that pushes forward the body, reducing the drag. Now focusing on the effect of different sting shape, the elliptic one with its more streamlined cross section causes fewer interferences allowing a better ease of the flow moving around. In particular this phenomena is present below the circular sting that with its larger section blocks more the flow.

Asymmetricities appear on the contour plots arising from the fact that the surface data is obtained from "instantaneous" intermediate save. Coefficients themselves were averaged at least 1000 iterations, as explained earlier.

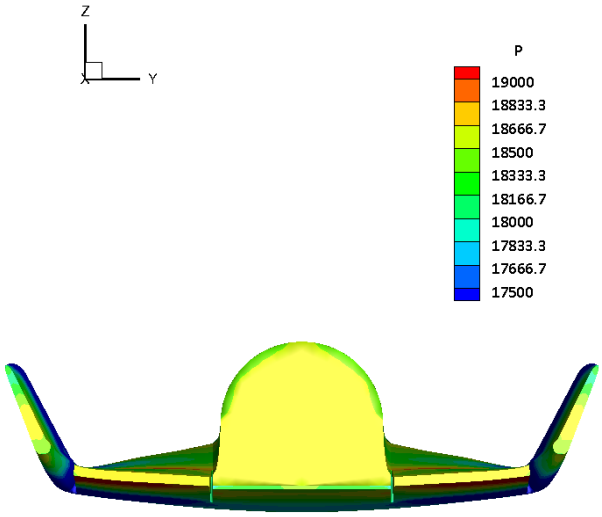

Figure 84. Back view of the SOAR alone; scale 1:180, α=0°.

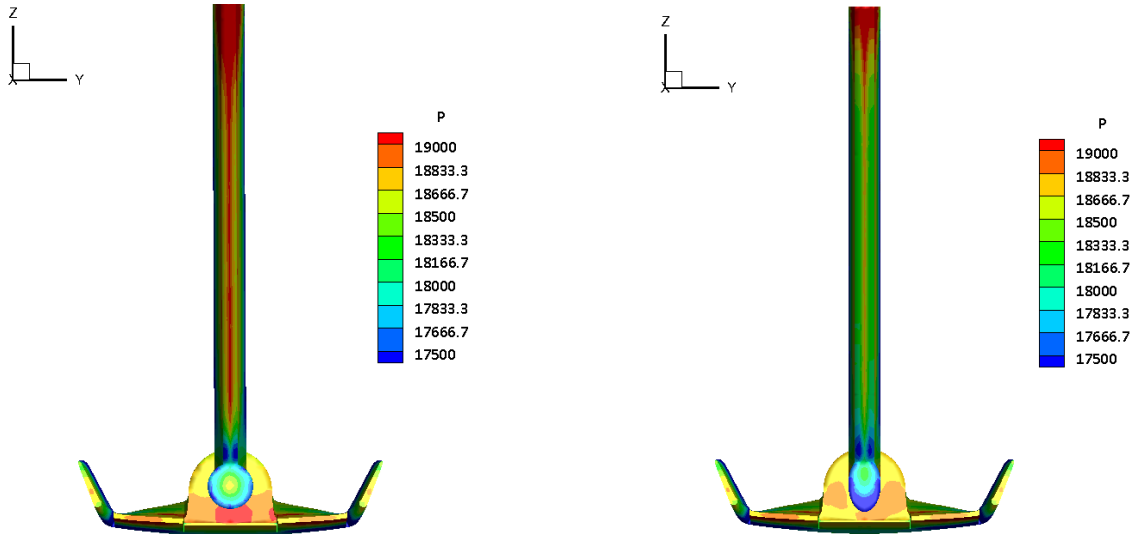

Figure 85. Back view of the SOAR with circular sting, on the left and with elliptic one, on the right; scale 1:180, α=0°.

Another aspect that is immediately evident from Figure 85 is the higher pressure on the trailing edge of the vertical part of the support with circular sting with respect than what happen on the elliptic one. This fact is mainly due to the different geometrical simplification made in paragraph 5.2 that also involves a different superior section (Figure 88). Such an important

effect was not expected when the rear part of the support was modified but it is in the same way a useful suggestion about how to fix the posterior part of the design. From Figure 87 it is possible to see that for the support with the circular sting there is a greater pressure behind it that is closer to the support wall than what happens for the support with elliptic sting. It is also possible to see that forward to the sting the pressure contour lines overlay on each other (see Figure 88) causing the same disturbance towards the SOAR after one chord length.

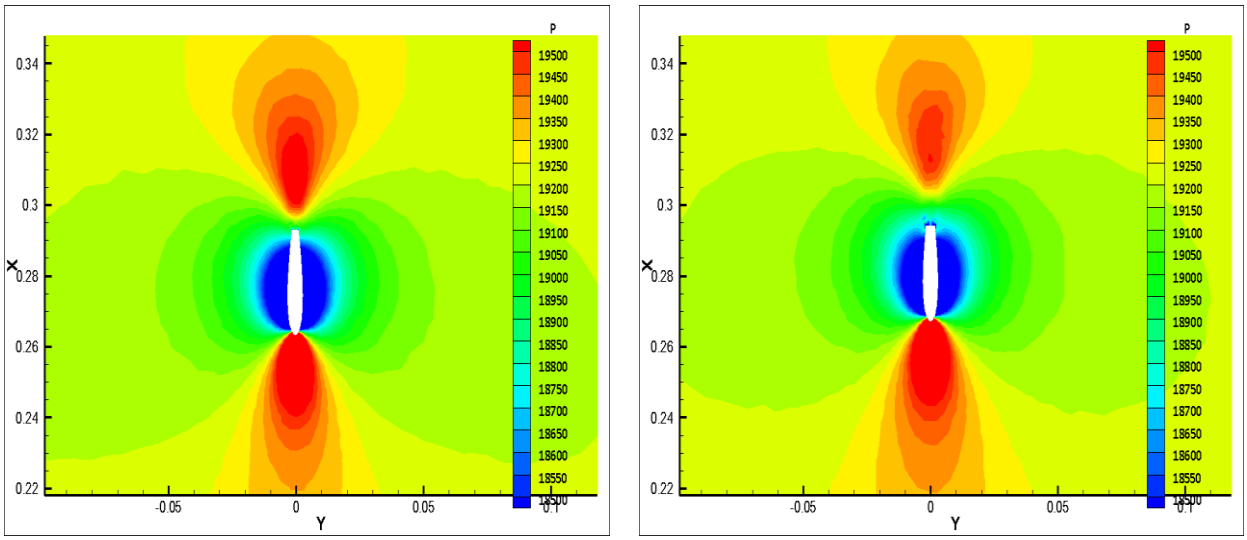

Figure 86. Pressure distribution on Z planes, Z=0.1 m. With circular sting on the left, elliptic on the right; scale 1:180.

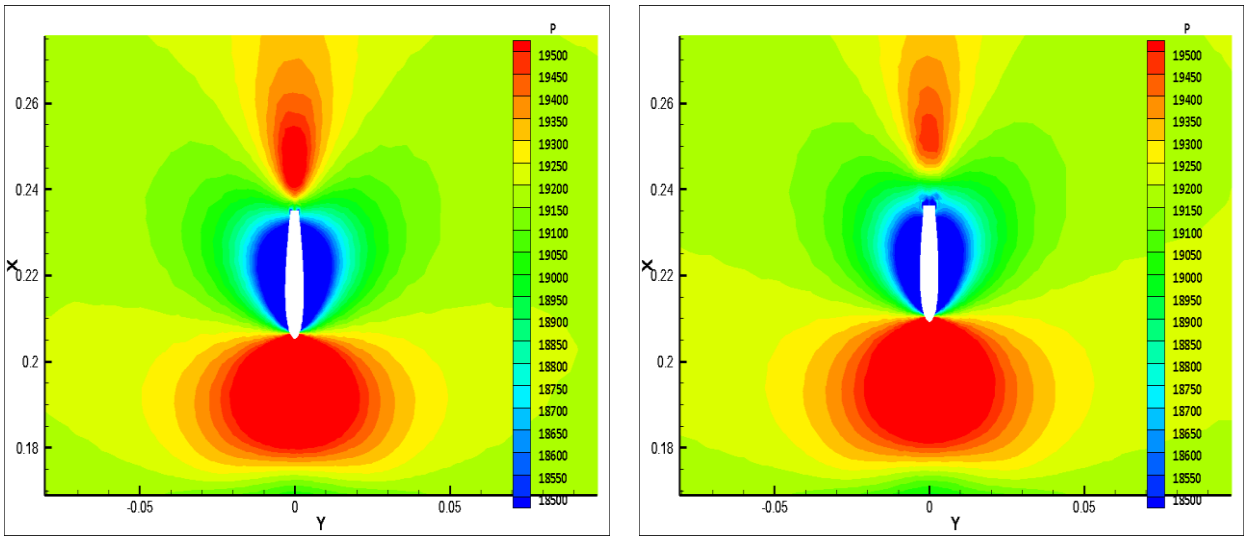

Figure 87. Pressure distribution on Z planes, Z = 0.05 m. With circular sting on the left, elliptic on the right; scale 1:180.

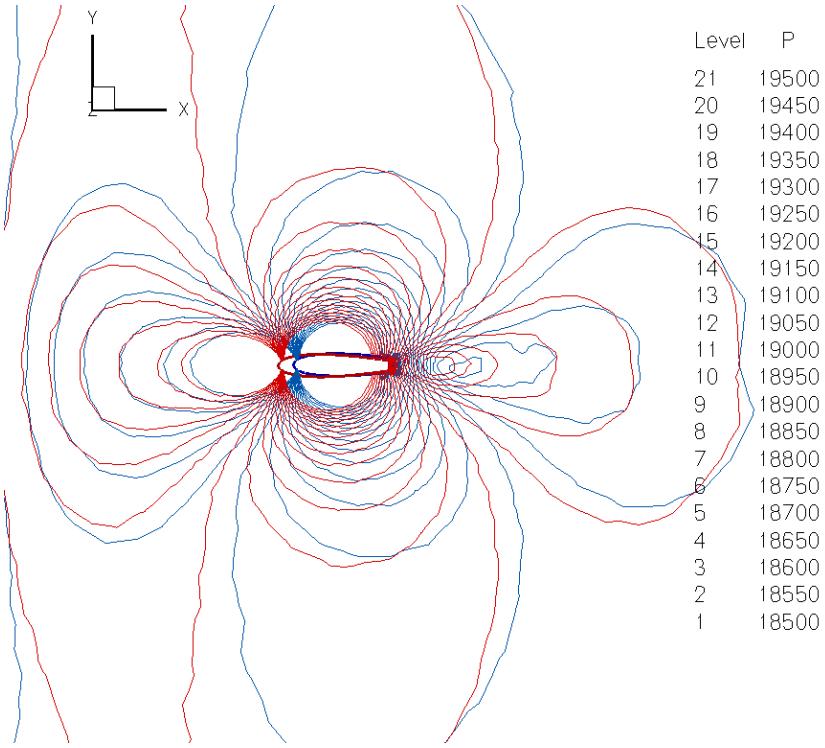

Figure 88. Comparison of the pressure levels of the SOAR with circular sting (red) and elliptic one (blue).

5.7.1.2 Effect of the dimensions variation, scale 1:180, α = 0°

This part of the analysis is performed to understand the impact of different dimensions of the sting performance to assess the sensitivity of the design. The magnitude of the alteration was chosen to 10% because of the constraints arising from the dimensions and instrumentation of the wind tunnel[32].

The effect of the dimensions variation with respect to the nominal conditions was evaluated with:

- one simulation with the longer sting;
- one with the shorter sting;
- one with the larger diameter.

And this is for both sting shapes and either in scale 1:180 either in scale 1:80.

From the results it is expected that a longer sting presents less interferences than a shorter one while the increase of the diameter creates greater interferences too. In fact looking at Figure 89 it is clear that a shorter sting induces a higher pressure on the rear surface of the model than the longer one. On the other hand it is not possible to deduce, clearly, the same behaviour with an increasing of the diameter. This means that we have not to expect significant deviation on the drag with a bigger sting. It is useful to highlight that the differences are always quite small.

[32] For example it is not possible to make the sting too long for the presence of the tail plane of the carrier backward of the SOAR. Similarly it has no sense to make it dramatically shorter because it would produce an important decreasing of the sting performance. In the same way it is not possible to make the sting with a smaller diameter for the existence of the cables inside and it has no sense again to make it really bigger.

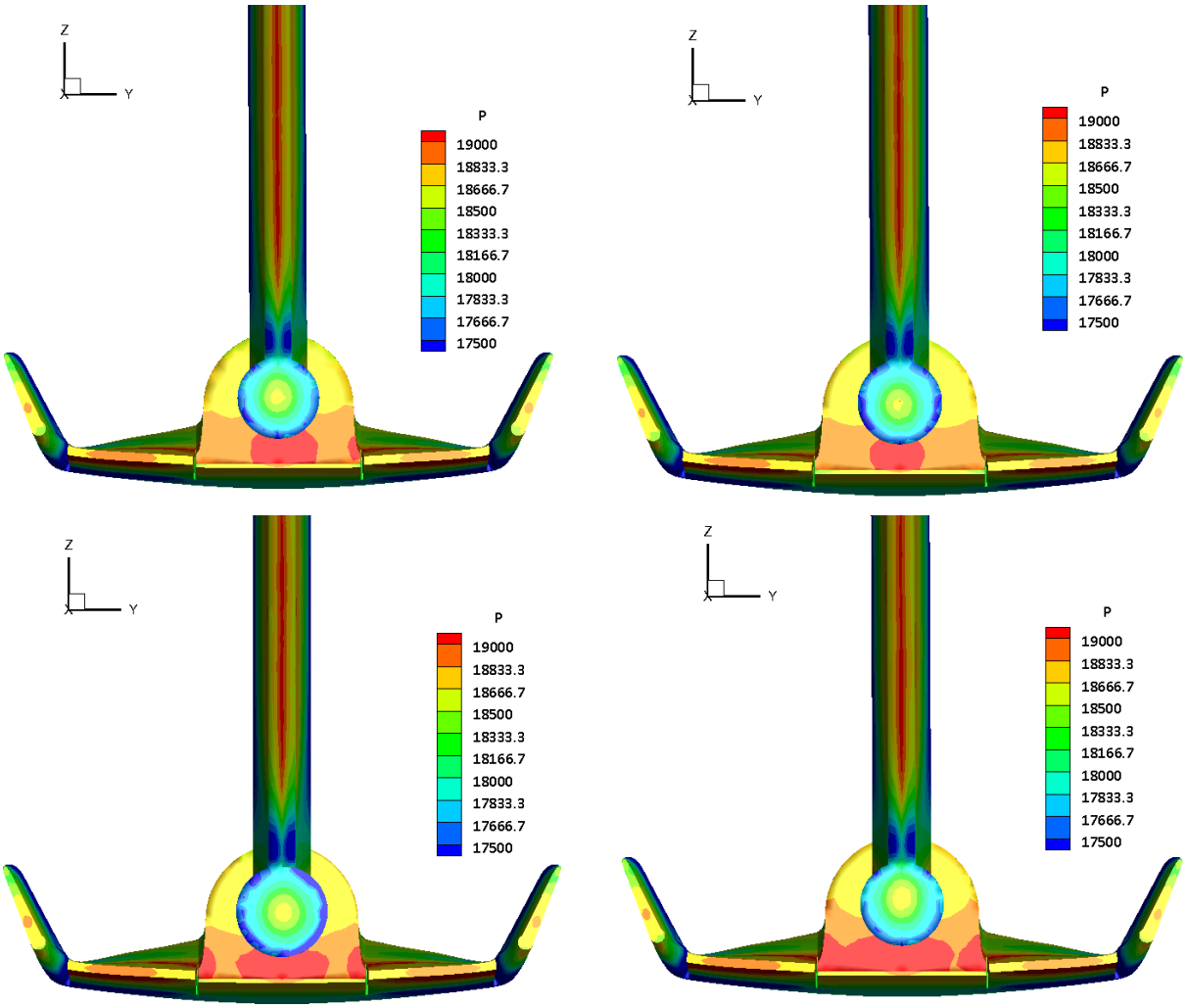

Figure 89.On the top on the left the sting with the nominal dimensions, on his right the longer sting. On the bottom, on the left the sting with a bigger diameter on the right the shorter one; scale 1:180, α =0°

Looking at the top view of the pressure contour it is possible to appreciate that a shorter sting creates an overpressure on the upper SOAR surface that produces a decrease of the lift. Once again the higher pressure is also on the flaps that are far away from the CoG and this means an increase of the pitching moment (see Figure 90 and Paragraph 5.7.2.2). This is due to the greater proximity of the vertical part of the support that brakes the flow over the vehicle.

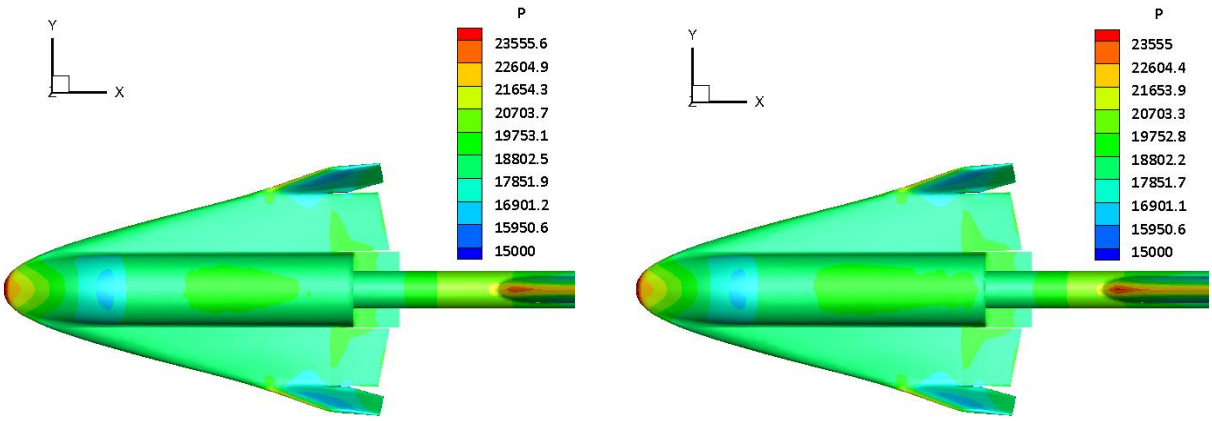

Figure 90. Top view of the SOAR with circular sting pressure contour. Nominal dimensions (left) and 10% shorter (right); scale 1:180.

5.7.1.3 Angle of attack effect, scale 1:180

In presence of an angle of attack the predominant effect on the flow concern to the change of inclination while the different shape of the supports adds minimal differences. On the other hand it will be seen that the dimensional variation has an important impact.

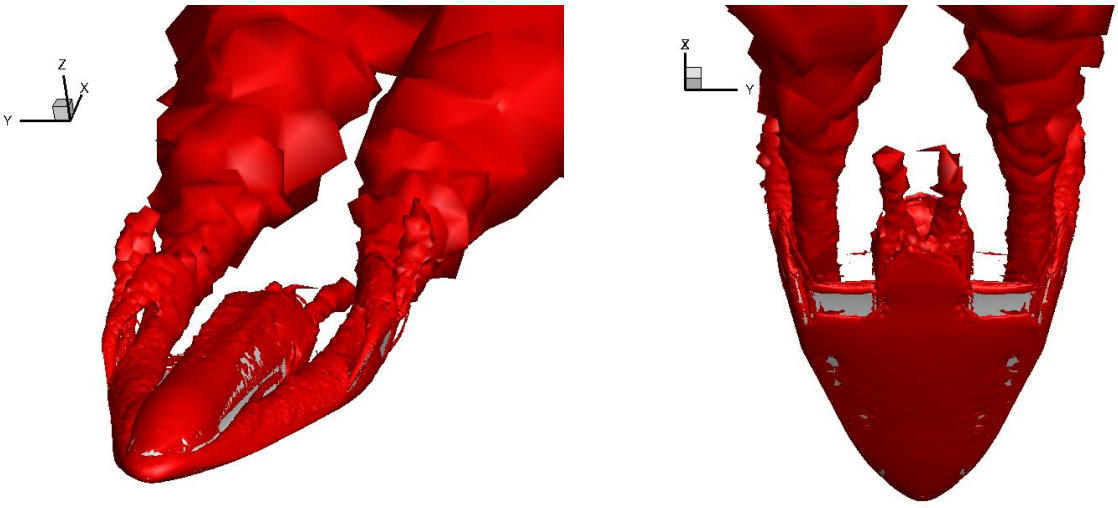

Figure 91. Q criterion=100000 ISO-surface of SOAR alone; scale 1:180, α=15°.

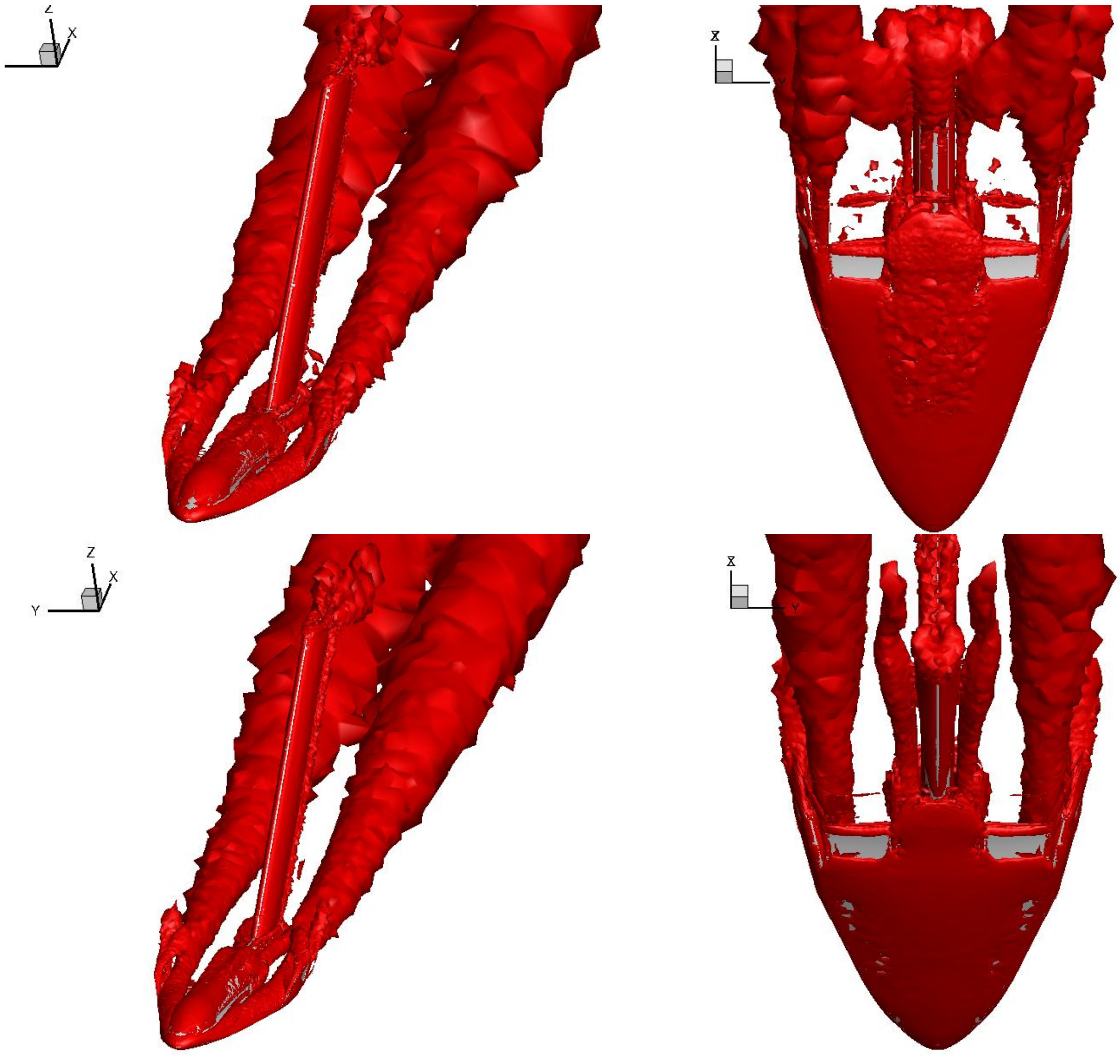

Figure 92. Q criterion=100000 ISO-surface of SOAR with circular sting on the top, with elliptic sting on the bottom; scale 1:180, α=15°.

Regarding the pressure contour differences it is necessary to accentuate the scale and the colour of the plot. The elliptic sting presents a slightly closer pressure distribution to the SOAR alone. It is more uniform than that for the circular one and without peaks of pressure below the sting.

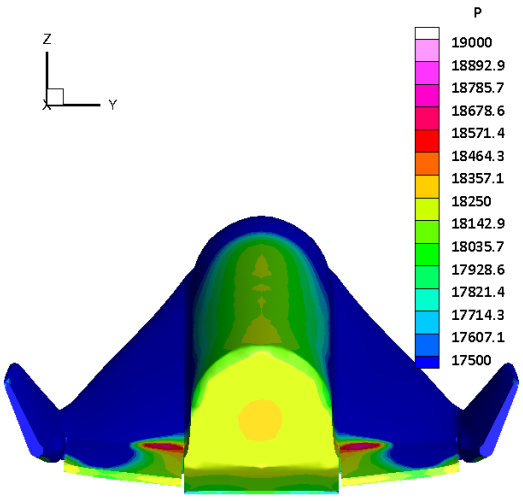

Figure 93. View of the SOAR alone base pressure contour; scale 1:180, α=15°.

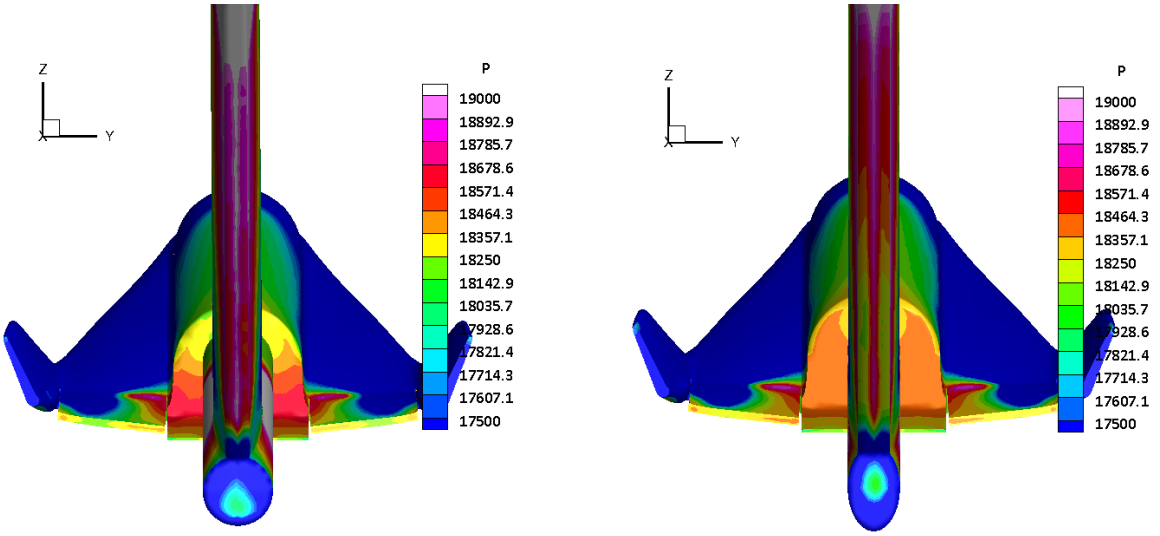

Figure 94. View of the SOAR base pressure contour. On the right the SOAR with elliptic support while on the left with the circular support; scale 1:180, α=15°.

The variation of the dimension, at 15° angle of attack changes the pressure distribution and it has a greater impact on the coefficients than what happens at α=0°. Taking as an example the case of the elliptic sting it is possible to see how the SOAR with the longer one has smaller pressure on the base surface and on the upper one with respect to the case with nominal dimensions. This lower pressure is also present on the SOAR bottom surface but it does not completely equilibrate the previous contribute. This means a lower reduction of drag and lift. Also the moment benefits from this for the lower downward load on the flaps (see Figure 95 and Figure 96).

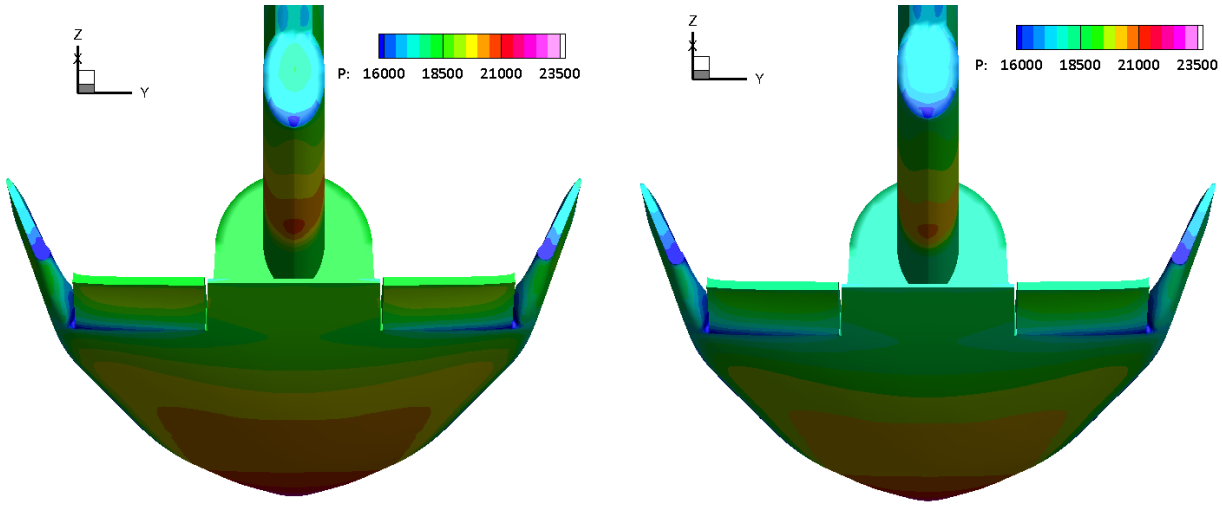

Figure 95. Base view of the SOAR with elliptic sting pressure contour. On the right with the sting 10% longer, on the left with the nominal dimensions; scale 1:180, α =15°.

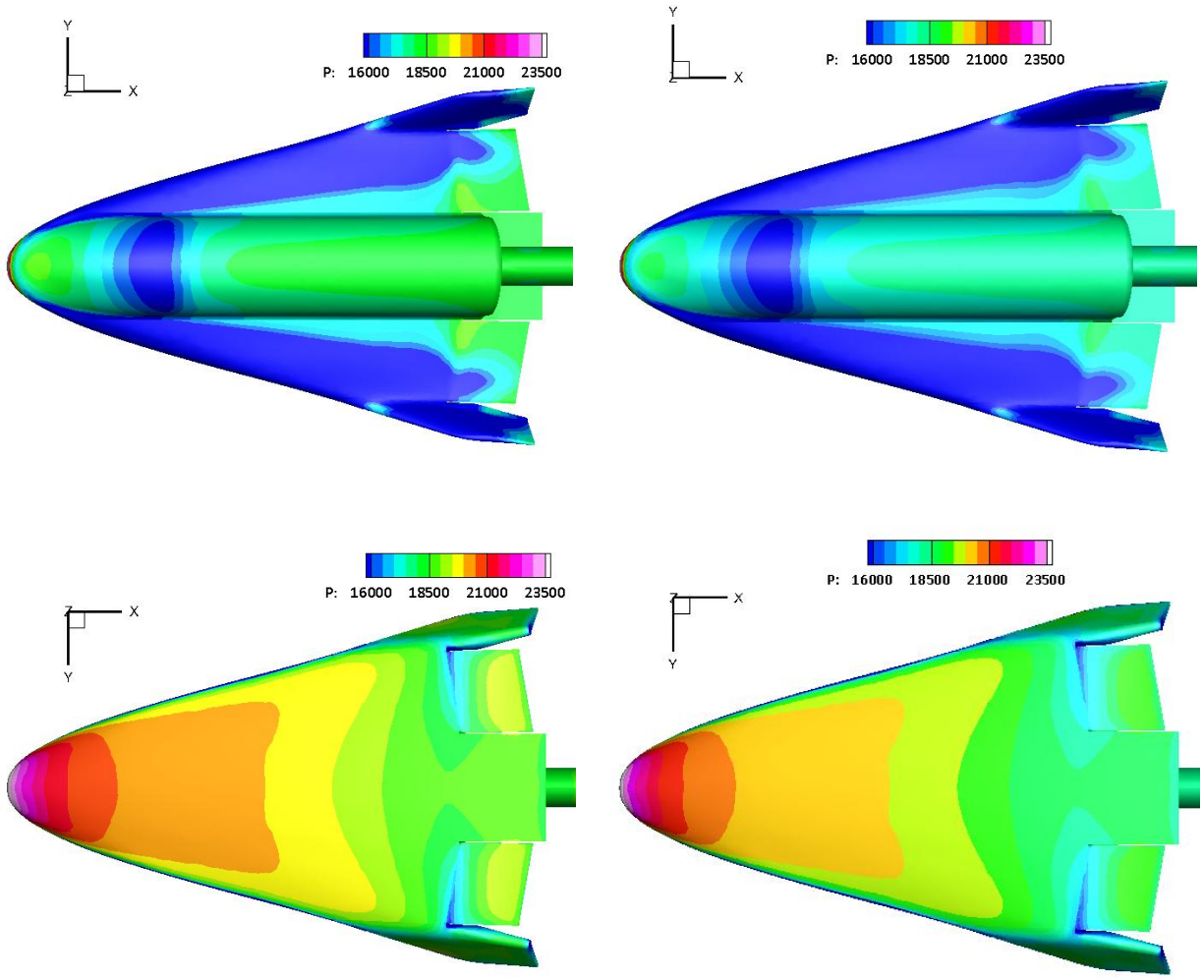

Figure 96. Bottom and superior view of the SOAR with elliptic sting pressure contour. On the right with the sting 10% longer, on the left with the nominal dimensions. α =15°.

5.7.1.4 Effect of the inclination variation, scale 1:180, α=0°

The differences on the pressure distributions are really appreciable only with 15° of variation. Growing the inclination it is possible to see an increase of the pressure on the base surface and on the upper one, especially in the rear part. Otherwise on the bottom it is not possible to notice strong differences. This, as it is already cleared, means a decrease of the drag and of the lift while the pitching moment growths. The global result is an increasing on the interferences (see Figure 97).

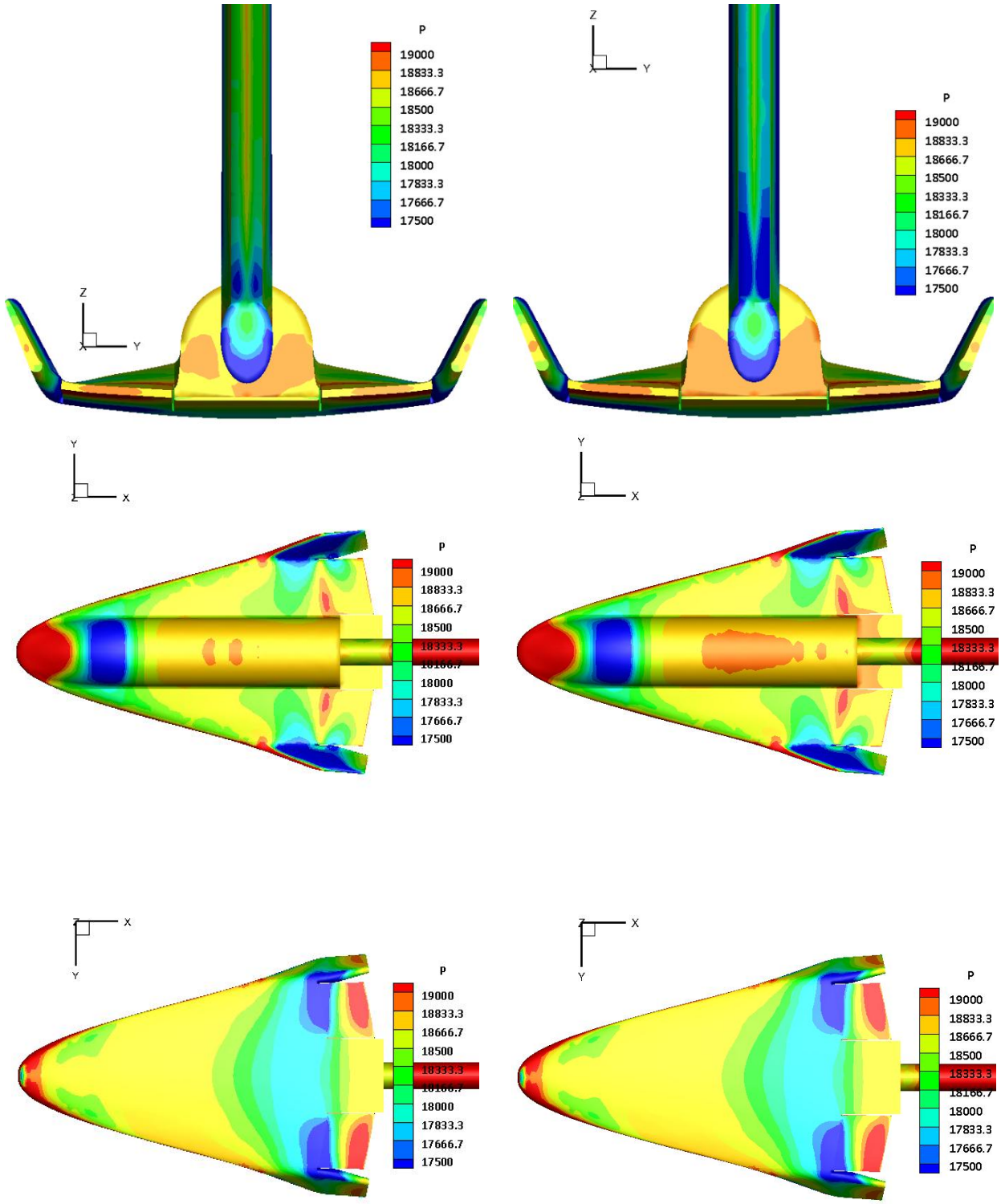

Figure 97. Different view of the SOAR with elliptic support. On the right β=55,8°, on the left β=40,8°; scale 1:180

5.7.1.5 SOAR alone and with straight support, scale 1:80 α=0°

As expected straight stings perturbs less the flow than any supports with an inclined part. Regarding the SOAR alone the same phenomena of the scale 1:180 are presents. The adding of a

sting produces a refinement in the mesh near the wake that permits to see the extensions of the two vortexes at the sides of the sting.

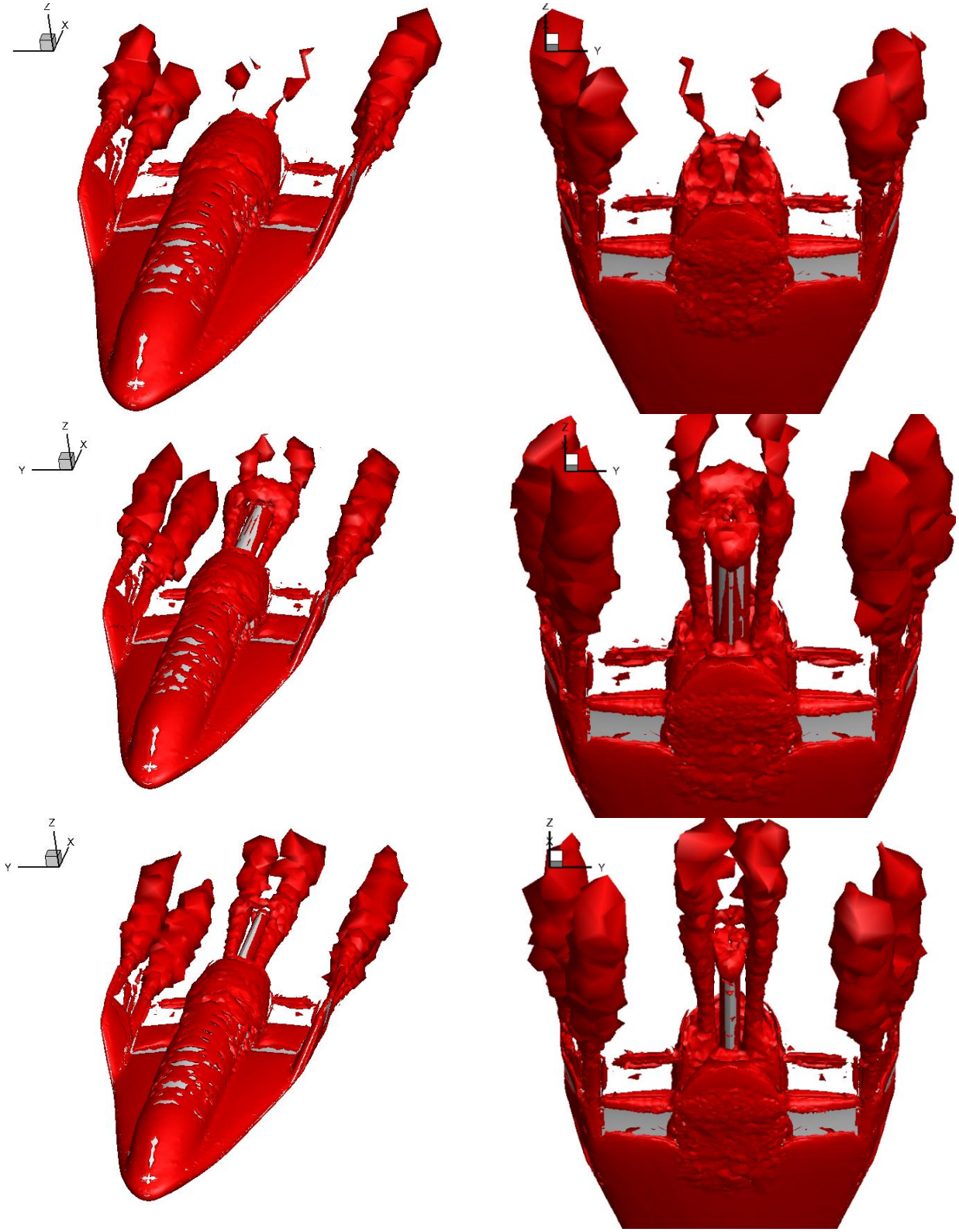

Figure 98. Q criterion=100000 ISO-surface of SOAR alone on the top, SOAR with circular sting in the middle and with elliptic on the bottom; scale 1:80, α =0.

The smaller perturbation of the flow with a straight sting appears also from the Mach number contour where the sting breaks less the velocity flow field (see Figure 99).

Even if the straight sting has a more streamlined shape and produces less interference on the SOAR, from the pressure contours it is possible to perceive an increase of pressure on the rear part due to the presence of the sting. To see this it was necessary to slightly change the contour resolution in Figure 100 and Figure 101 with respect to what was for the 1:180 scale (see Figure 81 and Figure 82). Since there are no large parts sticking out of the wake, the effects are small.

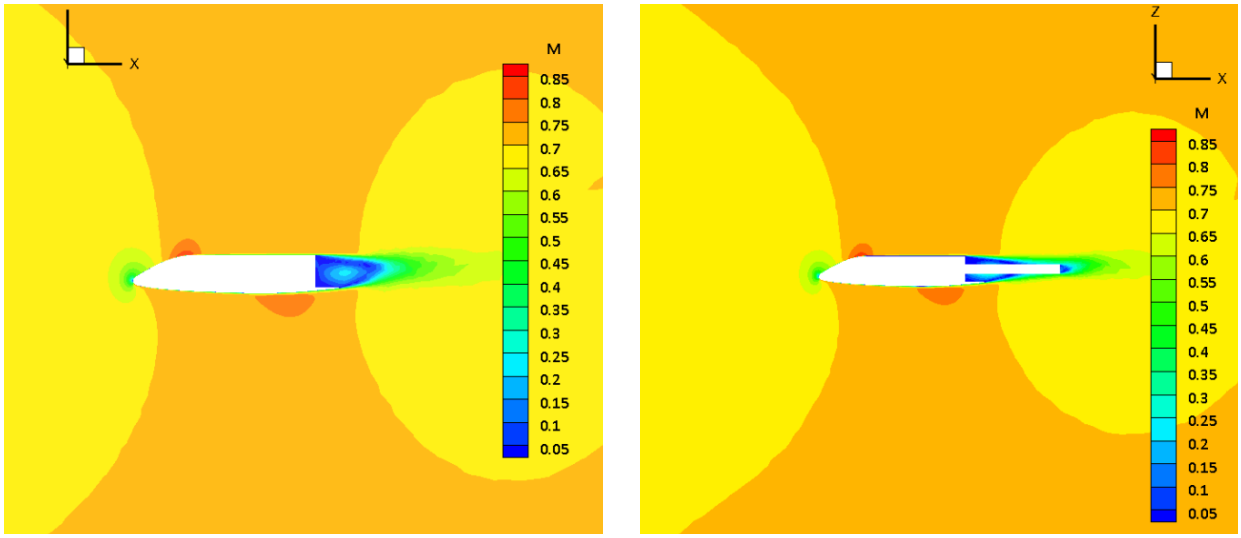

Figure 99. Mach contour, on the left the SOAR alone, on the right with circular sting; scale 1:80, α=0°.

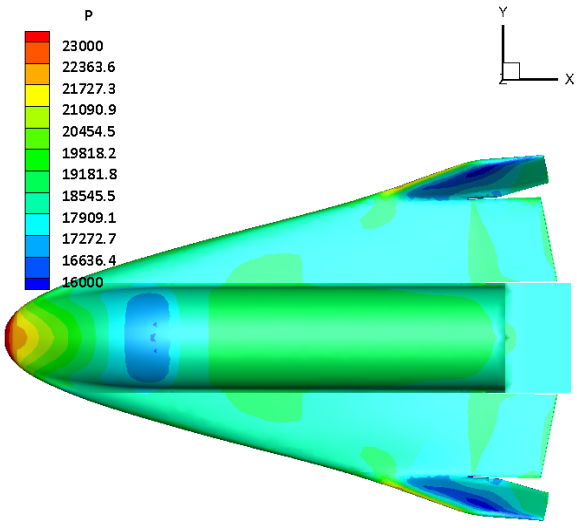

Figure 100. Top view of the SOAR pressure contour; scale 1:80, α=0°.

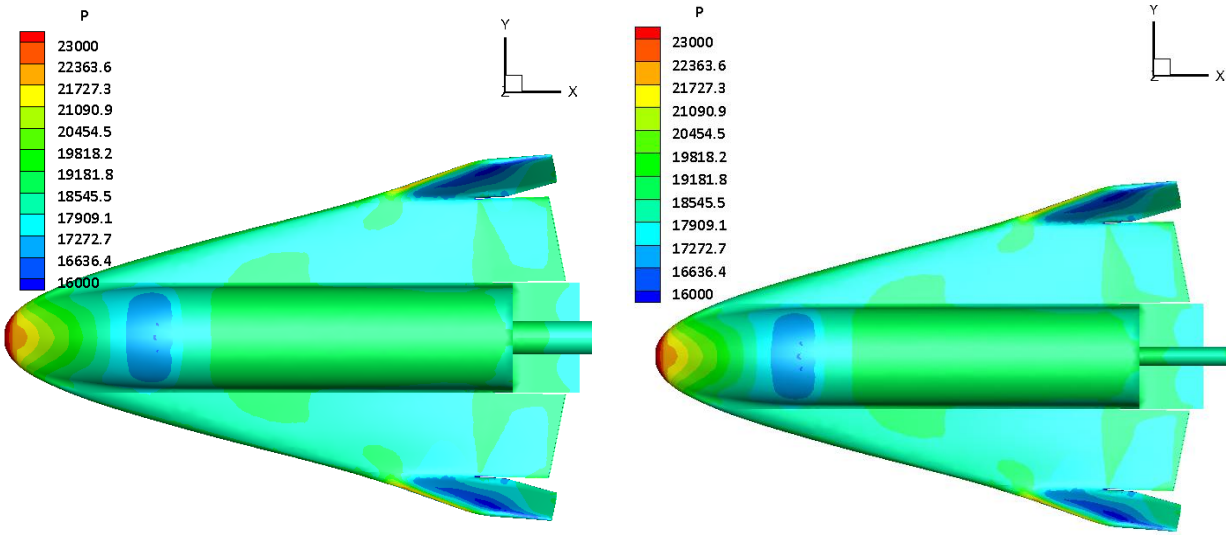

Figure 101. Top view of the SOAR with circular sting on the right and with elliptic sting on the left; scale 1:80, α=0°.

Unlike what was for the scale 1:180 support the pressure which growth over the vehicle surface is much lower, a plot similar to Figure 83 is not reported because no visible differences were detectable.

Regarding the rear part of the vehicle also the straight sting causes an increase of the pressure on the back surface of the SOAR. This phenomena is more evident (and follow the expected trend) with the circular sting than with the elliptic one. Once again the circular shape induce a larger blockage of the flow below the sting (see Figure 103). Also here the presence of little asymmetries is for the same reasons explained in Paragraph 5.7.1.1.

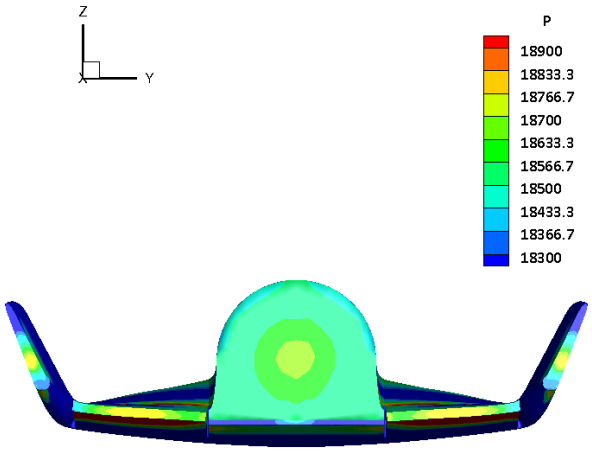

Figure 102. Back view of the SOAR alone; scale 1:80, α=0°.

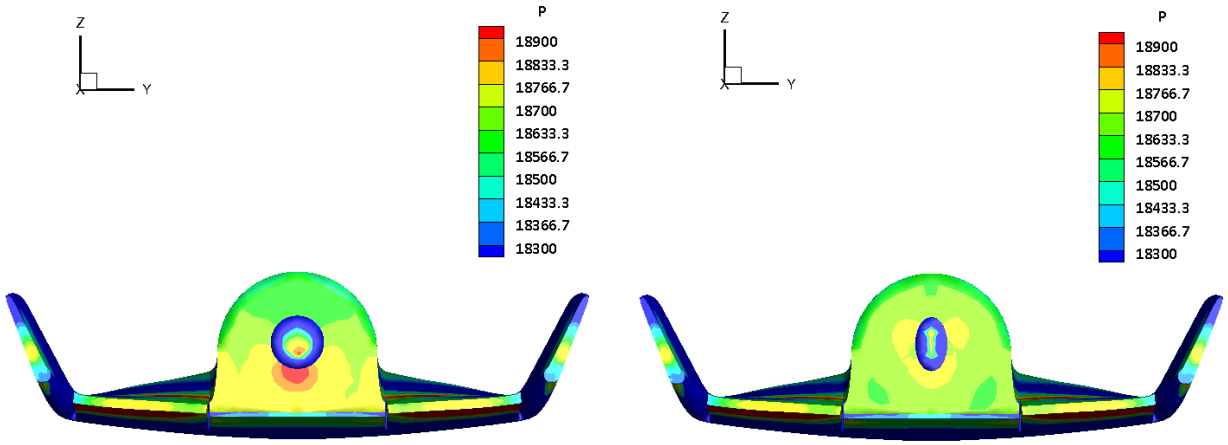

Figure 103. Back view of the SOAR with circular sting, on the left and with elliptic one, on the right, scale 1:80, α=0°.

5.7.1.6 Effect of the dimensions variation, scale 1:80, α = 0°

The 10% dimensional variations on the straight sting produce minimal differences on the pressure contours. Now a sting shorter sting causes a lower pressure on the vehicle base with a behaviour closer to the SOAR alone. The reason of this can be double:

- first at all it is necessary to remind the theory that for turbulent flow at the base predicts a shorter critical sting length;
- second with this model of sting there are not any inclined parts out from the wake of the SOAR. In fact the disturbances of the scale 1:180 support were bigger when the vertical part is closer to the vehicle, that is with a shorter sting. On the other hand, with only a straight sting, shorter it is lower are the perturbation on the wake, even if the amount of the interferences is always smaller.

It is difficult to clarify this trend because in the reality at the end of the sting there is another structure usually with a larger diameter. The effect of this bigger diameter component can be

similar (but smaller and depending of the diameter variation) of what induced an inclined bar, that is to increase the flow blockage as closer is to the vehicle. To conclude it is also necessary to say that the differences are always so small that non stationary transient phenomena could affect them.

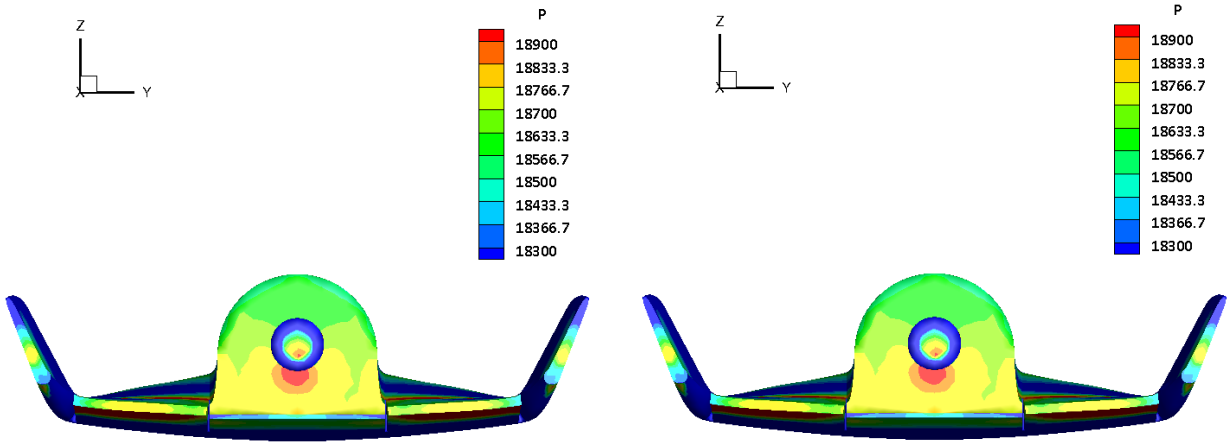

Figure 104. On the left the sting with the nominal dimensions, on his right the sting longer; scale 1:80, α =0°.

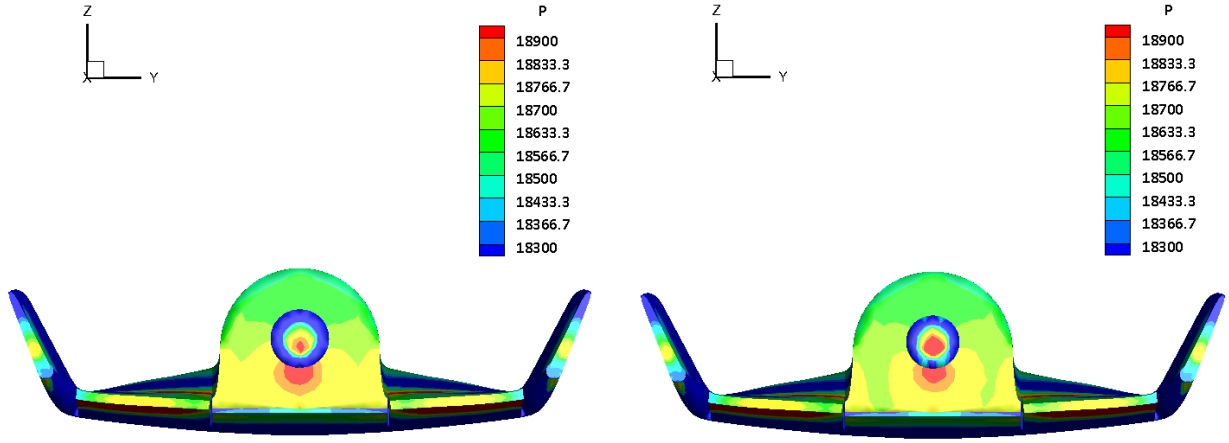

Figure 105. On the left the sting with a bigger diameter on the right the 10% shorter one; scale 1:80, α =0°.

5.7.1.7 Angle of attack effect, scale 1:80

The presence of the sting involves minimal differences with respect to the case without it. The effect of the angle of attack prevails over the influence of the sting on the flow topology and also on the pressure contour. As it is possible to see in Figure 106.

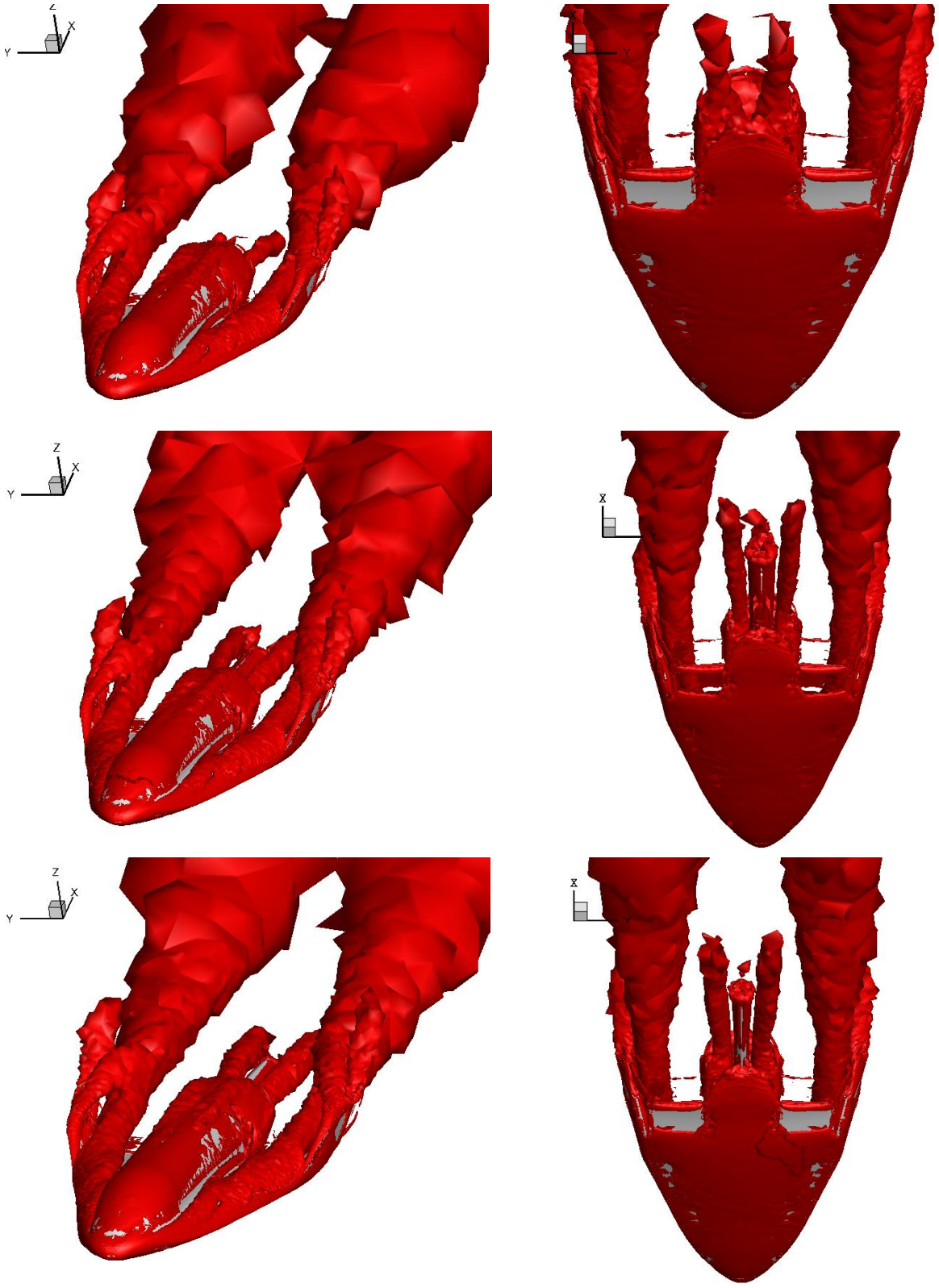

Figure 106. Q criterion=100000 ISO-surface of SOAR alone on the top, with circular sting in the middle, with elliptic sting on the bottom; scale 1:180, α=15°.

Looking at the pressure contour on the base it is necessary to accentuate the scale and the colour of the plot to see some differences[33]. Once again the base of the SOAR with circular sting

[33] Switching it from "small rainbow" to "large rainbow".

presents a slightly more different pressure contour from the SOAR alone than what happens with the elliptic sting.

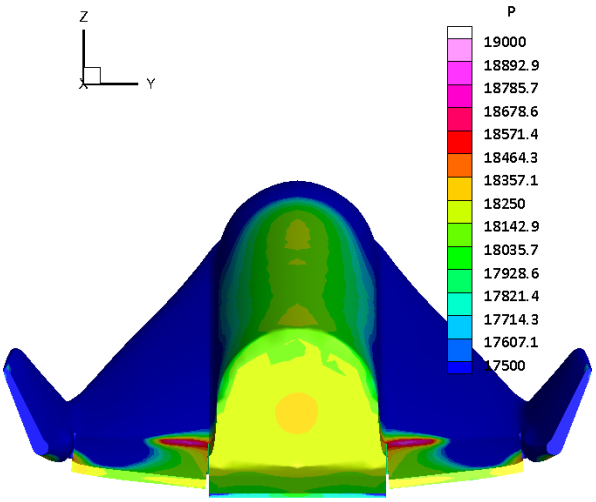

Figure 107. View of the SOAR alone base pressure contour; scale 1:80, α=15°.

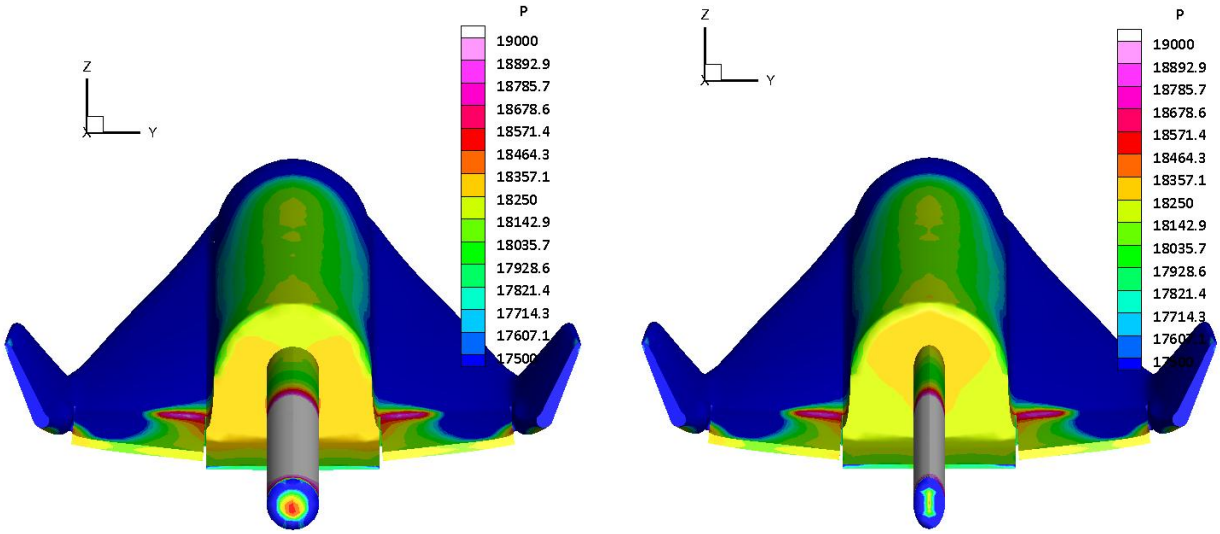

Figure 108. View of the SOAR base pressure contour. On the right the SOAR with elliptic support while on the left with the circular support; scale 1:80, α=15°.

Combining a dimensional variation, such as sting 10% longer and 15° of angle of attack it is possible to see small differences on the SOAR base surface. That means a little impact on the drag. On the other hand greater differences are present on the upper and the lower surface of the flaps, while on the rest of the SOAR top and bottom surface the variances are minimal. The increasing of the pressure prevails on the bottom of the flaps and this involves a growth of the lift and a decreasing of the pitching moment (See Figure 109).

Increasing 10% on the diameter the differences on the pressure contour are negligible and only on the coefficients small variations are appreciable.

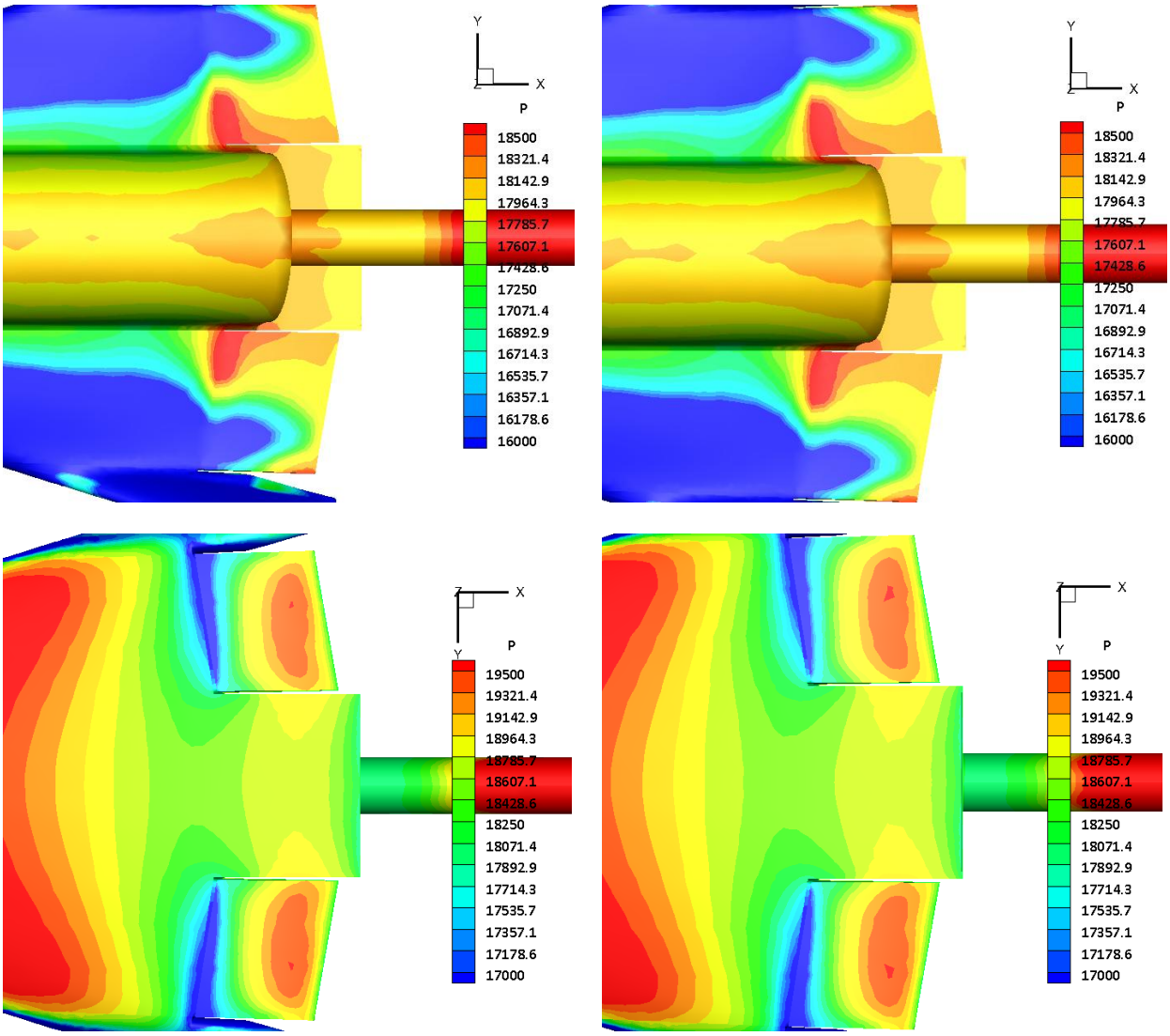

Figure 109. View of the top and bottom flap surface. Circular sting with nominal dimensions on the left, 10% longer on the right; scale 1:180, α=15°.

5.7.2 Aerodynamic coefficients

In this paragraph the aerodynamic coefficients found during the computation are presented. For every simulation, with a different kind of supports, corrected coefficients[34] of the SOAR vehicle are compared. The attention is focused on the comparison between the different cases.

5.7.2.1 Scale 1:180, comparison of the different shape as a function of α

The presence of the support always induces a decrease of the drag and of the lift on the SOAR. On the other hand the pitching moment raises. The reason of this behaviour is consistent with the alteration of the flow and of the SOAR pressure contour already discussed in paragraph 5.7.1.1.

[34] The coefficients here presented are corrected for the zero pressure body-support intersection (see paragraph 5.4).

About the drag and the lift the effect is minimal with small angle of attack, for both shapes and it increases at 15°. Raising α the advantages of the elliptic shape are evident also with a reduction of interferences on the lift. On the other hand for the moment the interferences are more important also at small angle presenting a constant trend with the angle of the flow. Also in this case the usage of an elliptic sting produces less interference. See Table XXVI and ANNEX B for all tabulated results.

In the following plots the deviations compared to the SOAR alone case are presented. SOARWS means the SOAR alone coefficients from a simulation with the presence of the support.

$$\Delta C = \Delta C_{Soar} - \Delta C_{SoarWS}$$

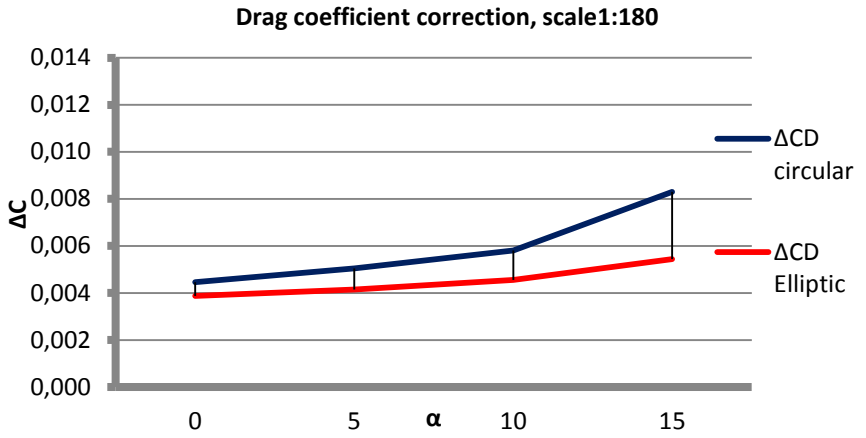

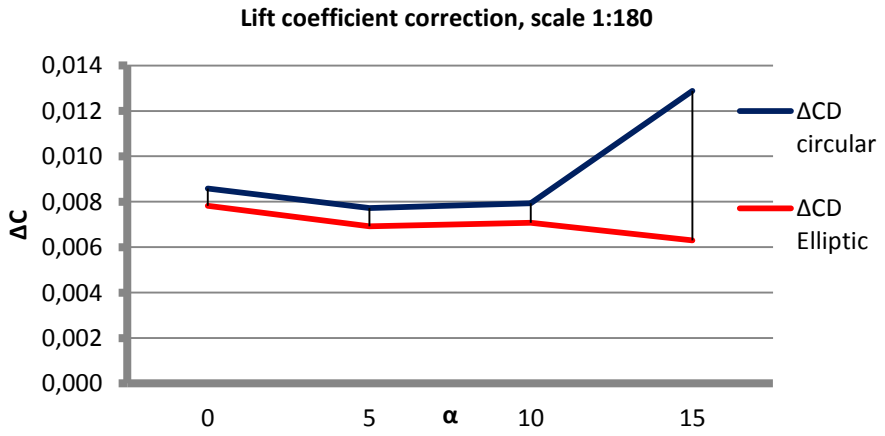

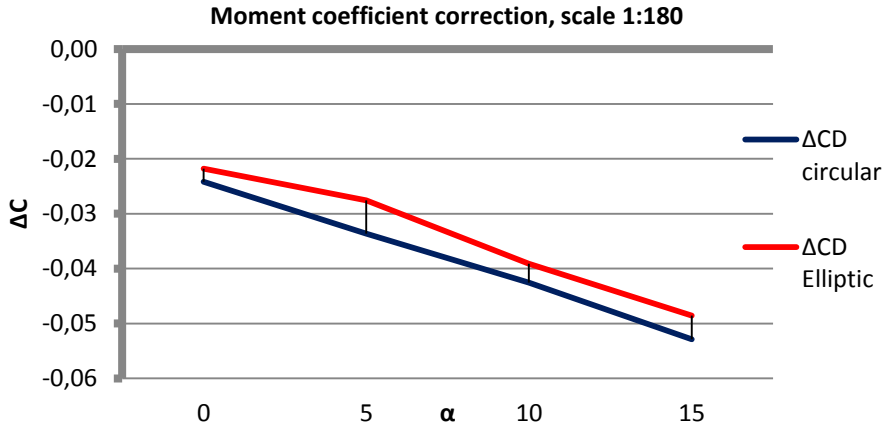

Table XXVI. Average correction on the SOAR alone coefficient, for value of α between 0° and 15°; scale 1:180.

Simulations	ΔCD Av.	ΔCL Av.	ΔCM Av.
SOAR with circular sting	0.00590	0.00928	-0.03831
SOAR with elliptic sting	0.00451	0.00703	-0.03425

5.7.2.2 Comparison of different sting dimensions, scale 1:180, α=0°

As expected a longer sting always presents less interferences than a shorter one. With a moderate variation of length the effect is minimal. It is not possible to notice any differences in the trend between the two sting shapes. A 10% length reduction produces larger changing than a 10% increase (see Table XXVII). The only unclear point is the behaviour of the drag coefficient for the circular sting.

A changing of 10% in the diameter does not produce any substantial effect, except for a little worsening of the elliptic sting performances and a small increase in the pitching up moment. For all values see ANNEX B and the plots of the coefficient variations of paragraph 5.7.2.3 (also with α = 0°).

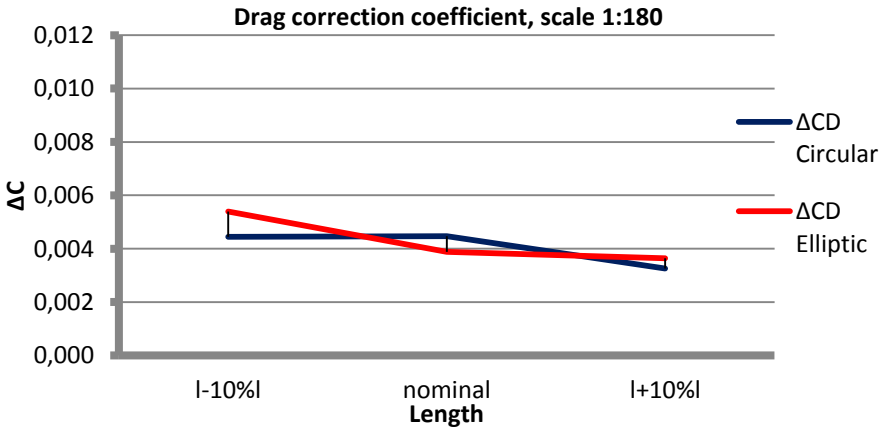

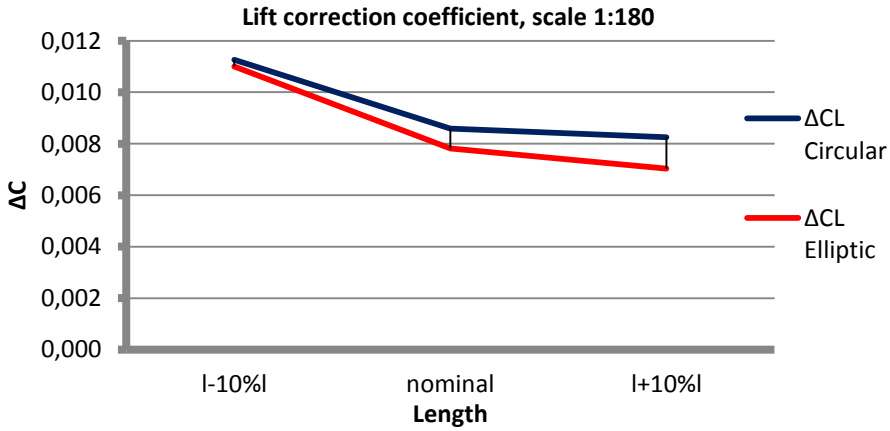

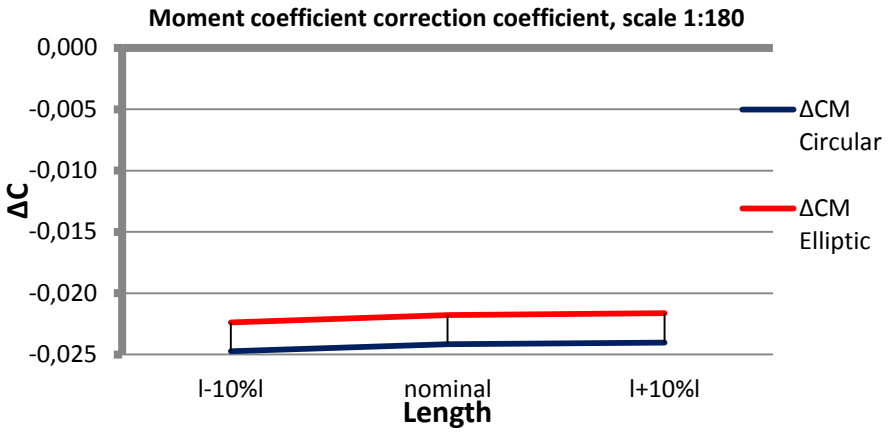

Table XXVII. Variation in the correction value between diverse length simulations. Each difference is subtract to the same value but with a shorter sting. Interferences decrease with negative ΔΔCD, ΔΔC and positive ΔΔCM. This table is useful to understand the improvement reached with the dimensional variation.

Simulations	ΔΔCD	ΔΔCL	ΔΔCM	ΔΔCD	ΔΔCL	ΔΔCM
	With circular sting			With elliptic sting		
l-(l-10%)	0.00002	-0.00268	0.00059	-0.00152	-0.00319	0.00061
(L+10%)-l	-0.00121	-0.00034	0.00013	-0.00024	-0.00078	0.00016

5.7.2.3 Comparison of the dimensions variation with an angle of attack, scale 1:180

At 15° it is possible to see that the trend, for the drag and the lift, is quite the same that with α=0°. Interesting is the drastic reduction of pitching moment interference for the longer elliptic sting. This fact is not present with the circular shape, while in scale 1:80 it is present with both shapes.

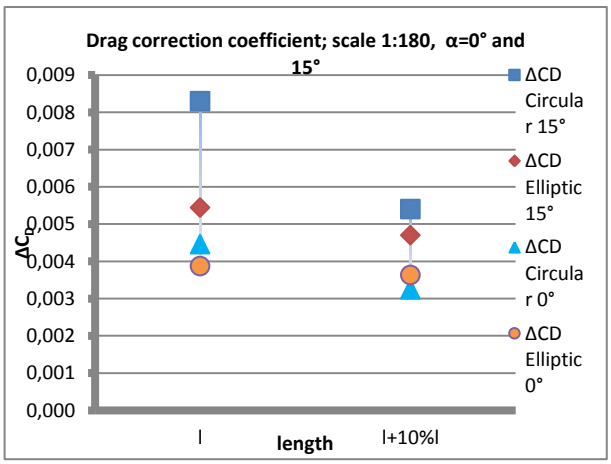

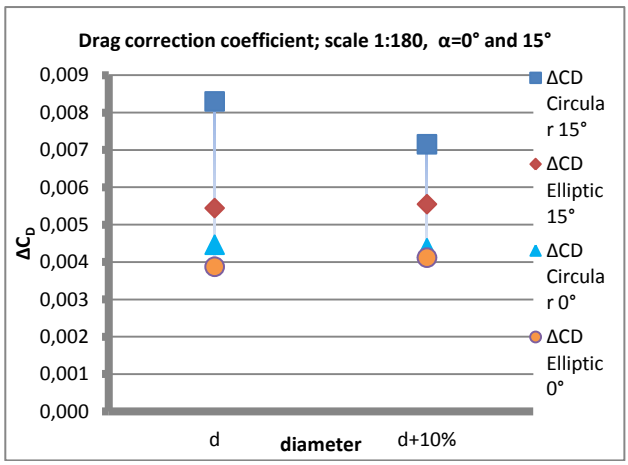

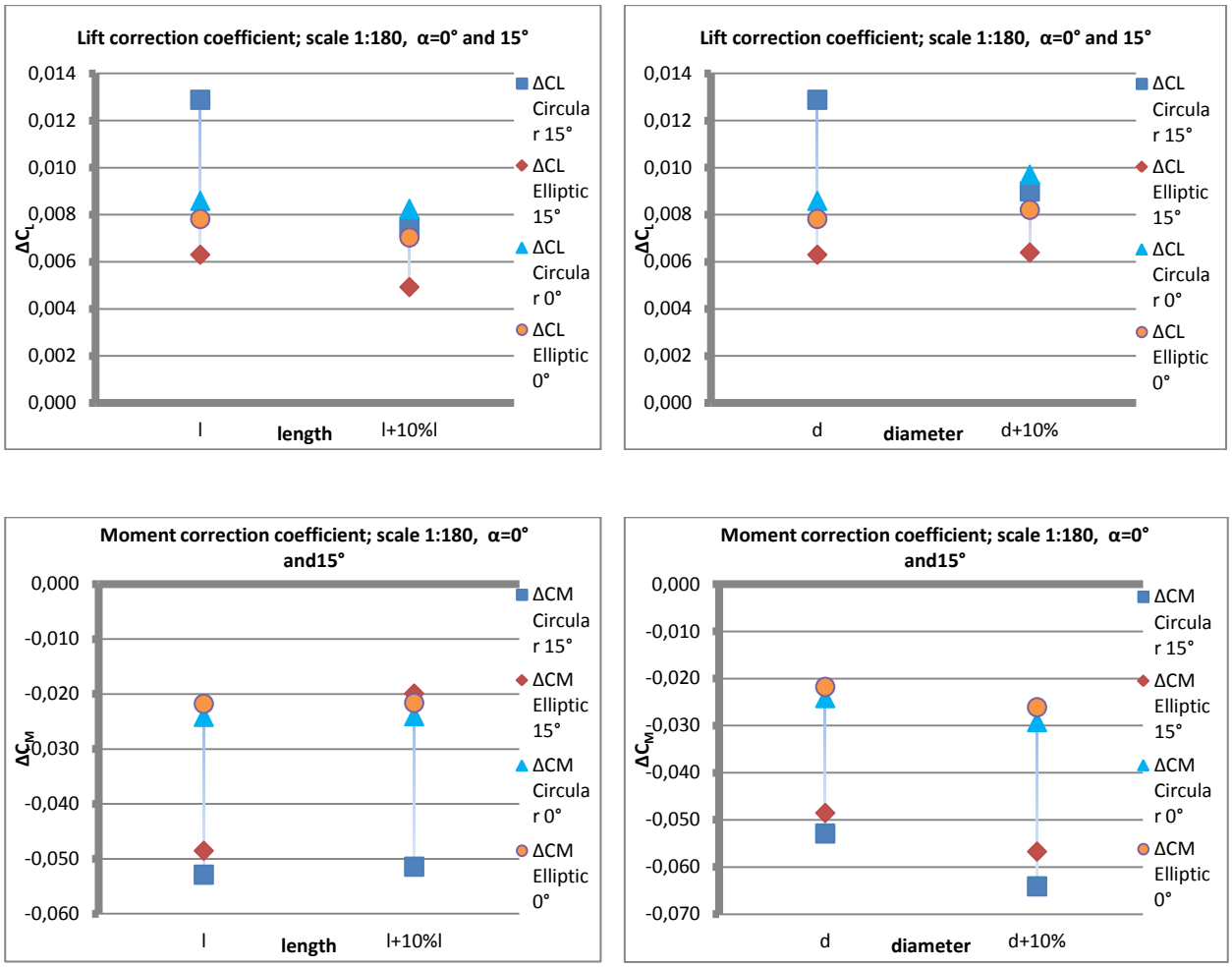

5.7.2.4 Comparison of different support inclination, scale 1:180, α=0°

A variation on the inclination of the supports vertical part of 5° manifests minimal differences on the interference. If the change is of 15° the differences are to be taken into account. The trend suggests worse interferences by increasing the angle (that is with an inclined part close to the vertical). About the drag the circular sting seems to allow better performance with the inclinations of 45.8° and 50.8°than the elliptic one.

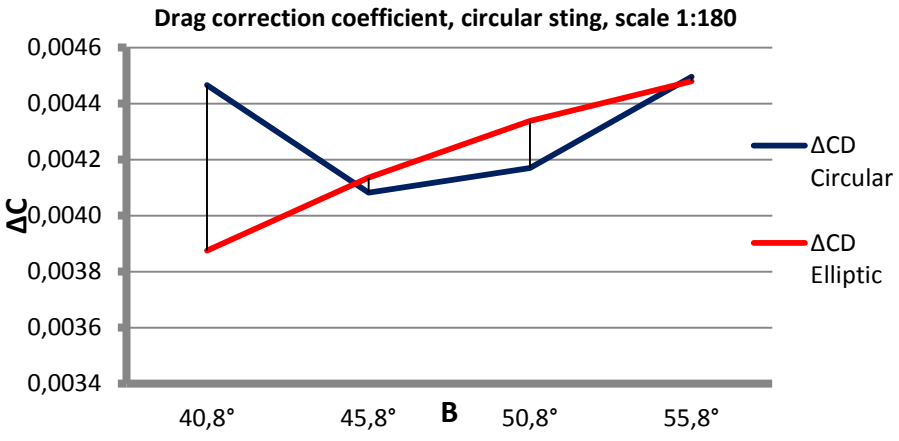

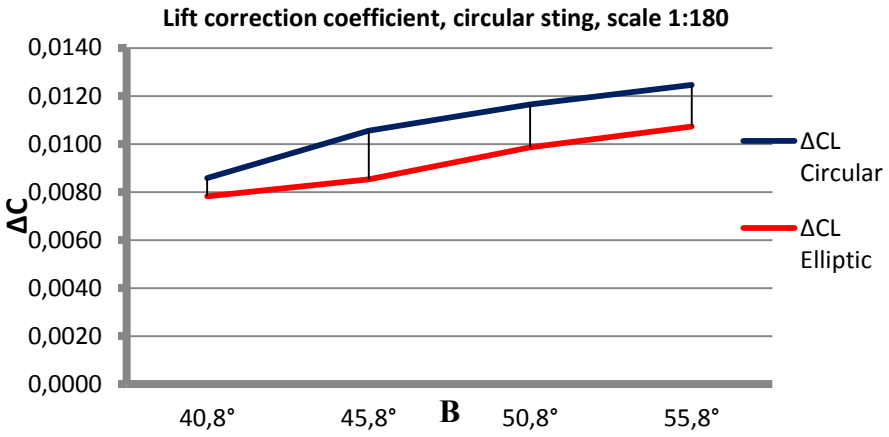

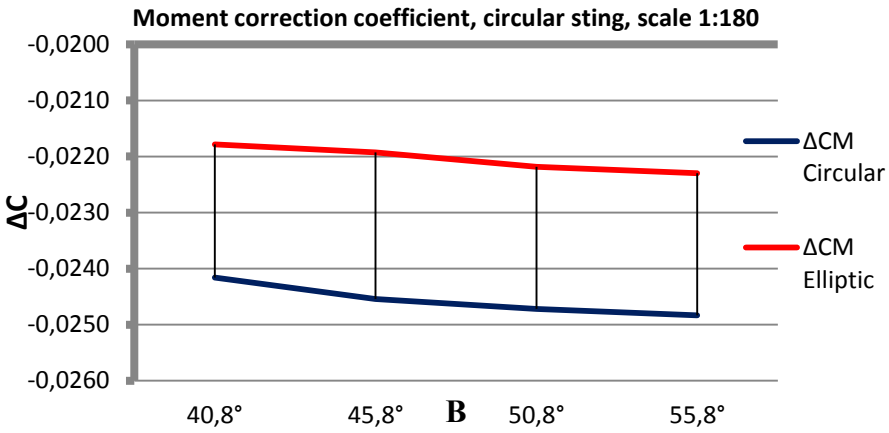

5.7.2.5 Scale 1:80, comparison of the different shape as a function of α

Also the straight sting induces the same kind of interferences, that is the decrease of the drag and the lift and increases the pitching moment. Once again it is possible to understand the origin of this behaviour from the pressure contour. See paragraph 5.7.1.5.

As expected the shape of the sting in scale 1:80 is more adequate to reduce the interference with the vehicle (it can be relatively smaller compared to the 1:180 case). In effect the deviance with respect to the drag and to the lift from the SOAR alone are actually small. For the pitching moment greater interferences persist and, once again, the elliptic sting has a better behaviour. This is due to the presence of the SOAR flaps under the sting that induce a higher pressure again.

Comparing Table XXVIII with Table XXVI it is possible to see how the correction in scale 1:80 is usually lower than what happen in scale 1:180.

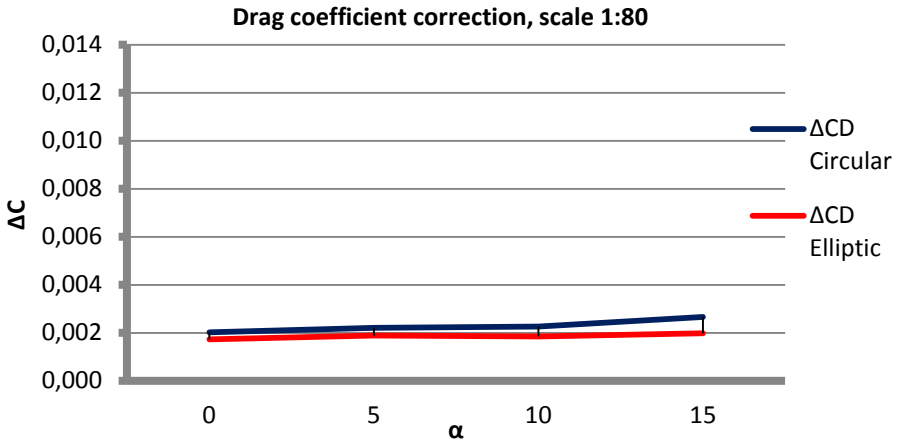

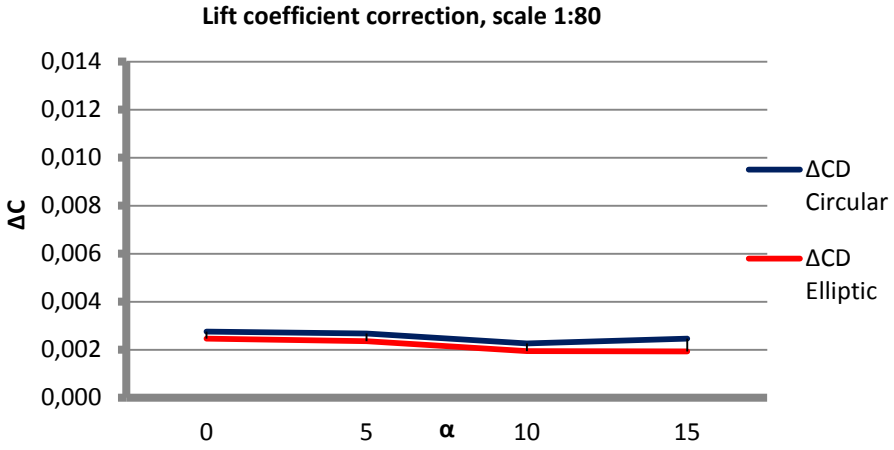

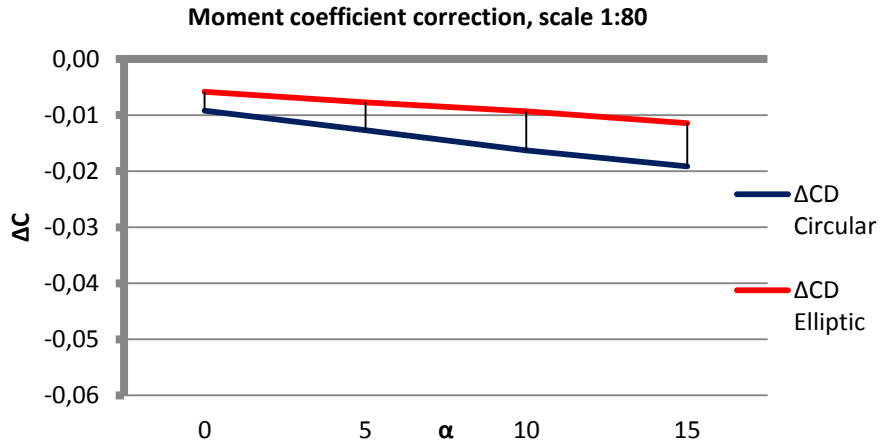

Table XXVIII. Average correction on the SOAR alone coefficient, for value of α between 0° and 15°; scale 1:80.

Simulation	$\Delta C_{D\,AV}$	$\Delta C_{L\,AV}$	$\Delta C_{M\,AV}$
Circular	0.00229	0.00254	-0.01434
Elliptic	0.00186	0.00217	-0.00857

5.7.2.6 Comparison of different sting dimensions, scale 1:80

The small differences on the pressure distribution discovered in paragraph 5.7.2.6 are not visible on the aerodynamic coefficients. The only remarkable aspect is the lift better performance at 15°

with the elliptic shape. In fact while the circular sting seems to have a worse behaviour the elliptic one improves.

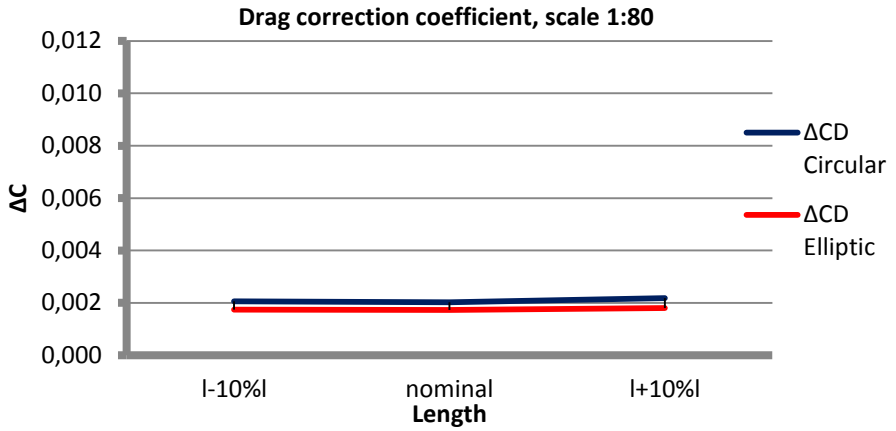

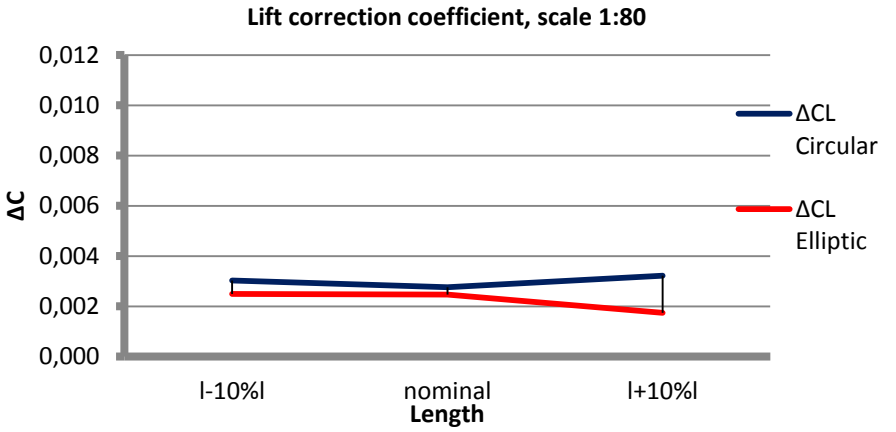

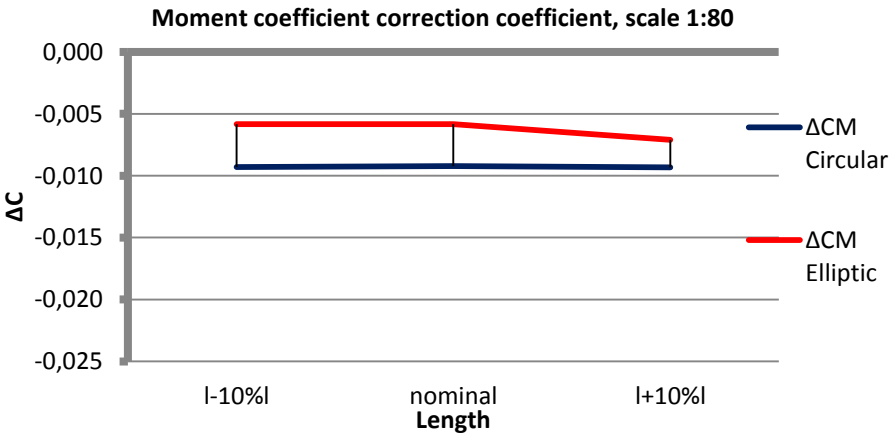

A changing of the 10% in the diameter produce a greater effect in scale 1:80 than what happens in scale 1:180. Also this time there is a little increase of the drag interferences for the elliptic one while the circular shape is not affected. About the lift the differences are minimal, while for the pitching moment the greatest deviance is observed. The magnitude is about 0.029 for the circular and 0.026 for the elliptic. All values are tabulated in ANNEX B and the plots of the coefficient variations (also with $\alpha = 0°$) are in the next paragraph.

5.7.2.7 Comparison of the dimensions variation with an angle of attack, scale 1:80

The variation of dimensions at α=15° presents the same trends than of α=0° for the drag, while the tendency of the lift is not the same. With regard to the pitching moment it is possible to see that with a sting 10% longer the interferences dramatically decrease.

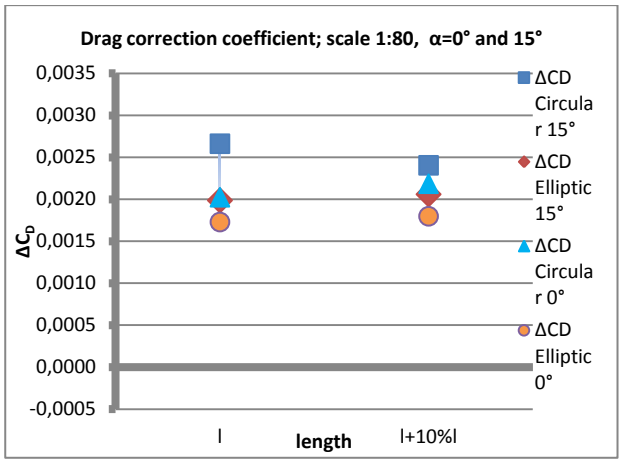

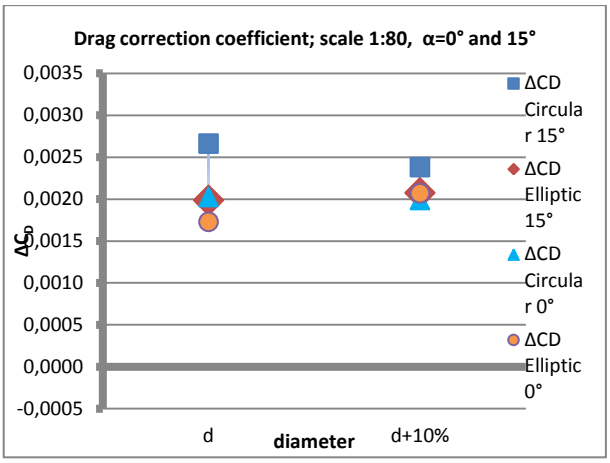

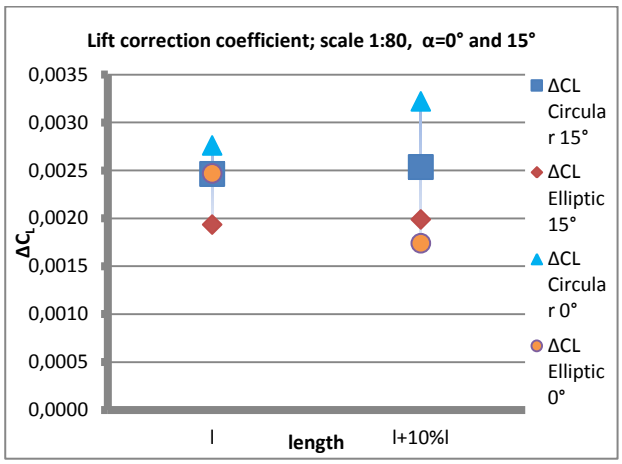

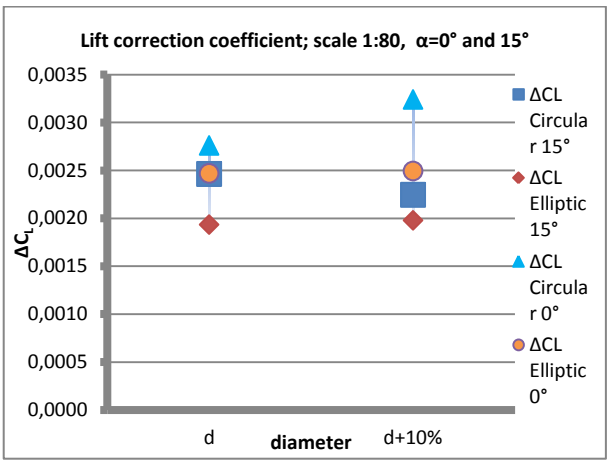

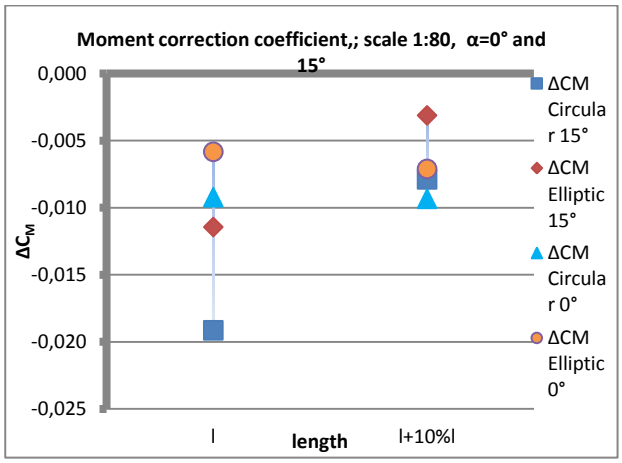

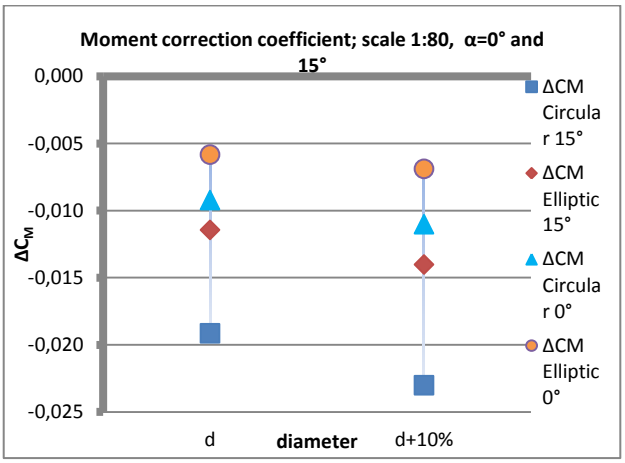

5.8 Comparison with the previous support

It is useful to remind that this study and support design rose from the necessity to build new supports after the first wind tunnel testing campaign in VKI. All results of that research activity are in [1].

The old support was attached to the vehicle from the top (dorsal strut)[35] and it was discovered to induce high interferences. That support configuration induced an extra pressure in front of the sting and lower pressure on the side. Furthermore lower pressures were presented on the base of the SOAR and on the top of the flaps. These decrease of pressures induced large forces due to the big areas it was acting on. In effect a lower pressure was generated behind the body and over the flaps with the double effect to increase in the drag and generate a pitching down moment.

The previous separation wind tunnel tests were performed in scale 1:180 and the cases at 0 and 10° of angle of attack are comparable with the results of this paper.

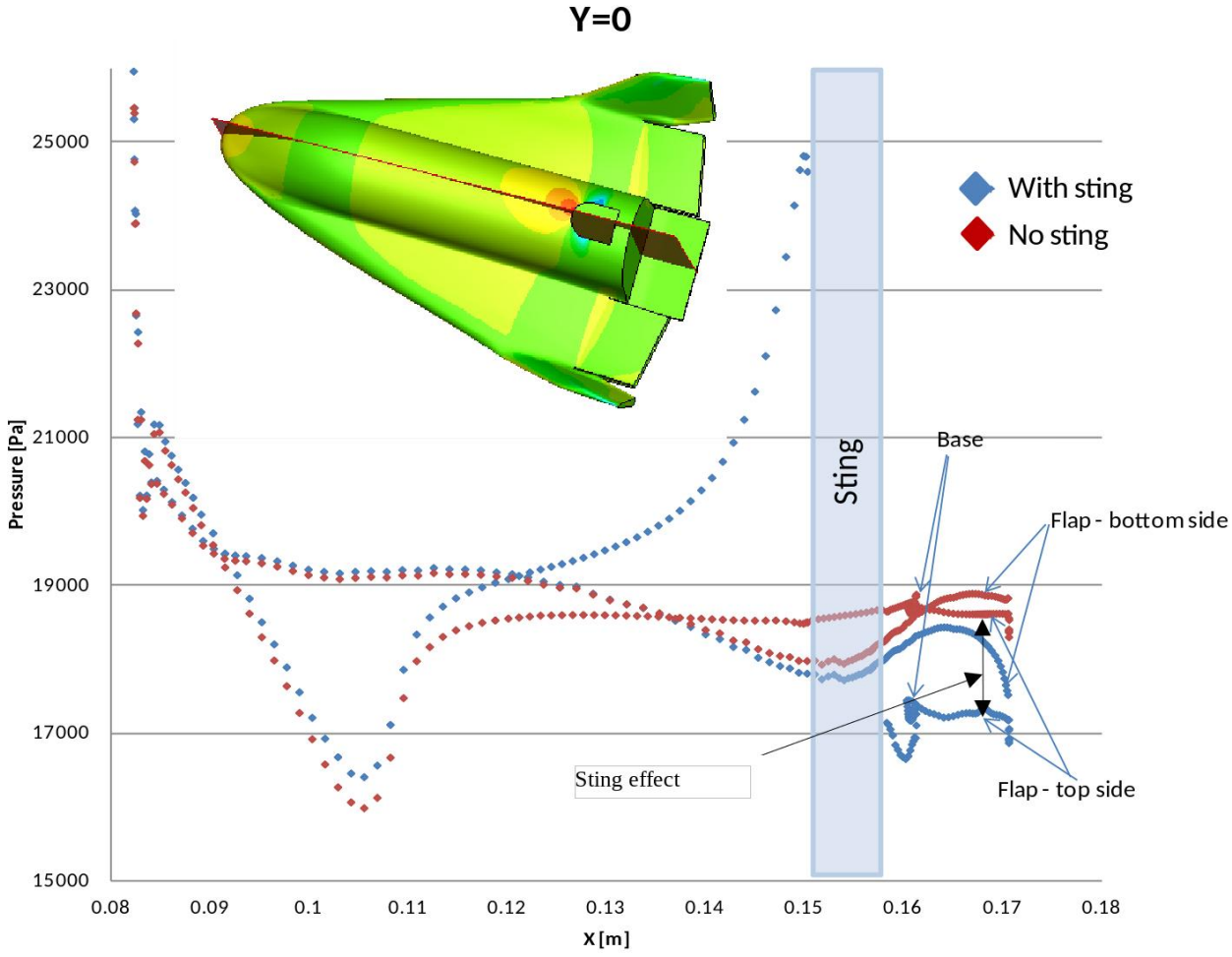

Figure 110. Pressure distribution on the middle Y plane of the SOAR with and without support; scale 1:180.

[35] It was the first approach to measure the behaviour of the SOAR atop of a carrier plane.

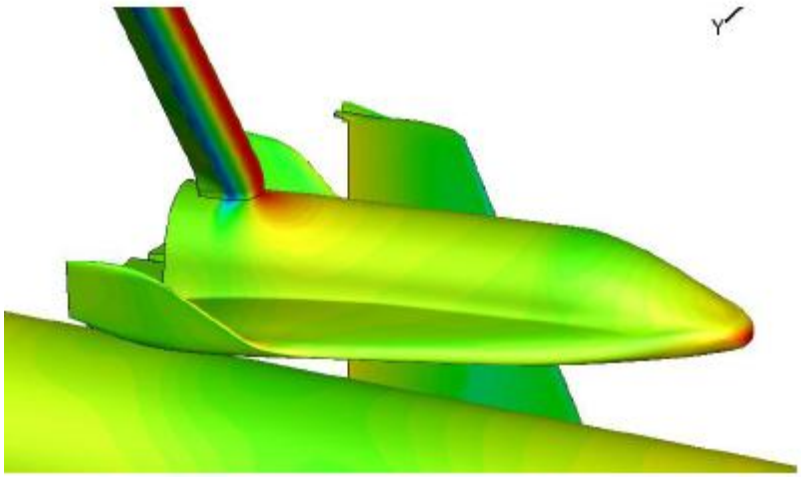

Figure 111. Sting effect. It is possible to see the red peak of pressure at the base of the sting; scale 1:180.

Table XXIX. Comparison of the support performance between the support with circular and elliptic sting and the old one. Scale 1:180, α=0°.

	Old support			New circular support			New elliptic support		
α	**ΔCD**	**ΔCL**	**ΔCM**	**ΔCD**	**ΔCL**	**ΔCM**	**ΔCD**	**ΔCL**	**ΔCM**
0	-0.0328	0.0662	0.0082	0.0045	0.0086	-0.0242	0.0039	0.0078	-0.0218
10	-0.0159	0.0891	0.0059	0.0058	0.0079	-0.0426	0.0046	0.0071	-0.0391

From the previous table it is possible to understand that with the use of the posterior supports dramatically the interferences reduce, in terms of drag and lift with respect to the dorsal strut. On the other hand the rear sting causes greater interferences about the pitching moment. It is also possible to see that the sting effect is opposite: while the drag was increased now it is decreased and the pitching moment now is higher while before it was smaller. Also the effect with the angle of attack is different: with the previous support the amount of the correction was reduced increasing α while the new models make the situation worse with high α. Only for the lift all choices cause decrease in the coefficient respect to the SOAR alone.

5.9 Local pressures and coefficients correction

In this paragraph the coefficient alterations are revised, but now looking at the pressure point by point. The following critical area of the vehicle are selected for this analysis:

- SOAR base surface;
- SOAR body;
- SOAR flap.

The following plots show the pressures gap in each zone. The analysis was performed for most of the cases but for reasons of brevity only few of them are presented. The main goal of the investigations is to find corrective coefficients to correct for the presence of the support with information coming from the pressure values. In fact during the wind tunnel test small transducer will be positioned to measure the pressure at smart location. With the coefficients found in this analysis it will be possible to have a value of the local pressure corrected and then close to what happen without the support. Afterwards it is desired to apply these coefficients also at corrective laws for the aerodynamics coefficients. The sense of the last point is to have a quick manner to obtain an indicative value of the coefficient correction for each case which can be tested in the wind tunnel. The study is done for the nominal dimension geometries function of the angle of attack.

First the local pressure values are presented, after the correction laws are explained.

5.9.1 SOAR base surface

The pressure is taken on the SOAR base surface on the line passing through the support midpoint in the y direction and in the z direction. Furthermore the pressures are evaluated on a base line below the sting junction.

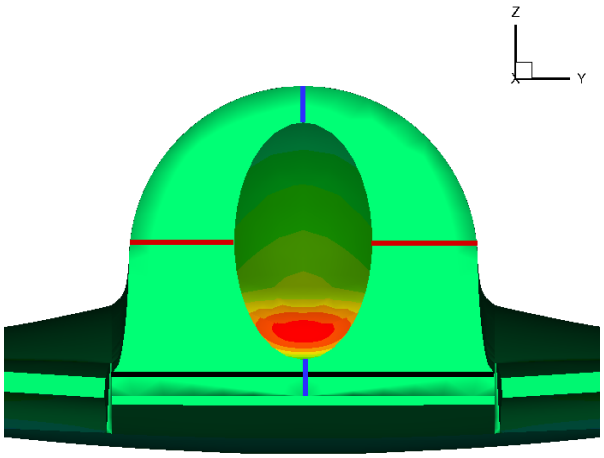

Figure 112. View of the base with the 3 lines (blue, black and red) where the pressure is evaluated.

It is possible to see that the circular sting induces higher pressure in the lower part of the base. Another remarkable difference is that with the circular, on the middle y line, closer to the sting, the pressure substantially decreases with respect to what happen for the elliptic sting. These results are present both in scale 1:180 both in scale 1:80 (see also Figure 85).

Increasing the sting length, as expected, the pressure is closer to the values of the SOAR alone. This is present with the same trend for both sting shapes in scale 1:180. In scale 1:80 the differences are small and not always this trend is clear (see Figure 113).

Investigating more deeply the pressure distribution below the sting it is possible to reveal that the main difference between the elliptic and the circular shape is here. In particular with the circular configuration there is a peak of pressure around the centre line. Increasing the angle of attack no important differences appear. The same tendency is also present in scale 1:80 (see Figure 115).

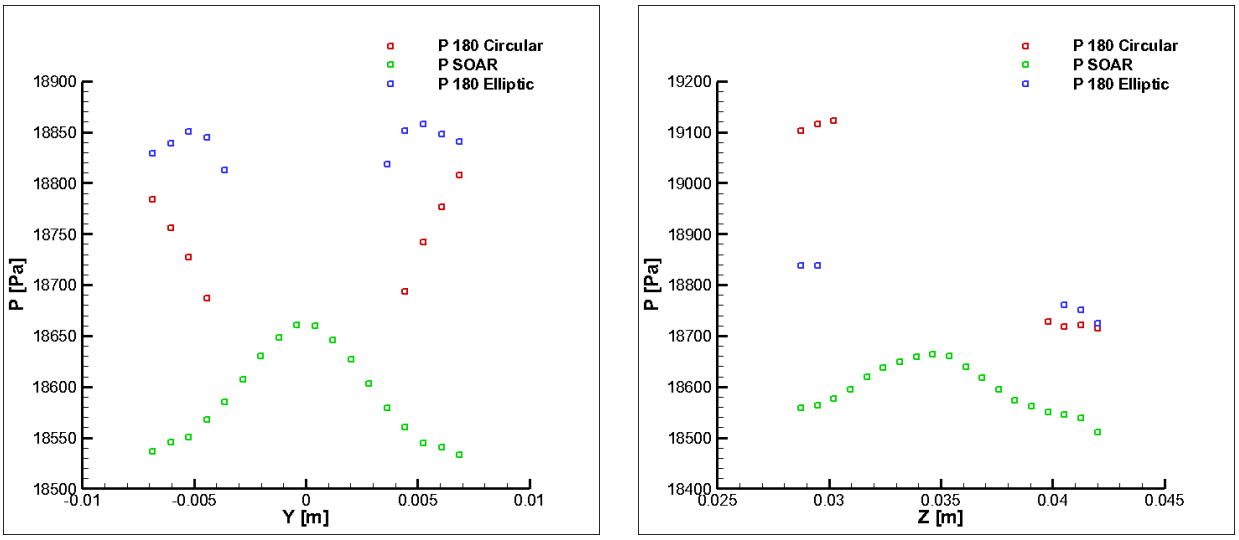

Figure 113. Pressure distribution plot on the middle y line on the left; on the middle z line on the right. SOAR alone and with different sting shape; scale 1:180, α=0°.

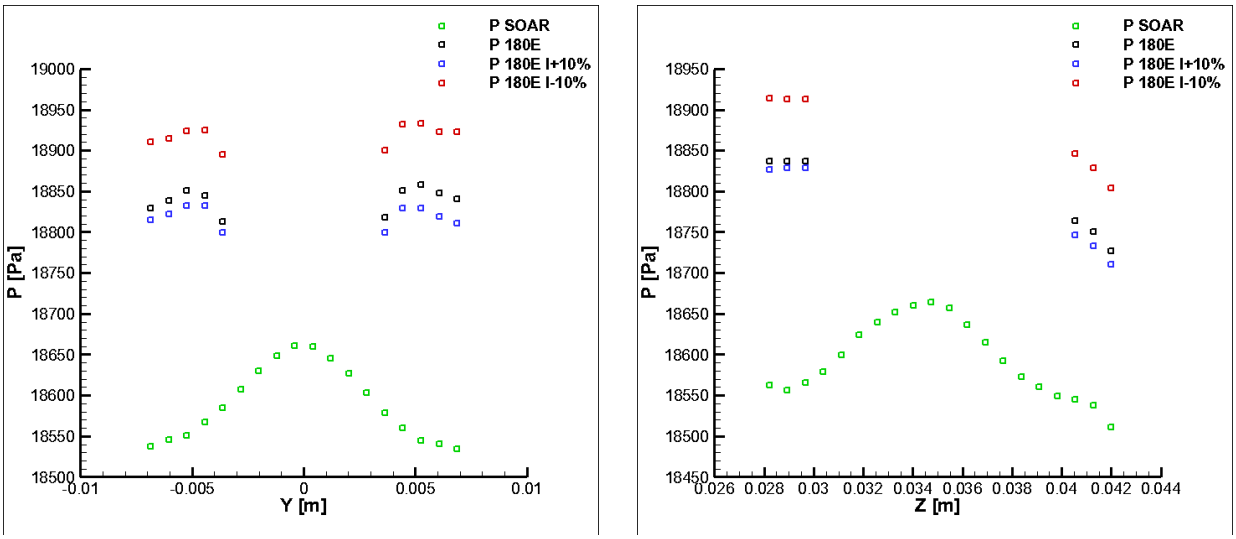

Figure 114. Pressure distribution plot on the middle y line on the left; on the middle z line on the right. SOAR alone and with different elliptic sting length; scale 1:180, α=0°.

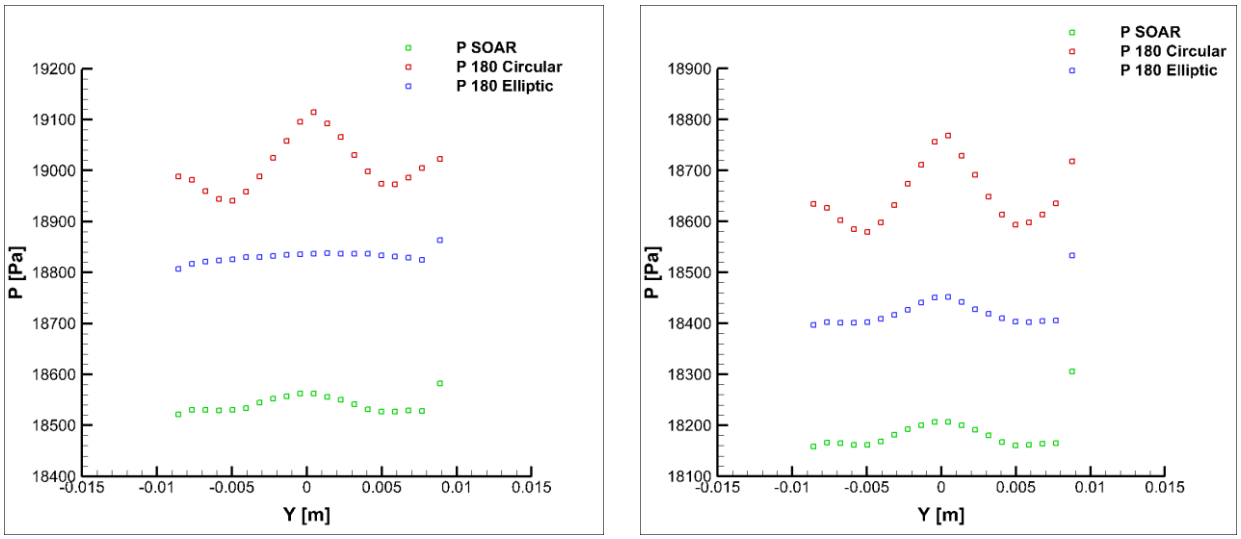

Figure 115. Pressure distribution plot on a line, in the y direction, under the sting junction. Scale 1:180, α=0° on the left, α=15° on the right.

5.9.2 SOAR body

The pressures on the top of the SOAR body, (in x direction), are evaluated from the end of the nose until the end of the body. It is the same plot of Figure 83 but now taken with a distribution of points and focused on body. The results presented are in scale 1:180. In scale 1:80 there is the same tendency but with minimal variations.

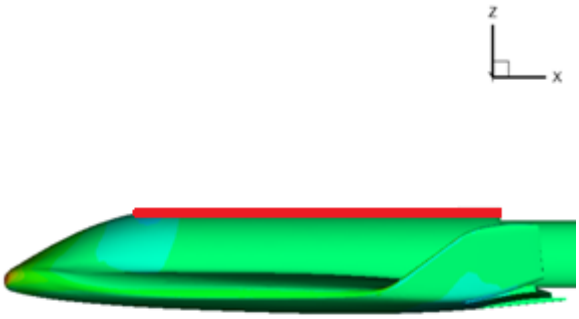

Figure 116. View of the SOAR with the red line that represent where the pressures are taken on the body.

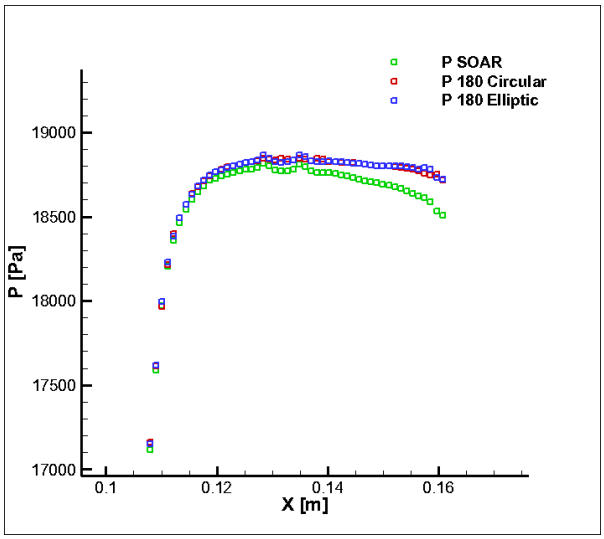

Figure 117. Pressure distribution plot on the centre line over the body; scale 1:180, α=0°.

5.9.3 SOAR flap

The pressure is taken on the right flap in the x direction following the line shown in Figure 119.

The first plot (top right) compares the values with the two different shapes and different lengths. As expected the longer sting always has a lower correction than the shorter and the elliptic shape is closer to the SOAR alone. The impact of higher pressure on the flap is always towards increasing the pitching up moment.

Interesting is to look at the plots of Figure 119 to understand how the pressure alterations are changing with the angle of attack. It is immediate to see that the flap is more affected by the sting for α = 0° than for α = 15° and that the circular sting produces less interferences on it increasing the angle of attack.

It is possible to find a similar trend also in scale 1:80 but the differences are minimal. Only plot in scale 1:180 are here reported.

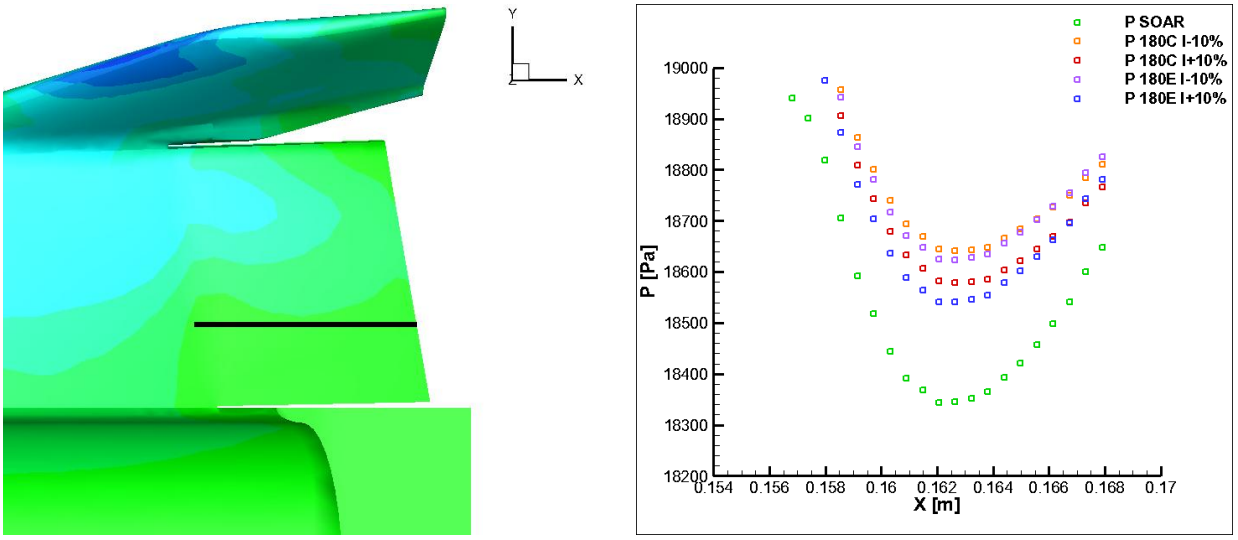

Figure 118. on the left view of the x line where the pressure is extracted. On the right pressure distribution on this line for different shape and geometry. Scale 1:180, α = 0°.

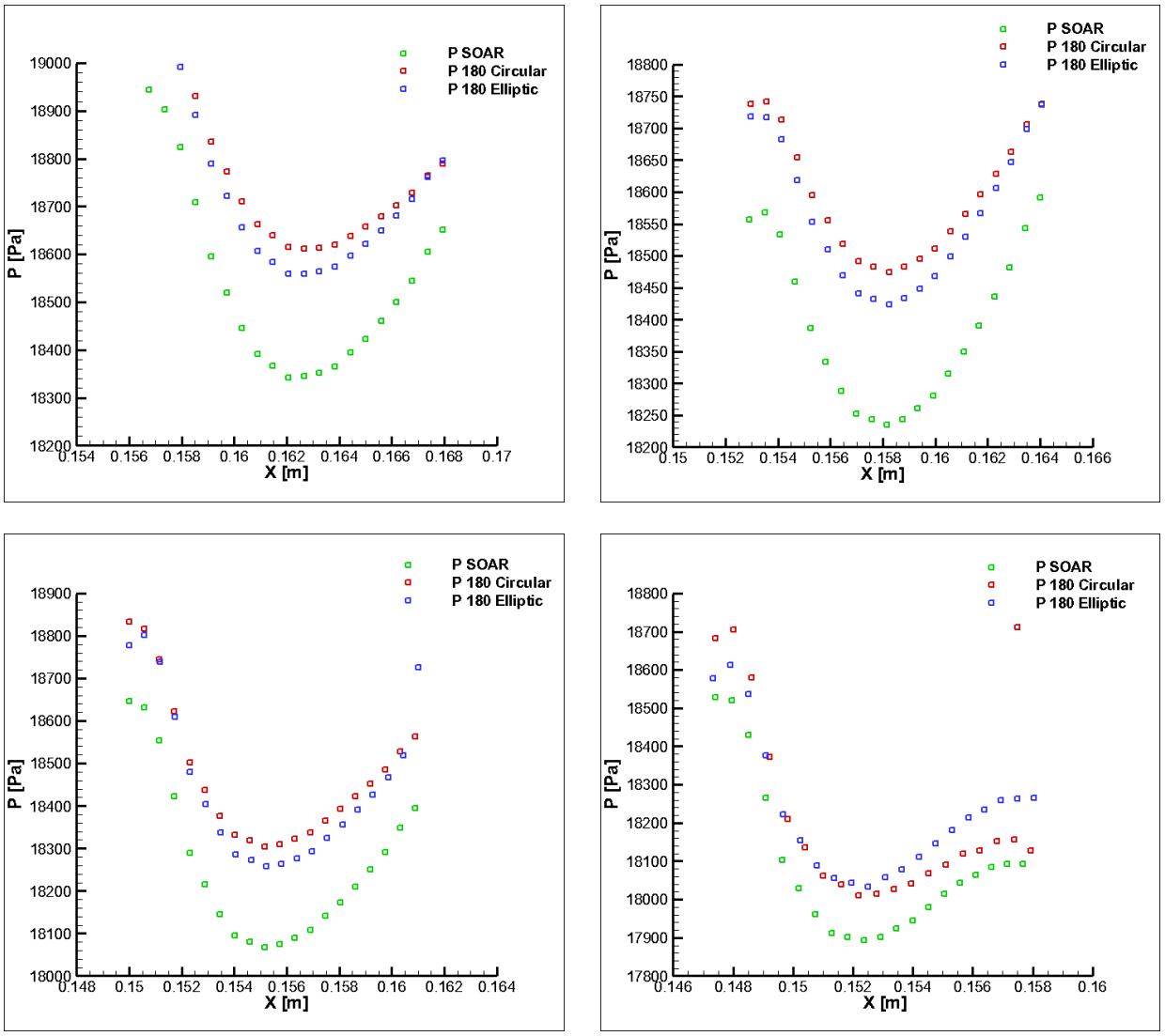

Figure 119. Pressure distribution with nominal dimensions, circular and elliptic sting. Scale 1:180, clockwise α = 0°, 5°,10°,15°.

5.9.4 Surface pressure ratio

The surface pressure ratios are reported in ANNEX D. For the scale 1:180 the results with the nominal sting dimensions and angle of attack of 0,5,10,15 degree are reported. For the case 1:80 only the results with 0 degree of angle of attack, again in nominal dimensions are reported.

5.9.5 Coefficients corrective laws

The coefficients coming from the simulations with support are corrected for the presence of the struts. The correction is performed at 0,5,10,15 degree of angle of attack and with the nominal dimensions for the supports.

The surface pressure alterations are considered responsible of the interferences on the coefficients. The differences on the base pressure are taken into account to correct the drag

while the values on the flap surfaces are supposed to be determinant for the pitching moment and the lift. Afterwards from these pressure ratios a first correction coefficient is applied and then other elements are added to try to have the best fit of the simulation results. The averaged surface pressure ratios, on the base and on the flap, used in the corrections are shown in the next table:

$$K_{i,j} = \frac{P_{SoarAlone\ i,j}}{P_{SoarWS\ i,j}}$$

(9)

Table XXX. Averaged local pressure ratio.

scale	1:180		1:80	
$K_{i,j}$	Circular	Elliptic	Circular	Elliptic
Flap	0.989	0.990	0.996	0.997
Base	0.975	0.986	0.989	0.994

The corrected results present always a residual averaged error from the SOAR alone lower than 10^{-4}, few cases have an error of 10^{-3}. The improvement from the results coming from the simulations is always at least one order of magnitude. It is useful to highlight that the nature of this correction is totally empiric. The pressure ratios are evaluated in Matlab with the data extrapolated from Tecplot. The correction laws are performed using Excel in the way explained in the previous lines.

5.9.5.1 Drag correction laws

The pressure corrective coefficient is in the denominator because the higher pressure induced by the sting on the SOAR base reduces the drag. This correction improves considerably the result and it was only necessary to add a constant term to had a better fitting of the values.

In scale 1:180 the following corrective laws, for the circular and the elliptic sting, are implemented:

$$C'_{D,C} = C_D \frac{1}{K_{b,C}} + 4{,}1174 \cdot 10^{-3}$$

(10) [36]

$$C'_{D,E} = C_D \frac{1}{K_{b,E}} + 3{,}498 \cdot 10^{-3}$$

(11)

Now in scale 1:80, again for the circular and elliptic sting:

[36] In this formula and in the followings the subscript "b" represent the base while "f" is for the flap. Obviously "C" means circular, while "E" is for elliptic.

$$C'_{D,C} = C_D \frac{1}{K_{b,C}} + 1{,}5146 \cdot 10^{-3}$$

(12)

$$C'_{D,E} = C_D \frac{1}{K_{b,E}} + 1{,}4388 \cdot 10^{-3}$$

(13)

It is possible to see that the correction is constant with respect to the angle of attack. The residual error with respect to the SOAR alone is almost always of 10^{-4}(see Table XXXI and Table XXXII).

5.9.5.2 Lift correction laws

To obtain a good fitting on the lift (in addition to the pressure depending and constant terms) also a coefficient function of the angle of attack was necessary[37]. This time the pressure coefficient multiplies the aerodynamics coefficient because the overpressure on the flap (and on the body) reduces the lift but making it less negative for α=0°.

In scale 1:180, for the circular and the elliptic sting:

$$C'_{L,C} = K_{f,C} C_L + 8.3573 \cdot 10^{-3} + 2.5311 \cdot 10^{-5} \alpha^{2,2}$$

(14)

$$C'_{L,E} = K_{f,E} C_L + 7.6171 \cdot 10^{-3} + 6.1430 \cdot 10^{-5} \alpha^{1,5}$$

(15)

In scale 1:80, for the circular and the elliptic sting:

$$C'_{L,E} = K_{f,C} C_L + 2.7075 \cdot 10^{-3} + 1.1164 \cdot 10^{-4} \alpha$$

(16)

$$C'_{L,E} = K_{f,E} C_L + 2.8858 \cdot 10^{-3}$$

(17)

5.9.5.3 Pitching moment correction laws

The pressure coefficient is divided by a factor 10 for the huge impact that the flap overpressure has on the coefficient due to the distance from the CoG and the large surface. Then everything is multiplied to the moment coefficient because the sting effect is to increase it. Always an angle of attack depending term is added and for the 1:80 elliptic sting also a constant term is presented.

[37] Except for the elliptic sting in scale 1:80.

In scale 1:180, for the circular and the elliptic sting:

$$C'_{M,C} = \frac{K_{f,C}}{10} C_M + 7.9296 \cdot 10^{-4}\alpha$$

(18)

$$C'_{M,E} = \frac{K_{f,E}}{10} C_M + 2.8187 \cdot 10^{-4}\ 8.511 \cdot 10^{-4}\alpha$$

(19)

In scale 1:80, for the circular and the elliptic sting:

$$C'_{M,C} = \frac{K_{f,C}}{10} C_M + 1.0313 \cdot 10^{-3}\alpha$$

(20)

$$C'_{M,E} = \frac{K_{f,E}}{10} C_M + \ 1.4618 \cdot 10^{-3} + \ 7.1719 \cdot 10^{-4}\alpha^{1.1}$$

(21)

In the following tables the differences between the coefficients for the SOAR alone and the SOAR with support (after this last correction) are reported. In the simulations column is indicated the scale, the sting shape and if an angle of attack different from zero is present. All cases are with the support nominal dimensions. The deviations are presented again as:

$$\Delta C = \ \Delta C_{Soar} - \Delta C_{SoarWS}$$

Table XXXI. Residual error after the correction; scale 1:180, α = 0°,5°,10°,15° and ΔC averaged.

Simulations	Δ_{CD}	Δ_{CL}	Δ_{CM}
1:180 C	-4.2614E-04	-1.7498E-08	4.9088E-05
1:180 C α=5	-1.6870E-05	3.4770E-09	-2.0839E-05
1:180 C α=10	-1.4023E-04	-1.0785E-03	2.7047E-04
1:180 C α=15	5.8333E-04	1.7296E-05	2.5804E-03
$\Delta_{C\ AV}$	**2.9164E-04**	**2.7396E-04**	**7.3019E-04**
1:180 E	-5.9492E-05	8.3185E-10	4.8438E-09
1:180 E α=5	1.1438E-04	-2.5930E-09	-9.0867E-10
1:180 E α=10	3.1247E-05	5.7212E-04	-2.5599E-04
1:180 E α=15	-8.6293E-05	-1.9474E-05	1.8503E-03
$\Delta_{C\ AV}$	**7.2854E-05**	**1.4790E-04**	**5.2658E-04**

Table XXXII. Residual error after the correction; scale 1:80.

Simulations	Δ_{CD}	Δ_{CL}	Δ_{CM}
1:80 C	1.7975E-04	-1.2763E-08	1.1230E-03
1:80 C α=5	2.9348E-04	-4.5311E-09	1.5592E-05
1:80 C α=10	-2.7368E-05	-3.0349E-04	-7.9467E-04
1:80 C α=15	-4.4580E-04	8.0450E-05	-2.0519E-06
$\Delta_{C\ AV}$	**2.3660E-04**	**9.5990E-05**	**4.8384E-04**
1:80 E	1.0903E-04	-4.5539E-04	-2.4395E-06
1:80 E α=5	2.2692E-04	-9.3800E-05	-4.4413E-06
1:80 E α=10	-1.4584E-05	-1.1545E-06	-2.7858E-04
1:80 E α=15	-3.2126E-04	5.5040E-04	6.6558E-04
$\Delta_{C\ AV}$	**1.6795E-04**	**2.7518E-04**	**2.3776E-04**

5.10 Conclusion of the CFD analysis

In this paragraph there are several considerations about the results. The conclusions on the two different scales are presented separately and each is analyzed alone.

5.10.1 Scale 1:180

First it is summarized the reflection about the sting shape, then about dimension, inclination and finally angle of attack variation. At the end there are the conclusive remarks about the comparison with the old support.

5.10.1.1 Considerations about the sting shape

The elliptic sting shape presents the best performance. Regarding the interferences, the advantage to use an elliptic shape as sting is evident for the pitching moment coefficient at all angle of attacks. For the lift and the drag this benefit is the most at α=15°.

5.10.1.2 Considerations about the dimensional variations

Any variations of 10% dimensions does not produce relevant differences on the coefficients. However the trend is what was expected: the interferences go down increasing the length and decreasing the diameter. The order of magnitude of the variations is always 10^{-3}.

If the project constraints will change an increase of the length and a decrease of the diameter should be considered.

5.10.1.3 Considerations about the inclination variation

Increasing the vertical parts inclination the interferences increase. If the variation is of 5° or maximum 10° the effect is minimal, at 55.8° the interferences rise more but it always stay small.

It is not clear the origin of the countertrend for the circular stings drag at 45.8° and 50.8° of inclination even if we speak of a reduction of about $4 \cdot 10^{-4}$.

5.10.1.4 Considerations about the angle of attack effect

Until 10° of angle of attack the effect of the shape is minimal and it does not justify a choice or another. For α=15° the elliptic sting should definitely be used. At 15° angle of attack having a sting 10% longer reduces the interferences. It is not yet clear why this does not happen with the circular sting for the pitching moment.

If possible, the sting should be at least 8-10% longer for test at α=15°.

5.10.1.5 Comparison with the old support

The first consideration is that the SOAR rear part, including their flaps, is a critical zone for the interferences. In fact for their large flat surface only small deviance on the pressure contour causes great alteration on the coefficients. This in particular affects the pitching moment for the distance from the CoG. Every kind of support, more or less, will produce alterations on the flow in this part and then a certain amount of interferences are inevitable. On the other hand to have a support that does not interfere with the rear part is not possible. The dramatic reduction of drag and lift interferences, with a posterior sting, seems to be interesting even if it is necessary to take into account a worsening on the pitching moment. With a little optimization on the design, the usage of an elliptic shape[38] and the research of some expedient to reduce the moment interferences may be the best solution.

5.10.2 Scale 1:80

This paragraph is structured the same way as the previous one with the only difference that there are not remarks about different inclinations and comparison with any old support. It is useful to remind that for the SOAR in scale 1:80 a sting has not yet been designed.

[38] The elliptic sting is suggested in particular to improve the behaviour with a not small angle of attack (more than 10°).

5.10.2.1 Considerations about the sting shape

For all the coefficients the interferences, in spite of the greater scale, are at least half of what happens with the 1:180 supports. For the lift and the drag the differences between the two shapes are halved, with the same trend. The pitching moment worsening with α is reduced, especially for the elliptic sting. It has already been cleared that this kind of support design is less problematic and in particular for small angle of attack the sting shape, circular or elliptic, is irrelevant.

5.10.2.2 Considerations about the dimensional variations

Variation of the 10% in the length are definitely not significant.

5.10.2.3 Considerations about the angle of attack effect

At 15° of angle of attack the usage of an elliptic sting should be considered.

The dimensional variations, similarly at what happens in scale 1:180 have a bigger impact with increasing angle of attack. Now longer sting is more advantageous for pitching moment measurement. It is recommended to take this into account.

5.11 Recommendations for the future CFD activities

The following critical points are suggested as future activities:

- have a better mesh refinement on the SOAR rear surface to better understand the pressure variation on that zone;
- give more attention to the CFD geometry simplification in order to ensure the same shape in every case;
- apply greater length variation in the scale 1:80 sting where these constraints are less severe;
- to perform simulations at more angle of attacks to understand better the impact of the shape and dimensional variations.

6 Overall conclusions

6.1 Concluding remarks

After having performed all the designing process not so critical situations to require a new iteration in the designing appear. All supports are structurally valid and induce an amount of interferences manageable with the suitable corrections.

Considering also the experience with the previous support it seems that, for the wind tunnel test with the composite configuration (SOAR and Airbus, scale 1:180), the utilization of a posterior sting with an inclined bar should be the best solution. Furthermore with respect to the old support with this project it has been possible to reach:

- the design of supports that allow an overall decrease of interferences;
- the awareness that a sting passing over the SOAR flap dramatically increase the interferences on the pitching moment. More generally the usage of posterior supports for the SOAR is always critic;
- a better knowledge in how supports can interfere with the SOAR;
- a better knowledge in how the variation of shape and dimensions modifies the level of interferences.

About the design of straight stings for the SOAR alone (scale 1:80) the problem is less critic and the interferences are smaller. However also in this case the utilization of stings passing over the flaps (to sustain the vehicle from the base) produces important interferences on the pitching moment.

Furthermore no substantial differences were detected varying 10% the length. The results achieved, even if incomplete, are not in disagreement with the theory about the usage of "short sting" with turbulent flow (scale 1:80).

The usage of elliptic stings is something that should be considered for test in both scales when the angle of attack is higher or equal to 15 degree.

6.2 Recommendations for the future activities

Partial recommendations after the structural analysis and the CFD study have already been written in paragraph 4.6 and 5.11. Here only overall suggestion are reported that is that the points specifically regarding only the performing of one part and not the whole project are not repeated again.

Small geometrical variations of the supports drawing, that does not compromise the general results of the structural and aerodynamics analysis, are recommended:

- a small lengthen (about 0.2 mm) of the slot for the cables in the inclined bar of the supports (scale 1:180). This for have a margin and a better sliding for the cables. Not to reduce the wall thickness, the same lengthen has to be performed also on the external shape;
- a small lengthen (about 0.2 mm) also for the elliptic sting for the 1:180 support. Also in this case the same amount for the hole diameter and for the sting diameter is suggested not to reduce the wall thickness.
- a small lengthen (0.2 mm) of the wall thickness for the elliptic straight sting in scale 1:80.
- make smaller the diameter for the circular sting in scale 1:80:
    - to bring the ratio $\frac{ds}{D}$ at about 0.28 for the external diameter;
    - to reduce at about 6.5 mm the internal hole.

When the new versions of the SOAR and of the Airbus will be transmitted it is suggested to revise all support dimensions (especially the length for the stings in the scale 1:180 supports).

Furthermore it is suggested to:

- to research a solution to decrease the interferences on the pitching moment. To permit this in scale 1:80 there is the possibility to position the sting higher on the SOAR base. This should reduce the flow blockage over the flaps. It is more difficult to realize the same in scale 1:180 (especially for the elliptic sting) for the higher ratio $\frac{ds}{D}$ already existent;
- to estimate the accuracy and the usefulness of the new correction methods purpose in paragraph 5.9;
- to extend the investigation on the usage of elliptic stings, especially performing more CFD test at angle of attack higher than 10 degree;
- to perform CFD test of supports with the completed sustaining mechanism. This is useful especially for the straight sting (scale 1:180) where testing only the last part of the support it is not possible to clarify the interferences variations with the length. Therefore it will be possible also to understand better the influence of the Reynolds number on the length to have an additional confirmation of the necessity of short sting with turbulent flow. To do this it is also necessary to apply larger variation of the 10%, as already said in 5.11.

ANNEX A: plotted aerodynamic coefficients

The aerodynamic coefficients of the SOAR with the support and alone are here reported:

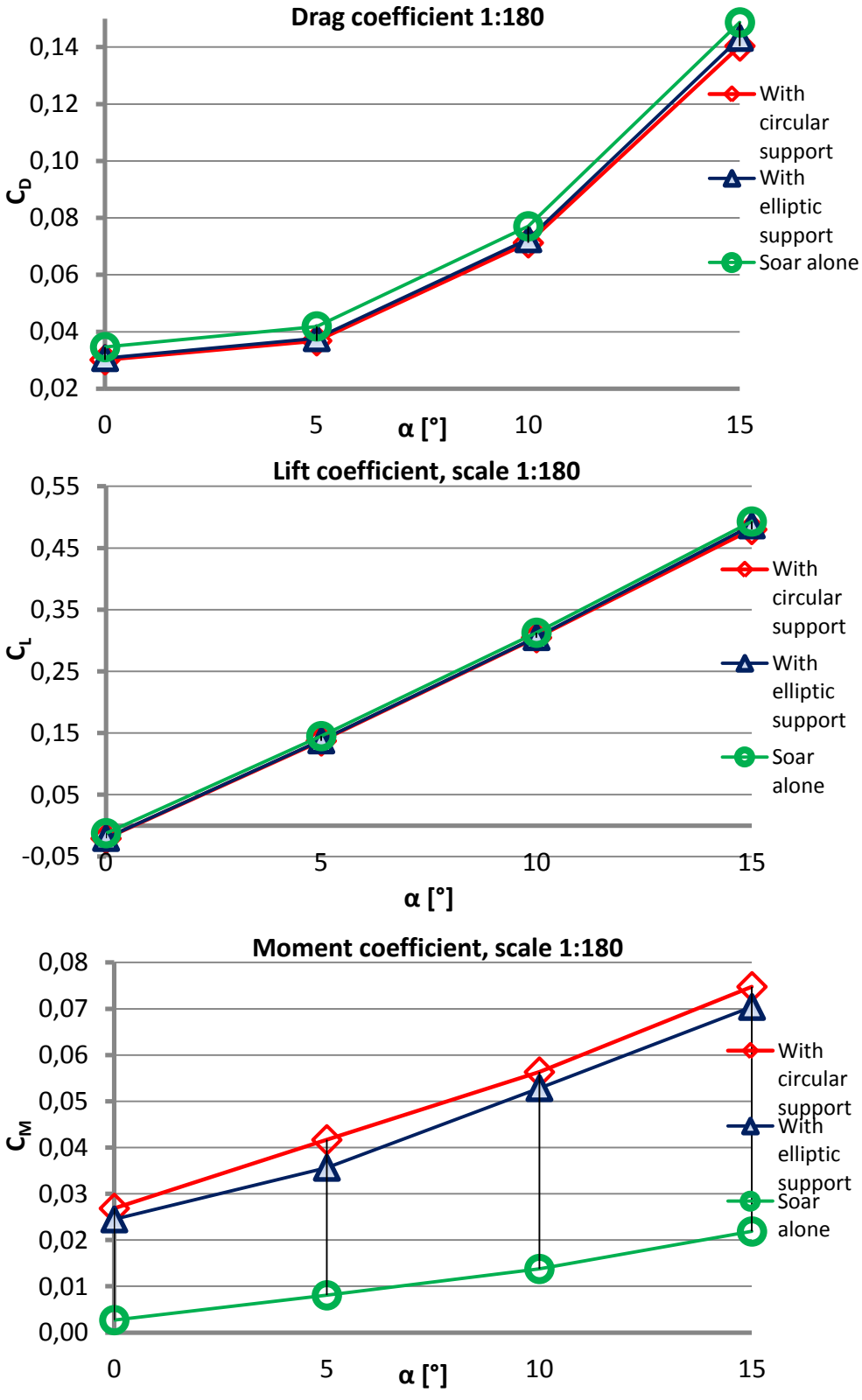

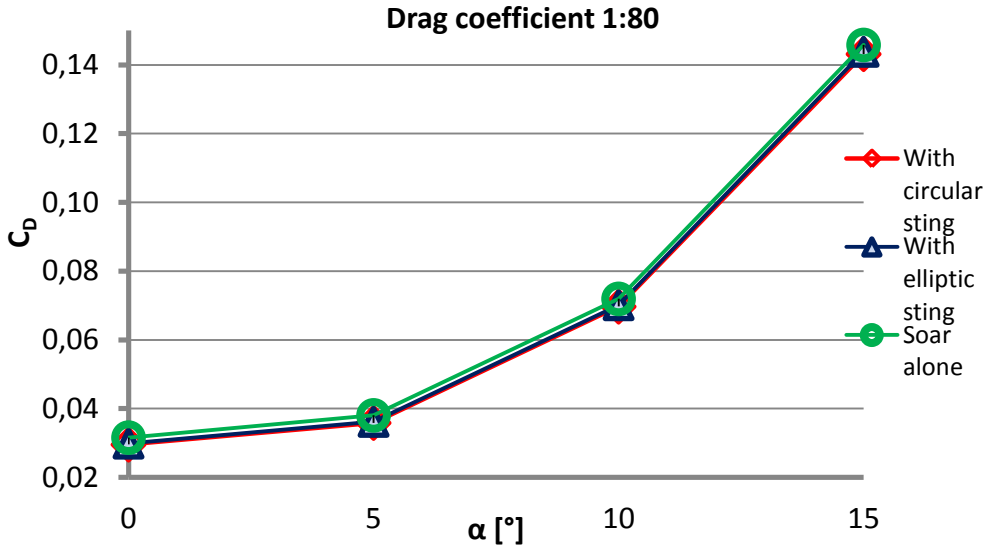
Drag coefficient 1:80
0,14
0,12
0,10
0,08
0,06
0,04
0,02
C_D
0
5
10
15
α [°]
With circular sting
With elliptic sting
Soar alone

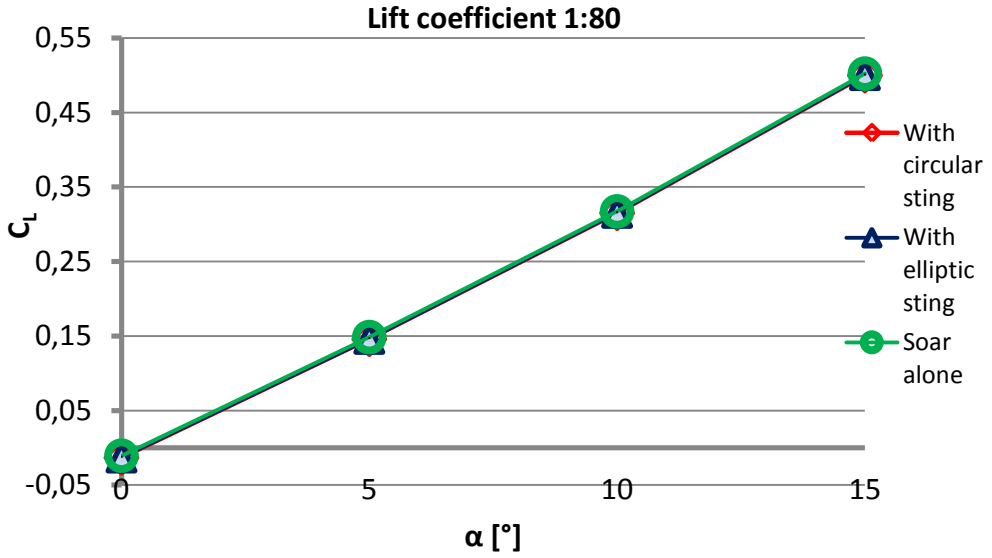
Lift coefficient 1:80
0,55
0,45
0,35
0,25
0,15
0,05
-0,05
C_L
0
5
10
15
α [°]
With circular sting
With elliptic sting
Soar alone

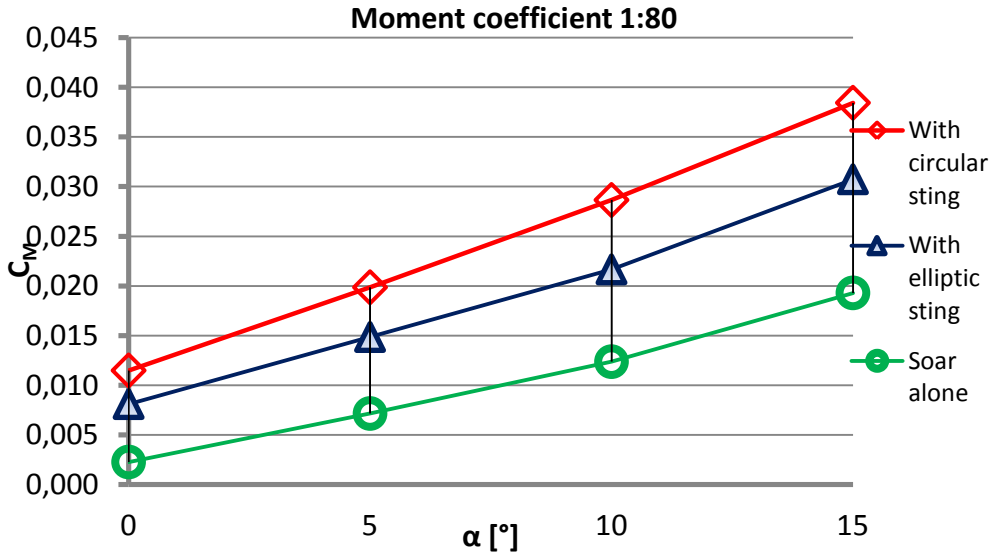
Moment coefficient 1:80
0,045
0,040
0,035
0,030
0,025
0,020
0,015
0,010
0,005
0,000
C_M
0
5
10
15
α [°]
With circular sting
With elliptic sting
Soar alone

ANNEX B: tabulated experimental results

Scale 1:80

Here the tabulated experimental results are reported. When is not written "SOAR alone" it means that it is a simulations with the presence of the support. First it is indicates the scale, then the sting shape (C-circular, E-elliptic) after if a dimensional variation is applied (l-length, d-diameter and B-inclination of the vertical bar).

Simulations	α [°]	C_D	C_L	C_M
SOAR alone	0	0.03159	-0.01062	0.00227
SOAR alone	5	0.03808	0.14857	0.00715
SOAR alone	10	0.07196	0.31735	0.01237
SOAR alone	15	0.14582	0.50232	0.01930
1:80 C	0	0.02957	-0.01338	0.01148
1:80 C	5	0.03587	0.14588	0.01986
1:80 C	10	0.06970	0.31509	0.02865
1:80 C	15	0.14316	0.49986	0.03844
1:80 C l+10%	0	0.02941	-0.01384	0.01161
1:80 C l+10%	15	0.14342	0.49979	0.02719
1:80 C l-10%	0	0.02954	-0.01365	0.01156
1:80 C d+10%	0	0.02961	-0.01386	0.01328
1:80 C d+10%	15	0.14344	0.50008	0.04230

Simulations	α [°]	C_D	C_L	C_M
SOAR alone	0	0.03159	-0.01062	0.00227
SOAR alone	5	0.03808	0.14857	0.00715
SOAR alone	10	0.07196	0.31735	0.01237
SOAR alone	15	0.14582	0.50232	0.01930
1:80 E	0	0.02987	-0.01309	0.00810
1:80 E	5	0.03619	0.14621	0.01485
1:80 E	10	0.07012	0.31541	0.02166
1:80 E	15	0.14383	0.50039	0.03074
1:80 E l+10%	0	0.02980	-0.01236	0.00938
1:80 E l+10%	15	0.14376	0.50033	0.02241
1:80 E l-10%	0	0.02986	-0.01312	0.00812
1:80 E d+10%	0	0.02953	-0.01311	0.00916
1:80 E d+10%	15	0.14375	0.50034	0.03331

Scale 1:180

Simulations	α [°]	C_D	C_L	C_M
SOAR alone	0	0.03462	-0.01226	0.00271
SOAR alone	5	0.04189	0.14504	0.00807
SOAR alone	10	0.07706	0.31265	0.01377
SOAR alone	15	0.14868	0.49295	0.02187
1:180 C	0	0.03015	-0.02084	0.02686
1:180 C	5	0.03685	0.13732	0.04168
1:180 C	10	0.07126	0.30471	0.05632
1:180 C	15	0.14037	0.48007	0.07477
1:180 C l+10%	0	0.03137	-0.02050	0.02674
1:180 C l+10%	15	0.14327	0.48548	0.07331
1:180 C l-10%	0	0.03018	-0.02352	0.02745
1:180 C d+10%	0	0.03025	-0.02196	0.03198
1:180 C d+10%	15	0.14152	0.48397	0.08599
1:180 C B+5°	0	0.03054	-0.02282	0.02725
1:180 C B+10°	0	0.03045	-0.02390	0.02742
1:180 C B+15°	0	0.03012	-0.02471	0.02754

Simulations	α [°]	C_D	C_L	C_M
SOAR alone	0	0.03462	-0.01226	0.00271
SOAR alone	5	0.04189	0.14504	0.00807
SOAR alone	10	0.07706	0.31265	0.01377
SOAR alone	15	0.14868	0.49295	0.02187
1:180 E	0	0.03074	-0.02007	0.02449
1:180 E	5	0.03774	0.13812	0.03564
1:180 E	10	0.07250	0.30557	0.05287
1:180 E	15	0.14323	0.48665	0.07041
1:180 E l+10%	0	0.03098	-0.01929	0.02433
1:180 E l+10%	15	0.14397	0.48803	0.04178
1:180 E l-10%	0	0.02923	-0.02326	0.02509
1:180 E d+10%	0	0.03050	-0.02046	0.02881
1:180 E d+10%	15	0.14312	0.48656	0.07861
1:180 E B+5°	0	0.03048	-0.02079	0.02463
1:180 E B+10°	0	0.03028	-0.02211	0.02489
1:180 E B+15°	0	0.03014	-0.02299	0.02500

ANNEX C: aerodynamic coefficients of the SOAR and the Airbus in the composite configuration

The tabulated results reported here come from the previous wind tunnel test campaign [1].

Composite Mach=0.70			AoA_Airbus=1.5				
AoA_Soar	AoA_ Airbus	CD_soar	CL_soar	Cm_soar	CD_Airbus	CL_Airbus	Cm_Airbus
5.507548	1.499815	0.037415	-0.031995	0.030256	0.046074	0.273427	-0.078899
6.004093	1.499815	0.03809	-0.01503	0.031129	0.045845	0.269925	-0.075156
6.506391	1.499815	0.039281	0.004278	0.03169	0.045622	0.266873	-0.069521
7.008612	1.499815	0.040442	0.022187	0.032465	0.045181	0.261391	-0.06471
7.504533	1.499815	0.041945	0.039905	0.033259	0.044941	0.256586	-0.060637
8.004474	1.499815	0.043817	0.057885	0.034182	0.044787	0.252518	-0.056519
5.495892	1.499815	0.036007	-0.038439	0.031847	0.046011	0.272666	-0.083456
5.022139	1.499815	0.035251	-0.054021	0.030362	0.046195	0.277785	-0.08656
4.52678	1.499815	0.034709	-0.070619	0.028931	0.046309	0.281697	-0.089908
3.989086	1.499815	0.034637	-0.091699	0.028868	0.046656	0.28609	-0.09659
3.491635	1.499815	0.034604	-0.10892	0.027775	0.046807	0.289384	-0.100444
2.99151	1.499815	0.034683	-0.12576	0.026609	0.047055	0.29278	-0.104092
2.491869	1.499815	0.035065	-0.143594	0.025822	0.047215	0.29642	-0.108212
2.015869	1.499815	0.035589	-0.160017	0.025131	0.047399	0.299172	-0.110476
1.492747	1.499815	0.03648	-0.179362	0.024413	0.047577	0.302002	-0.115393
0.988819	1.499815	0.037608	-0.196841	0.023168	0.047706	0.304391	-0.11934
0.487779	1.499815	0.039547	-0.214572	0.022265	0.047934	0.306744	-0.122543
-0.012382	1.499815	0.041638	-0.23235	0.021265	0.048059	0.308473	-0.126048
5.508657	1.499815	0.033501	-0.030095	0.029603	0.045795	0.275144	-0.078376

ANNEX D: surface pressure ratio

The following ratio is here reported:

$$K = \frac{P_{SoarAlone}}{P_{SoarWS}}$$

It is pointed out that occasionally the first and last points are out of range. This can be due to transient phenomena at the extremity or a small difference in the position of the last points that arranges them out of the contour. In the different columns there is the variation of the angle of attack.

Flap surface pressure ratios; scale 1:180							
Circular sting				Elliptic sting			
0 [°]	5 [°]	10 [°]	15 [°]	0 [°]	5 [°]	10 [°]	15 [°]
0.9907	0.9904	0.9901	0.9917	0.9921	0.9914	0.9930	0.9973
0.9901	0.9907	0.9902	0.9901	0.9917	0.9920	0.9910	0.9951
0.9893	0.9904	0.9899	0.9919	0.9911	0.9920	0.9901	0.9943
0.9883	0.9896	0.9892	0.9942	0.9904	0.9915	0.9899	0.9940
0.9873	0.9888	0.9885	0.9941	0.9897	0.9910	0.9896	0.9934
0.9866	0.9881	0.9879	0.9942	0.9892	0.9905	0.9897	0.9931
0.9859	0.9876	0.9875	0.9945	0.9887	0.9902	0.9895	0.9930
0.9854	0.9870	0.9871	0.9930	0.9884	0.9898	0.9895	0.9921
0.9854	0.9870	0.9871	0.9940	0.9884	0.9897	0.9896	0.9921
0.9854	0.9870	0.9871	0.9933	0.9883	0.9897	0.9896	0.9922
0.9856	0.9871	0.9871	0.9931	0.9884	0.9897	0.9897	0.9914
0.9859	0.9874	0.9873	0.9934	0.9886	0.9898	0.9898	0.9914
0.9863	0.9876	0.9875	0.9931	0.9888	0.9899	0.9899	0.9908
0.9869	0.9880	0.9878	0.9938	0.9891	0.9901	0.9900	0.9908
0.9874	0.9884	0.9881	0.9942	0.9894	0.9903	0.9901	0.9909
0.9883	0.9890	0.9885	0.9953	0.9898	0.9905	0.9902	0.9907
0.9892	0.9896	0.9890	0.9951	0.9903	0.9909	0.9904	0.9906
0.9902	0.9903	0.9895	0.9961	0.9909	0.9911	0.9905	0.9905
0.9915	0.9913	0.9903	0.9981	0.9917	0.9917	0.9908	0.9907
0.9926	0.9922	0.9909	0.9670	0.9923	0.9922	0.9823	0.9906

Base surface pressure ratios; scale 1:180							
Circular sting				Elliptic sting			
0 [°]	5 [°]	10 [°]	15 [°]	0 [°]	5 [°]	10 [°]	15 [°]
0.9754	0.9773	0.9745	0.9745	0.9848	0.9869	0.9871	0.9871
0.9762	0.9780	0.9752	0.9752	0.9848	0.9866	0.9872	0.9872
0.9774	0.9790	0.9765	0.9765	0.9846	0.9863	0.9871	0.9871
0.9781	0.9797	0.9772	0.9772	0.9844	0.9860	0.9870	0.9870
0.9783	0.9801	0.9776	0.9776	0.9843	0.9861	0.9869	0.9869
0.9776	0.9796	0.9769	0.9769	0.9843	0.9865	0.9869	0.9869

0.9766	0.9790	0.9758	0.9758	0.9848	0.9875	0.9872	0.9872
0.9752	0.9778	0.9742	0.9742	0.9852	0.9882	0.9873	0.9873
0.9737	0.9765	0.9726	0.9726	0.9853	0.9887	0.9869	0.9869
0.9721	0.9749	0.9706	0.9706	0.9855	0.9891	0.9867	0.9867
0.9711	0.9739	0.9701	0.9701	0.9854	0.9891	0.9867	0.9867
0.9719	0.9745	0.9717	0.9717	0.9850	0.9885	0.9868	0.9868
0.9729	0.9753	0.9733	0.9733	0.9847	0.9879	0.9872	0.9872
0.9743	0.9764	0.9749	0.9749	0.9843	0.9871	0.9871	0.9871
0.9754	0.9772	0.9760	0.9760	0.9838	0.9860	0.9868	0.9868
0.9764	0.9780	0.9767	0.9767	0.9837	0.9855	0.9868	0.9868
0.9765	0.9780	0.9765	0.9765	0.9838	0.9855	0.9869	0.9869
0.9759	0.9775	0.9758	0.9758	0.9840	0.9858	0.9870	0.9870
0.9749	0.9766	0.9747	0.9747	0.9843	0.9862	0.9870	0.9870
0.9768	0.9807	0.9779	0.9779	0.9851	0.9873	0.9877	0.9877

Flap surface pressure ratios; scale 1:80							
Circular sting				**Elliptic sting**			
0 [°]	**5 [°]**	**10 [°]**	**15 [°]**	**0 [°]**	**5 [°]**	**10 [°]**	**15 [°]**
0.9972				0.9980			
0.9970				0.9978			
0.9967				0.9976			
0.9962				0.9973			
0.9957				0.9969			
0.9954				0.9967			
0.9951				0.9965			
0.9949				0.9964			
0.9949				0.9964			
0.9949				0.9964			
0.9950				0.9965			
0.9952				0.9966			
0.9954				0.9967			
0.9957				0.9968			
0.9960				0.9969			
0.9964				0.9971			
0.9969				0.9973			
0.9974				0.9975			
0.9983				0.9979			
0.9990				0.9981			

Base surface pressure ratios; scale 1:80							
Circular sting				Elliptic sting			
0 [°]	5 [°]	10 [°]	15 [°]	0 [°]	5 [°]	10 [°]	15 [°]
0.9889				0.9938			
0.9892				0.9938			
0.9898				0.9938			
0.9903				0.9939			
0.9906				0.9941			
0.9904				0.9942			
0.9897				0.9944			
0.9889				0.9944			
0.9883				0.9944			
0.9877				0.9945			
0.9878				0.9944			
0.9883				0.9942			
0.9890				0.9942			
0.9898				0.9943			
0.9905				0.9942			
0.9907				0.9940			
0.9904				0.9939			
0.9899				0.9938			
0.9893				0.9937			
0.9889				0.9937			

References

[1] S. Paris and T. Bànyai, Contribution to the aerodynamic database of the SOAR and the A300 during the separation - Wind tunnel tests and CFD, Rhode Saint Genèse: Von Karman institute for fluid dynamics, 2014.

[2] H. M. Schurmeier, An investigation of the interference effect of a sting support system on the pressure distribution over a body of revolution, Pasadena, California: Pasadena institute of technology, 1949.

[3] A. Pope, Wind tunnel calibration techniques, AGARDograph, 1961.

[4] F. B. Cyran, Sting interference effects on the static, Dynamic, and base pressure measurements of the standard dynamics medel aircraft at Mach numbers 0.3 through 1.3, Arnold air force station, Tennessee USA: Arnold engineering development center, August 1981.

[5] S. Hoerner, Fluid Dynamic Drag, USA: Hoerner, 1965.

[6] D. L. Loving and A. A. Luoma, Sting support interference on longitudinal aerodynamic Characteristics of cargo-type airplane models at Mach 0.70 to 0.84, Langley Station, Hampton, Va: Langley research center, July 1967.

[7] J. D. Anderson Jr., Fundamentals of aerodynamics fifth edition, New york: Mcgraw-Hill, 2011.

[8] Swiss Space System internal document, Soar design definition file design justification file, 2013.

[9] Ansys, Inc., Help manual, documentation for Ansys 15.0, Cannosburg, USA, 2014.

[10] J. Vierendeels e J. Degroote, «Aspects of CFD computations with commercial packages,» in *Introduction to computational fluid dynamics*, Von Karman Institute For Fluid Dynamics, 2015.

[11] F. Menter, «Turbulence modelling for engineering flows,» in *Introduction to computational fluid dynamics*, Von Karman Institute For Fluid Dynamics, 2015.

[12] S. Paris, Investigation of dynamic stability in transonic and supersonic regime, Rhode Saint Genèse: Von karman institute for fluid dynamic, 2009.